GAP PLASMON RESONANCES IN METAL FILM-COUPLED NANOPARTICLES FOR ENHANCED PHOTOLUMINESCENCE AND NONLINEAR OPTICAL EMISSION

LI GUANGCAN

Ph.D

The Hong Kong Polytechnic University

2017

The Hong Kong Polytechnic University

Department of Applied Physics

Gap Plasmon Resonances in Metal Film-coupled Nanoparticles for Enhanced Photoluminescence and Nonlinear Optical Emission

LI Guangcan

A thesis submitted in partial fulfilment

of the requirements for the degree of

Doctor of Philosophy

January 2017

CERTIFICATE OF ORIGINALITY

I hereby declare that this thesis is my own work and that, to the best of my knowledge and belief, it reproduces no material previously published or written, nor material that has been accepted for the award of any other degree or diploma, except where due acknowledgement has been made in the text.

_____(Signed)

LI Guangcan (Name of student)

Abstract

Placing a noble metal nanoparticle near a metallic substrate can significantly modify its optical properties, for which the metal film-coupled nanoparticle system has received extensive research interests in the past decade. In this structure configuration, the capacitive electromagnetic coupling between the particle plasmon resonance and its induced charges distributed in the metal film results in a gap plasmon mode featured by substantially enhanced electromagnetic field intensity at the gap junction, which offers a promising platform for various plasmon-enhanced optical phenomena. Particularly, the ease in fabrication and readily control over the particle-film gap distance down to sub-nanometer scale enable the realization of an ultrasmall plasmonic nanocavity, which has triggered a host of recent breakthroughs in fundamental nanophotonic research and energy harvesting applications such as photocatalysis.

This thesis reports our studies on the linear and nonlinear plasmonic properties of the metal film-coupled nanoparticle system. Firstly, our studies focus on experimental characterization and theoretical understanding on the fundamental properties of the gap plasmon modes in gold film-coupled nanoparticle monomers and dimers, with particular attention on the plasmon hybridization upon coupling the nanoparticles to the metal film. Secondly, our studies explore several fascinating gap plasmon resonance-enhanced linear and nonlinear optical phenomena, including photoluminescence (PL) and nonlinear optical emission such as second-harmonic generation (SHG) and two-photo absorption induced luminescence (TPL).

In the first part of this thesis, the plasmonic scattering properties of the gap plasmon modes of the gold film-coupled nanoparticle monomers and dimers are revealed experimentally. By using an improved dark-field spectroscopy and imaging methodology – polarization resolved spectral decomposition and color decoding, one can “visualize” and distinguish unambiguously the spectral and far-field radiation properties of the complex gap plasmon modes in the two systems. Together with the full-wave numerical simulation results, it is found that while the monomer-film system supports two hybridized dipole-like plasmon modes having different oscillating orientations and resonance strengths, the scattering spectrum of the dimer film-system features two additional peaks, one strong yet narrow resonant mode resembling a plasmonic dipolar mode, and one hybridized higher-order resonance mode, both polarized along the dimer axis. In particular, the stronger radiation efficiency and much narrower spectral linewidth of the dimer plasmon resonance, compared to its counterpart on silica substrate, are further addressed with an analytical multipole expansion model. The calculation results confirm that these new features are originated from an intense plasmon hybridization between a bonding dipolar mode along the dimer axis and a quadrupolar mode resulted from an anti-paralleled dipole bonding in direction perpendicular to the dimer axis, which reduces the far-field radiation loss and thus leads to the linewidth shrinking effect. These findings not only shed new lights on the plasmon hybridization between individual plasmon resonance modes but also open up the prospect for engineering resonance linewidth of coupled plasmonic modes in general nanoclusters by metal substrate mediated mode hybridization.

Based on the depended understanding of the gap plasmon properties as unraveled in the first part, we extend my work to explore their spectroscopy enhancement applications in the second half of this thesis. In light of the strong radiation efficiency and enhanced near-field intensity associated with the excitation of the dimer plasmon resonance, I have performed

photoluminescence spectroscopy measurements on the gold film-supported nanoparticle dimer system, and an emission intensity enhancement up to ~200-fold is demonstrated as compared to that of its counterpart on the glass substrate, showing excellent agreement with the calculation results (253-fold). The experimentally observed similar spectral characteristics of the plasmonic scattering and the photoluminescence emission indicate that the radiative decay of the hybridized dimer plasmons is the origin of the detected photoluminescence, which is further verified by the calculations with a proposed phenomenological model. Moreover, the calculation identifies that the particle-film gap junctions are dominantly responsible for the enhanced emission, implying that the metal film-coupled nanoparticle dimer system can be used as a versatile plasmonic platform simultaneously possessing an improved quality factor and a nanoscale mode volume for realizing light -matter interaction in the strong coupling regime that is of fundamental importance in cavity quantum electrodynamics (QED).

Finally, we turn our attention to the nonlinear optics aspect of the metal film-coupled gold nanospheres. In this part, we firstly demonstrate a large spectral tunability of the coupled structure in the visible and near infrared region by simply controlling the diameter of the gold nanosphere, and then we use a multiphoton spectroscopy and imaging system to explore its nonlinear optical properties. Upon resonant excitation by a pump femtosecond (fs) laser spectrally overlapping with the gap plasmon resonance, it is found that the nonlinear optical emission spectrum of the structure is featured with a pronounced narrow SHG emission peak and a broad TPL emission band, both of which shows significant enhancement in emission intensity compared to that of a gold nanosphere of the same diameter on silica substrate. More interestingly, the two-lobes shaped emission pattern of the observed SHG and TPL excited by the tightly focused linearly polarized fs laser beam, unambiguously evidences that the invoking of the dipolar gap plasmon resonance at the nanosphere-film vertical junction is dominantly responsible for the large nonlinear emission enhancement. Excellent agreement

between the nonlinear optical emission patterns with the calculated focal field distributions based on the vector diffraction theory suggests that the metal film-couple nanoparticles can be used as a sensitive plasmonic virtual probe for mapping the longitudinal electromagnetic fields in the focal plane.

List of Publications and Conference Presentations

Journal publications based on this thesis work:

([#] equally contributed, * corresponding author)

1. **G.-C. Li**, Y.-L. Zhang, and D. Y. Lei*, "Hybrid plasmonic gap modes in metal film-coupled dimers and their physical origins revealed by polarization resolved dark field spectroscopy," ***Nanoscale***, vol. 8, no. 13, pp. 7119–7126, 2016.
2. **G.-C. Li**, Y.-L. Zhang, Jing Jiang, Yu Luo, D. Y. Lei*, "Metal substrate mediated plasmon hybridization in a nanoparticle dimer for photoluminescence linewidth shrinking and intensity enhancement", ***ACS Nano***, vol. 11, no. 3, pp. 3067-3080, 2017.
3. **G.-C. Li**, S.-D. Liu, Y.-L. Zhang, D. Y. Lei*, "Gap plasmon enhanced nonlinear optical emission in metal film-coupled nanoparticles for longitudinal field mapping", manuscript under preparation, 2017.

Journal publications during my PhD study but not included in this thesis:

([#] equally contributed, * corresponding author)

4. S.-D. Liu, E. S. P. Leong, **G.-C. Li**, Y. Hou, J. Deng, J. H. Teng, H. C. Ong, and D. Y. Lei*, "Polarization-Independent Multiple Fano Resonances in Plasmonic Nonamers for Multimode-Matching Enhanced Multiband Second-Harmonic Generation," ***ACS Nano***, vol.

10, no. 1, pp. 1442–1453, 2016.

5. S. Zhang[#], **G.-C. Li**[#], Y.-Q. Chen[#], X.-P. Zhu, S.-D. Liu*, D. Y. Lei*, and H. Duan*, "Pronounced Fano Resonance in Single Gold Split Nanodisks with 15 nm Split Gaps for Intensive Second Harmonic Generation," ***ACS Nano***, vol. 10, no. 12, pp. 11105–11114, 2016.
6. S. Y. Choi, C. T. Yip, **G.-C. Li**, D. Y. Lei, K. H. Fung, S. F. Yu, and J. Hao, "Photoluminescence enhancement in few-layer WS2 films via Au nanoparticles," ***AIP Advances***, vol. 5, no. 6, p. 67148, 2015.

Conference presentations

1. **G.-C. Li**, D.Y. Lei, "Direct evidence of gap-mode induced nonlinear optical emission from gold nanoparticle-on-film system", Poster presentation, 两岸三地知名高校物理学科博士生学术创新论坛, Shanghai, 2015.
2. **G.-C. Li**, Y.-L. Zhang, and D. Y. Lei, "Hybrid plasmonic gap modes in metal film-coupled dimers and their physical origins revealed by polarization resolved dark field spectroscopy," Poster presentation, Young Giants of nanoscience 2016, Hong Kong, Jun. 2016.
3. **G.-C. Li**, Y.-L. Zhang, and D. Y. Lei, "Gap plasmon enhanced nonlinear optical emissions in single metal nanoparticles on mirror", Oral presentation, 第八届全国光学青年学术论坛, Hangzhou, China, Nov. 2016.

Acknowledgments

Many people deserve my incredible appreciation for their great support during my PhD study.

First of all, I would like to thank my supervisor Dr. Lei Dangyuan for offering me the opportunity to do my PhD study at PolyU. During the past three years, his enthusiasm and energy for research has consistently inspired me for academic novelty and grown me as a professional researcher. Under his supervision I have practiced the art of widely and efficiently collaborating with researchers across multidiscipline. Without his guidance and support, I would not be able to complete the thesis work on time and commerce on my extended research. I am also grateful for support from my co-supervisor Prof. Yu Siu Fung. My gratitude also goes to Prof. Ong Hock Chung and Dr Li Andrew at The Chinese University of Hong Kong for providing access to the fs laser system used in my study, as well as Dr. Cao Zhaolong for his valuable suggestions on constructing relevant experimental setups.

I have been privileged to collaborate closely with some senior researchers from other institutes, including Prof. Liu Shao-Ding at Taiyuan University of Technology and Prof. Duan Huigao at Hunan University. Furthermore, I would like to express my special thanks to Dr. Zhang Yong-Liang. Dr. Zhang is an expert on theoretical physics and has helped me a lot on physical explanation of my experimental observations. Many thanks also go to my group members: Mr. Bao Zhiyong, Mr. He Jijun, Dr. Duan Jinglai, Dr. Hou Yidong, Mr. Chen Fei, Mr. Filip Ligmajer, Mr. Zhu Yangzhi and Dr. Jia Guangyi.

Finally, I will show my deepest love to my family members for their encouragement and support throughout my life.

Table of contents

List of Figures

Nomenclature

MNPs	Metal Nanoparticles
SPRs	Surface Plasmon Resonances
SPP	Surface Plasmon Polaritons
LSP	Localized Surface Plasmon
LSPRs	Localized Surface Plasmon Resonances
TIR	Total Internal Reflection
CS	Cross Section
PH	Plasmon Hybridization
SERS	Surface-enhanced Raman Scattering
PL	Photoluminescence
CW	Continuous Wave
LSCM	Laser Scanning Confocal Microscopy
SH	Second Harmonic
SHG	Second Harmonic Generation
THG	Third Harmonic Generation
MWM	Multiple Wave Mixing
TPA	Two-Photons Absorption
TPL	Two-photon absorption induced Luminescence
CTAB	Cetyltrimethylammonium Bromide
RMS	Root-Mean-Square
SNR	Signal-to-Noise Ratio
SEM	Scanning Electron Microscopy
LDOS	Local Density of Optical States
FDTD	Finite Difference Time Domain
FEM	Finite Element Method
PML	Perfect Match Layer

FWHM	Full Width at Half Maximum
QED	Quantum Electrodynamics
NA	Numerical Aperture
TE	Transverse Electric
TM	Transverse Magnetic

Chapter 1 Introduction

1.1 Breaking optical diffraction limit for strong light-matter interactions

Light-matter interaction is the fundamentally important physical process in the universe - governing phenomena from atomic transitions to photo-synthesis on earth. Precise manipulation of this interaction has enabled various advanced technologies ranging from global telecommunication to signal detection in single-molecule level. On subwavelength scale, however, light-matter interaction is limited by the well-known optical diffraction limit, as evidenced by the weak and diffuse transmission of light through single subwavelength hole[1,2]. In fact, the optical diffraction limit was formulated in 1873 by German physicist Ernst Abbe during his attempt to improve the resolution of optical microscope. According to Abbe's theory, two features spaced closer than $\lambda/2n$ could not be resolved regardless of the precision improvement in optical lens fabrication. Equally, the smallest optical spot size obtained by optical focusing is limited to a lower bound as $\frac{1.22\lambda}{\mathrm{NA}}, < \lambda$, where NA is the numerical aperture of the objective. This limit severely hampers the ability to control the optical phenomena within the subwavelength scale.

In addition, strong light-matter interactions are frequently required in light emission applications such as surface-enhanced Raman scattering (SERS)[3], photoluminescence[4] and nonlinear optics[5]. Due to the ultra-low light conversion efficiency in these processes, excitation light with high optical intensity is highly demanded for considerable emission intensity in practice. The invention of laser in 1960 largely relaxed the requirements for

coherent light source with strong power, and offers significantly improved optical density by focusing into the spot size scaled down to the theoretical diffraction limit. However, confinement of light within subwavelength volume for higher optical density is still facing challenges. To break the optical diffraction limit for strong light-matter interactions, the physical phenomena associated with surface plasmon resonances (SPRs), as described in the following, have been demonstrated as a good candidate solution.

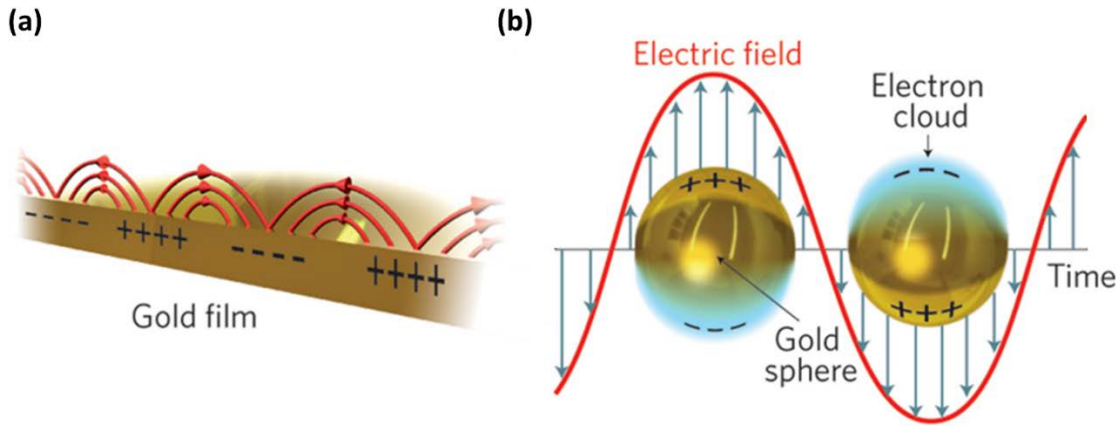

Figure 1.1 Illustration of surface plasmon polaritons and localized surface plasmons. Collective oscillation of electrons excited by incident electromagnetic field at gold-air interface (a) and in gold nanoparticles[6].

1.2 Surface plasmons polaritons and localized surface plasmons

Surface plasmon refers to the hybrid electron-photon oscillation occurred at the metal-dielectric interface[7]. While surface plasmons can occur at any metal-dielectric interface, the ones associated with the particles and planar geometrics have received most of the attentions in the past decades. The surface electromagnetic modes on the planar plasmon geometry, formally termed as surface plasmon polaritons (SPPs), are characterized by propagating charge density waves confined to the metal-dielectric interface as schematically depicted in Figure 1.1(a). Depending on the excitation wavelength and the specific metal/dielectric used,

the electromagnetic field penetration into the dielectric can be within the subwavelength scale. In comparison, the metallic particles sustain localized surface plasmons (LSPs), which, within electrostatic limits, resemble dipoles with clouds of charge localized at the surface poles as seen in Figure 1.1(b). Accordingly, the metallic nanostructures can act as optical antennas, concentrating incident light to a subwavelength volume, and thus break the optical diffraction limit, permitting a host of applications ranging from surface-enhanced Raman spectroscopy[8–10] to photothermal ablation in tumor therapy[11–13] and the development of efficient photovoltaic devices[14–16].

Because of the mismatch between the wave vector of light in free space and at the metal surface, direct excitation of SPP with electromagnetic waves is not possible. It can only be excited upon providing the missing momentum contribution[17]. This can be achieved by replacing the air with a high index dielectric, as shown in Figure 1.2. In contrast, the excitation of LSP in individual metallic nanoparticle can readily be achieved with direct coupling with the incident electromagnetic waves due to its non-propagating property (see more details in Chapter 2). This relaxation in optical excitation configurations largely expands its applications scope into the light spectroscopy[18–20] and optical manipulation[21–23] domains, etc.

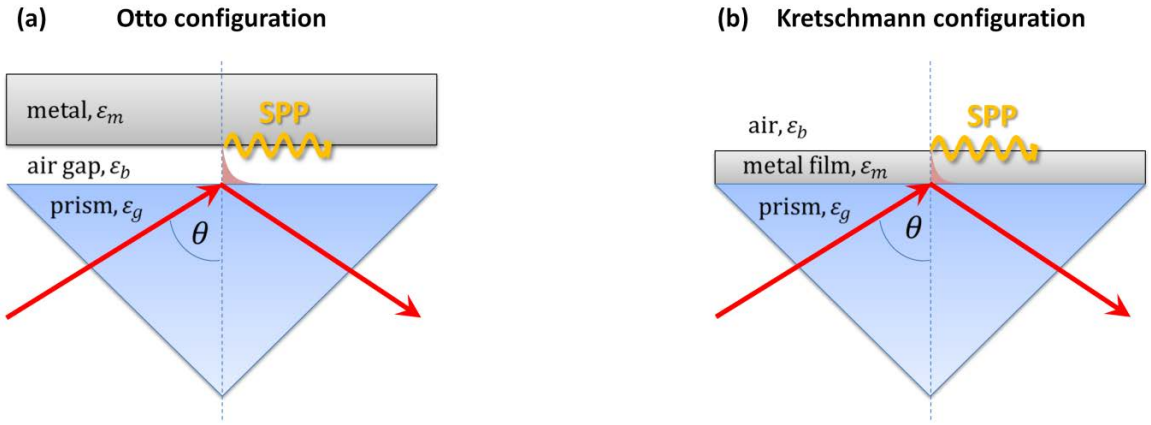

Figure 1.2 Two typical configurations that provide the momentum match discussed in the main text for activation of surface plasmon polaritons at the metal surface[24]. (a) Otto configuration: The total internal reflection (TIR) occurred at the prism-air interface generates an evanescent field that excites a SPP at the dielectric-metal interface. This is the preferred configuration when the metal surface should not be damaged, but it is challenging to keep a constant distance (within the wavelength scale) between the metal and the prism surface. (b) Kretschmann configuration: The metal film is directly attached to the prism surface and the TIR at the prism-metal interface generates an evanescent field exciting a SPP at the upper metal-air interface. Note that the thickness of the metal film should not exceed the penetration depth of the evanescent field.

Particularly, LSPs sustained in noble metal nanoparticles have received the intensive studies in fundamental researches and applications, not only because of their resistance to corrosion and oxidation in ambience, but also due to the strong electromagnetic resonances within the visible and near-infrared spectral band. These electromagnetic resonances, arising from the surface plasmon oscillations, determine the optical response of the metal nanoparticles. Upon illumination at the resonant wavelength, the nanoparticle is featured with a significantly increased extinction cross section compared to that of the off- resonance case (see Figure 1.3c, d), and experience much stronger light-matter interactions. When the metal nanoparticle is illuminated by white light, the color observed thus depends on the plasmon resonance wavelength as demonstrated in Figure 1.3a. Meanwhile, the resonant oscillation of the collective electrons with the incidence will create strong electromagnetic field confinement near the particle surface as depicted in Figure 1.3b. More intriguingly, the LSPRs is largely dependent on the particle size, geometry, material composite and the surrounding dielectric environment., thus enabling a flexible modification on their optical properties through synthesis or fabrication process control (Figure 1.3a).

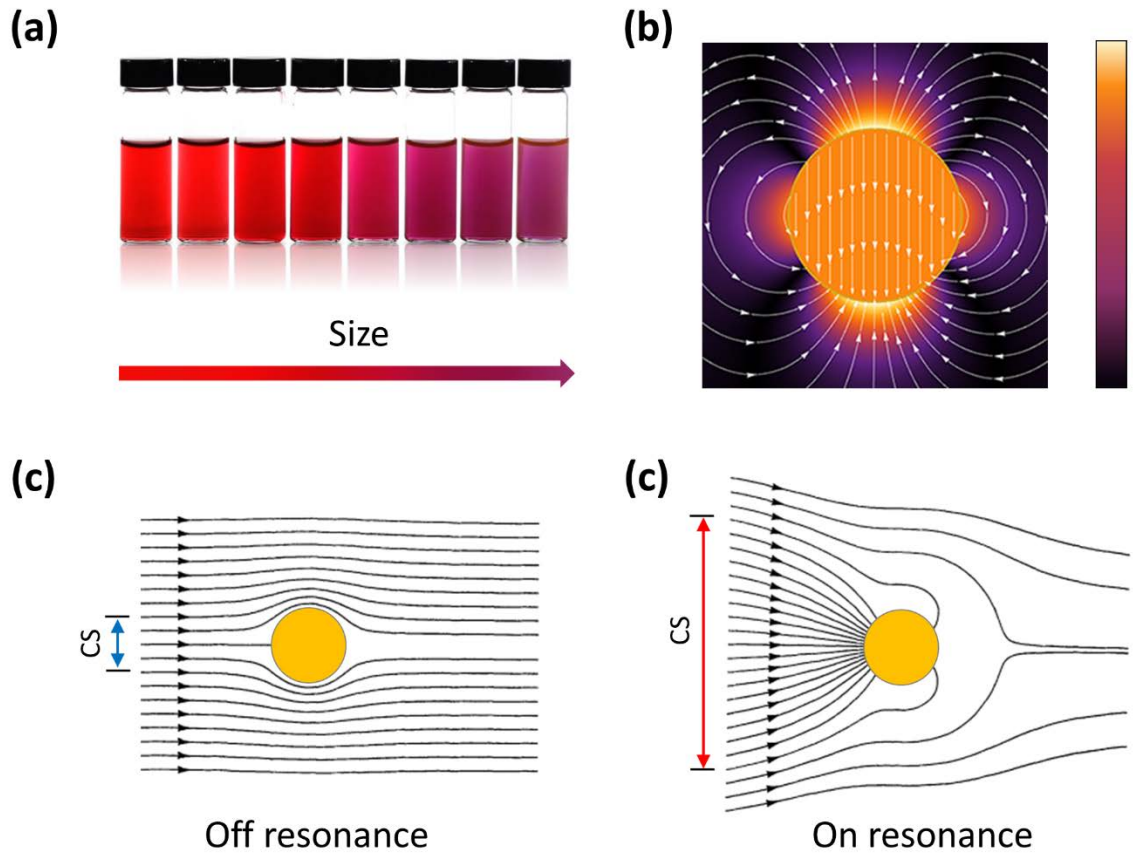

Figure 1.3 The optical properties of individual plasmonic nanoparticles. (a) The color appearance of the gold nanoparticles colloidal with increasing particle diameters. (b) Normalized field distributions of a gold nanoparticle upon excitation at the resonant wavelength 532 nm, the incidence polarization is along the vertical direction. (c-d) Field lines of the Poynting vector around a metal nanosphere under monochromatic light illumination off/on the resonant wavelength. Noted the scattered field is excluded for clarity[25].

1.3 Plasmon coupling for novel plasmonic properties

Apart from the localized surface plasmon resonances sustained in individual metal nanoparticles, many strategies using plasmon coupling have also been developed to create specific plasmon resonances through generating, for example, sub-radiant and super-radiant modes and plasmonic Fano resonances[26,27]. These methods have been applied in many new types of metallic nanostructures, such as nanoparticle clusters or oligomers made from

rational assembling of two or more individual nanoparticles into single symmetric or symmetric-broken entities[28–30] as partially concluded in Figure 1.4.

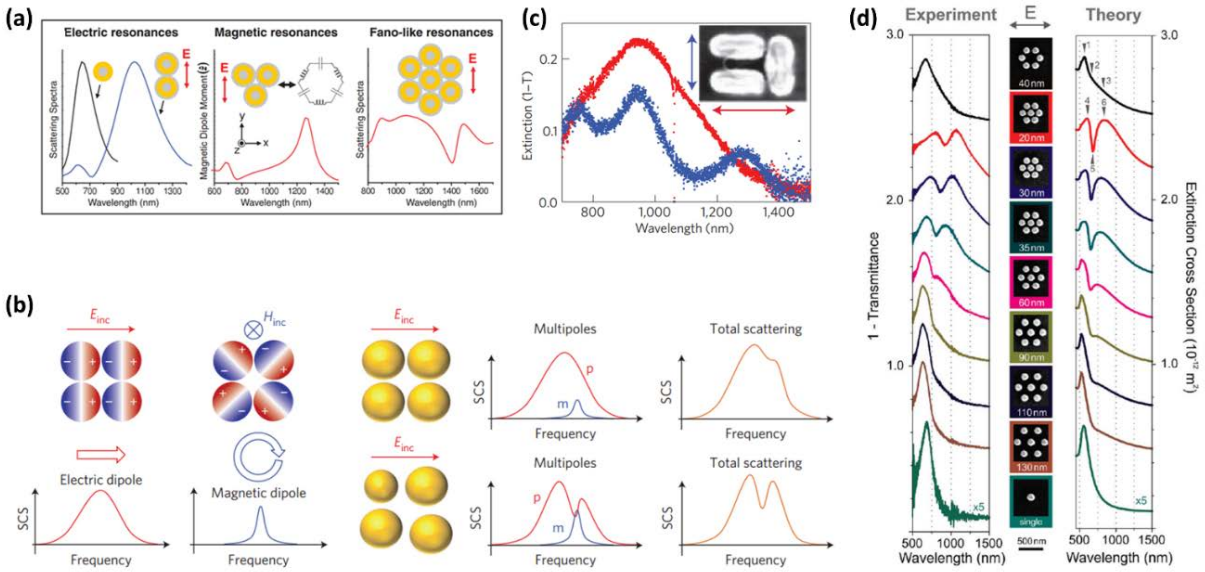

Figure 1.4 Rational assembling of individual nanoparticles into one entity to create new type of plasmon resonances. (a) Cluster of dielectric/metal core-shell structure nanoparticles[31]. The single particle possesses one dipolar plasmon resonance as manifested in the scattering spectrum. Upon a second particle brought in proximity, a bonding dipolar mode appears and shifts to the red spectral side (left column). In the nanoparticle trimer, a magnetic resonance emerges in the near-infrared wavelength band (middle column). The more complex heptamer cluster, in contrast, comes with a spectral dip as a result of the destructive interference between the broad dipolar mode and the narrow magnetic mode. (b) Metal nano-rings structure with tiny symmetry broken is featured with a pronounced Fano resonance due to induced interference between the dipolar plasmon mode and the magnetic mode[32]. (c) Experimentally observed individual dumbbell-like structure extinction spectrum for the two excitation polarizations indicated in the inset. The multiple Fano resonances arise from the interference between the spectrally broad dipole mode and higher electric modes[33]. (d) Extinction spectra of a gold nanoparticle monomer, a gold hexamer and heptamer clusters with different interparticle gap distances. In the monomer and hexamer, particle dipolar plasmon resonances are observed both experimentally and in simulation results. The transition from individual to collective modes is clearly visible when reducing the interparticle gap separations in the different heptamer clusters. Specially, a pronounced Fano dip appears in the spectra when the interparticle gap distance is decreased below 60nm[34].

Due to the strong capacitive electromagnetic interaction between constitute elements, these composite nanostructures are often featured with one or more near-field hot spots at the interparticle gap regions, which offer a promising platform for surface-enhanced Raman scattering and photoluminescence spectroscopy[35–37]. In particular, reducing the symmetry of a nanocluster system relaxes the selection rules of dipolar coupling, resulting in effective plasmon hybridization of dipolar and higher-order modes[38,39]. This coherent mode coupling provides, beyond the scope of simply tuning the plasmon resonance position by varying nanoparticle size and shape, important possibilities for engineering the resonance line-width and line-shape through radiative damping control[40,41].

The electromagnetic coupling between individual plasmonic nanoparticles to form a more complex plasmonic structure is in an analogy to the phenomenon in which atoms interact with each other to form a molecule. With the concept of atom hybridization, Perter Norlander et al. have proposed a hybridization model for the plasmon response of complex nanostructures[42], for which the complex plasmonic nanostructure can also been termed as "plasmonic molecules"[43]. The plasmon hybridization model can be readily understood in the illustration of the plasmon response of the simplest plasmonic molecule – a gold nanoparticle dimer. In direct analogy to the electron wave functions of two hydrogen atoms (H) mixing and hybridization to form molecular orbitals in a hydrogen molecule (H_2), when a second particle monomer is brought in close proximity, the LSPs in the two particles mix and hybridize, giving rise to the formation of bonding and antibonding plasmonic modes[44] as schematically illustrated in Figure 1.5b. Particularly, some of the hybridized modes have a net nonzero dipole moment, like the longitudinal bonding dipole mode in the dimer, and thus can decay radiatively into the far field, manifesting themselves in the scattering spectrum as in Figure

1.5c. Accordingly, this kind of plasmon mode is called bright mode or superradiant mode as aforementioned. In contrast, the dark plasmon modes are featured with a net zero dipole moment, such as the longitudinal antibonding and transverse bonding modes in Figure 1.5b. Due to the weak coupling with the incoming electromagnetic waves, these plasmon modes cannot be directly activated under linearly polarized illumination, and in turn, other excitation schemes are required to invoke these modes, such as the focused electron beams[45,46], by using tailored illumination configurations like spatially inhomogeneous fields[47], evanescent excitation[48], tilted incidence beam[27], spatial phase shapping[49] and more subtle retardation effects[50]. Additionally, resonant excitation of these hybridized plasmons will result in an electromagnetic hot spot within the gap region, which offers a nanoscale cavity with ultra-small mode volume for strong light-matter interactions[36,51,52].

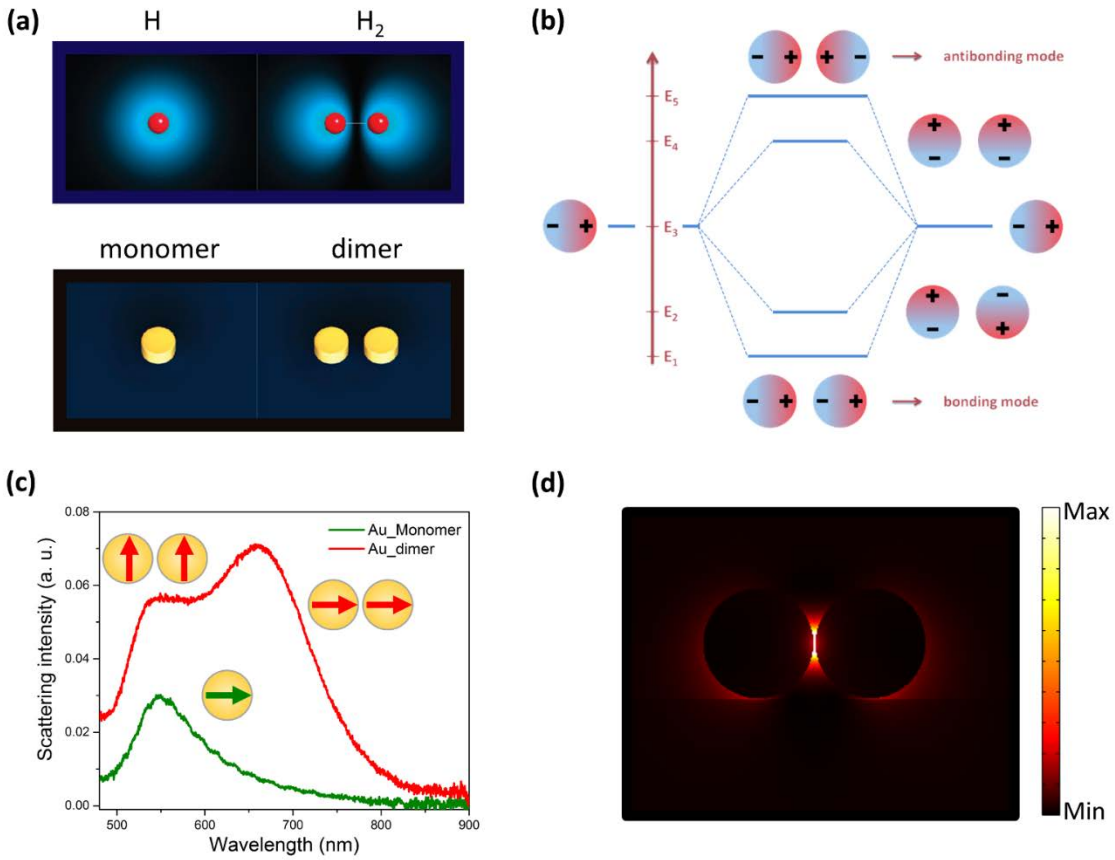

Figure 1.5 Plasmon resonances in coupling nanostructures. (a) Illustrations of the molecular configurations of an H atom and an H2 molecule (upper panel). Their plasmonic analogues – a gold nanoparticle monomer and dimer (bottom panel). (b) Energy levels of two coupled nanosphere particles described by the plasmon hybridization model. The dipolar plasmon resonance of each particle couples to that of the other one in different manners, forming the bonding and antibonding modes[47,53]. (c) The coupled dipolar plasmon resonances manifested in the scattering spectrum of a gold nanoparticle dimer on glass substrate. The dipolar plasmon resonance in single particle monomer is also depicted for comparison. (d) Filed intensity distribution of the metallic nanoparticle dimer (100 nm in diameter of each constituent particle) at the plasmon resonance wavelength 650 nm as marked in (c).

1.4 Metal film-coupled nanoparticles for enhanced spectroscopy

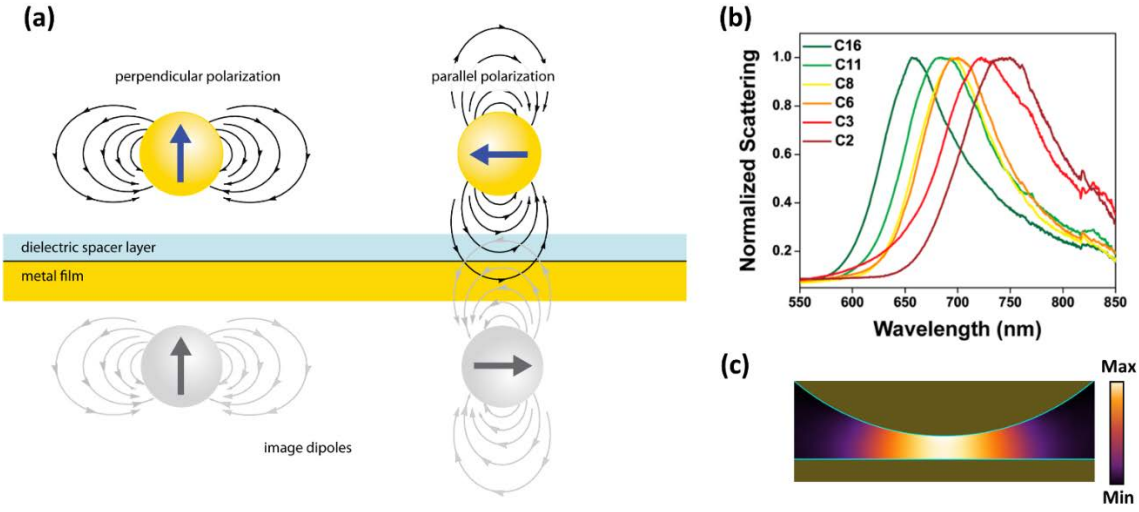

Figure 1.6 Optical properties of metal film-coupled nanoparticles. (a) Schematics of the electromagnetic interaction between the metal nanoparticle and the underlying film[54]. Here, the dipole-image model is used to account for the optical response of the metal particle-films system within the electric-static approximation. In this manner, the optical properties of the metal film coupled nanoparticles resemble that of a metal nanoparticle dimer in the vertical direction. (b) The gap distance dependence of the plasmon resonances manifested in the scattering spectrum of the gold film coupled nanosphere nanoparticles[55]. By decreasing the particle-film gap distance, the gap plasmon resonance spectrally shifts to the red side and broadens. (c) Electric field intensity distribution within the gap region in the metal film supported nanoparticles at the gap plasmon resonance wavelength. Note that the field is highly concentrated within the nanoscale volume inside the gap.

Nowadays, most of the composite plasmonic nanostructures are fabricated with lithographic method which limits the achievable gap size above sub-10s nm region, or formed by self-assembling of nanoparticles in an in-plane arrangement. In the latter scheme, although the sub-nanometer gap size can be realized, achieving tunable optical response though readily control over gap distances still faces great challenges. More importantly, the feasibility of precisely loading of active molecular emitters or the hot 2D materials into these nanoscale gap cavities, which is of crucial importance in cavity quantum electrodynamics[56,57] and ultra-small

spaser technology[58], also remains largely hindered due to the difficulty of the in-plane arrangement. In this regard, the metal film coupled plasmonic nanostructures seems to be a good candidate solution, which have received intensive studies in the past decade[59–64]. Benefiting from the well-established technologies in planar film deposition and spacer fabrication[55,65], the particle-film gap distances can not only be precisely controlled for tunable optical properties in these composite nanostructures[54] (see Figure 1.6b), but also can be scaled down to the sub-nanometer regime for addressing nonlocal effect [66]and quantum mechanics[67]. Moreover, the achievable ultrasmall nanocavity mediated by the particle-film gap can largely facilitate the accessibility of various active monolayer molecules or 2D materials[68], forming a promising platform responsible for a series of breakthroughs in nanophotonic applications such as deep subwavelength plasmonic lasers[69], huge spontaneous emission enhancement[70,71], and recently, even realization of single molecule-light strong coupling at room temperature[72]and single molecule optomechanics in "pico-cavities"[73].

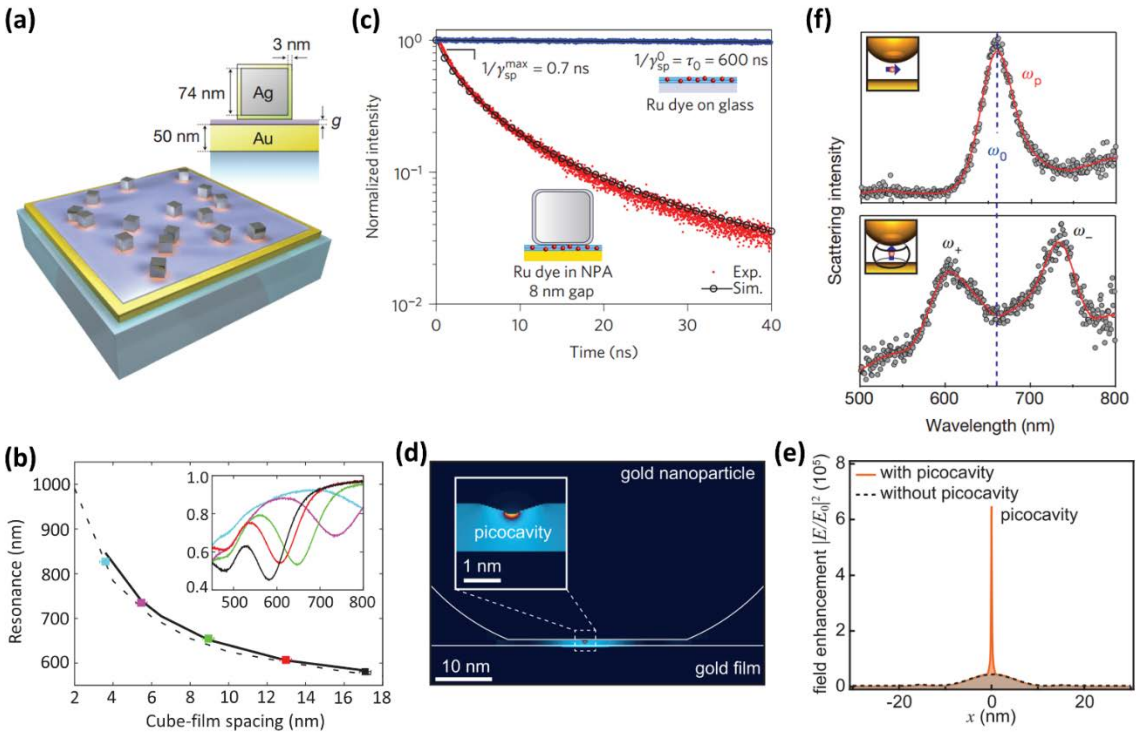

Figure 1.7 A series of breakthroughs in fundamental and applied nanophotonics based on the metal nanoparticle-film platforms. (a-b) Controlled-reflectance surfaces achieved with film-coupled colloidal nanocubes[74]. (c) Large Purcell factor of the metal film-particle cavity for spontaneous emission enhancement[71]. (d-e) Demonstration of the single- molecule optomechanics in the gold nanoparticle-film mediated picocavities[73]. (f) Achievement of single-molecule strong coupling at room temperature in the sub-nanoscale particle-film cavity[75]. The Rabi splitting is clearly visible when the dipole moment of single molecule aligns along the dominant field component in the gap (bottom panel).

1.5 Photoluminescence and second harmonic generation in metals and their nanostructures

1.5.1 Photoluminescence

Like the semiconductors or fluorophores, the inter-band transitions in noble metals upon light excitation can also occur, leading to single photon absorption induced luminescence – photoluminescence which was firstly observed by Mooradian in 1969[76]. Particularly, for bulk gold – the mostly used raw material for plasmonic nanostructures, it has been found the emission originates from the radiative combination of electrons in the *sp*-band with holes in the d-band, quite analogy to the optical transitions in fluorophore as depicted in Figure 1.8a. However, the emission quantum efficiency is rather low, which is estimated to be on the order of 10^{-10}. In 1986 Boyd et al. reported significantly enhanced photoluminescence (quantum efficiency $\sim 10^{-6}$) from roughed metal films and a detailed model in terms of band structure and electromagnetic filed enhancement has been developed to account for the increased emission intensity[77]. Together with a series of observations of PL enhancement in nanostructured metals subsequently, it has been concluded that the surface plasmons must play a crucial role in the emission enhancement[78–81], which will be discussed in more details

in chapter 6. Together with the absence of irreversible photo-bleaching upon laser exposure, the gold nanoparticles and clusters bear large potential as label-free fluorophores in bioimaging[82,83] and optical switch units for data storage[84].

While the single-photon luminescence process corresponds to absorption of a higher energy photon and subsequent generation of a lower energy photon, the two-photon absorption (TPA) induced luminescence involves absorption of two photons simultaneously and subsequent emission of a higher energy photon similar to the single-photon emission process[77] (right: Figure 1.8a). Since the cross section of the two-photon absorption in noble metals is of several orders smaller than that of the single-photon absorption, the emission probability is ultralow and large excitation intensity is necessary to be high. This is why two-

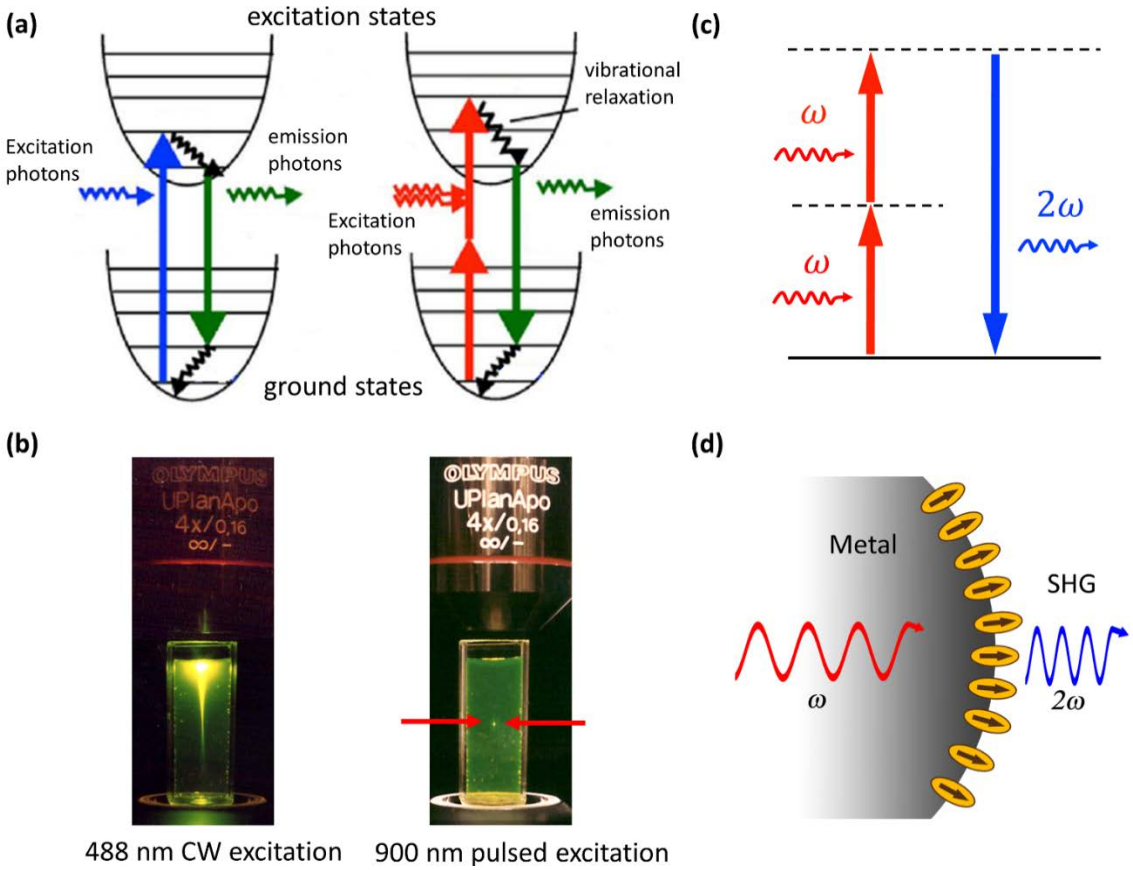

Figure 1.8 Illustrations of the photoluminescence, two-photon luminescence and second harmonic generation in fluorophore or metals. (a) Jablonski diagram for single-photon (left) and two-photon (right) absorption induced optical emission. Excitation occurs between the ground states and the first electronic excited states. Single-photon excitation occurs through the absorption of one photon, while two-photon excitation occurs upon the absorption of two photons of lower energy via short-lived intermediate states. After each of the excitation process, the fluorophore relaxes to the lower energy levels of the excitation states via vibrational processes. The subsequent photons emission processes for both modes share the same mechanics[85]. (b) Experimental demonstration of the excitation of single- and two-photon luminescence excitation in spectroscopy[86]. As can be seen, the emission of the TPL is confined in the very small volume at the focal spot. (c) Schematic of the up-conversion process of second harmonic generation. (d) Illustration of the origins of SHG in bulk metals. Noted the SHG emission originates mainly from the nonlinear polarization by norm field components at metal surface.

photon luminescence of various fluorophore can usually be observed upon excitation by pulsed laser with high peak power density[87–89], which is, however, still far from sufficient for the non-bleaching metallic structures. The surface plasmons in metal nanostructures significantly relax this requirement by introducing large local field enhancement upon resonant excitation, boosting the TPL emission intensity on several orders of magnitudes[90–92]. More importantly, the excitation of two-luminescence occurs only at the location with high optical power density, as illustrated in Figure 1.8b. This extreme confinement of excitation into sub-micrometer scale renders the TPL microscopy automatically a confocal configuration advancing the concurrent laser scanning confocal microscopy (LSCM) system and promising technique for high resolution and background-suppressed imaging[93–95] and revolutionary optical data storage[96].

1.5.2 Second harmonic generation

Boosting the efficiency of nonlinear optical processes in extremely confined volumes remains challenging in nano-optics research[97], but are importantly required in applications in optical frequency convertor[98], photocatalysis[15], nanomedcine[99], and back-ground-free biosensing[100].

Plasmonic nanostructures has often been utilized to foster various nonlinear optical effects such as second/third harmonic generation[101–104] and four-waves mixing (FWM)[105,106]. As the simplest nonlinear optical phenomenon - second harmonic generation, actually, can be described by a three-wave mixing process (Figure 1.8c). In this process, the absorption of two photons at the excitation wavelength results in a SH photon emission at exactly twice the energy of the pump photon. This effect is physically forbidden in centrosymmetric bulk materials (like metals: Au, Ag, etc.) within the electric dipole approximation. However, SHG emission can be expected in plasmonic nanostructures enabled by the centrosymmetry breakdown at metal surfaces (Figure 1.8d)[107–111]. Particularly, the strong local field intensity upon resonant excitation of the plasmon resonance can significantly boost the pump rate for nonlinear polarization at the metal surface[112–118], and dominates the far-field SHG emission enhancement. Additionally, the practical SHG conversion efficiency measured in spectroscopy experiments also depends on the antenna efficiency of the plasmonic structure at the SH frequency, pushing the design and fabrication of nanoscale plasmon entities for higher SH conversion efficiency toward the double-mode configuration matching the excitation and emission spectrally and spatially at one time[98,119,120].

1.6 Outline of thesis

In light of the advantages of the metal film-coupled nanoparticles over other coupling resonators as stated above, the main research content of this thesis will start with explore of the gap plasmon modes in these nanostructure, with particular attentions paid on the complex gold nanoparticle dimers on film configuration, and the characteristics of its optical properties both in the near- and far-field domain. The focus will be casted on the gap plasmons enhanced photoluminescence and second harmonic generations in this metal-film coupled nanoparticle systems. In details, the contents will be arranged as follows:

Chapter 2 will present a brief overview of the theoretical background for description of optical responses in plasmonic entities within the frame work of classic electromagnetic field theory, including the introduction of Maxwell's equations, the dielectric functions of metals, derivation of the surface plasmons, analytical models for plasmon couplings and some fundamentals for nonlinear optics of metal materials.

In the first part of chapter 3, I will give a detailed introduction on the sample fabrication method, and then in the second part, I will list the various technique tools and instrumental systems for experimental characterization of the plasmonic responses of metal film-coupled nanoparticles and perform the versatile light spectroscopy.

Chapter 4 present a thorough study on the distinctive plasmon response of both the gold film-coupled nanoparticle monomers and dimers with the polarization resolved dark field spectroscopy method. Correspondingly, full wave simulations are also performed to confirm the origins of the plasmon modes revealed experimentally.

In chapter 5 and 6, a detailed comparison of gold nanoparticle dimers on the gold film and glass substrate will be carried out, which includes the plasmon linewidth, radiation

intensity, and photoluminescence emission. Electromagnetic simulations and calculations are performed to account for the various contrast observations in experiments.

The study on nonlinear optical aspect of the metal film-coupled nanoparticles will be presented in chapter 7. There the multi-photon spectroscopy experiments are performed over the nanoparticles on both gold film and glass substrate. To illustrate the observed nonlinear optical emission features, the nonlinear perturbative model and vectorial diffraction theory are introduced to confirm the dominant contribution of the gap plasmon resonance in the nanoparticle coupled to film.

In the end, conclusion and outlooks are presented in chapter 8.

Chapter 2 Theory Background

The metal nanoparticles and nanostructures of interest in this thesis are situated in the gray zone between the micro- and macrocosm – they are quite small compared to the classical objects while still consist of several thousands to millions of atoms. Actually, surface plasmons are of bosonic type quasi-particles[121] and intrinsically have a quantum nature as demonstrated by the tunneling experiments[122]. Hence, for the analytical description one can either apply the quantum electrodynamics model from the bottom side or deal with the plasmonic entities with the classical field theory (given the nanostructures are not too small). Recent reports pointed out that for structure size below 5 nm, the concept of a dielectric function involved in the classical field theory becomes questionable[121,122]. At the same time, if the gap between constitute elements in coupled nanoparticles approach 1 nm, the emergent screening effect and electron tunneling across the particle gap region would significantly modify the optical properties as reported by Peter Norlander et al[123]. The author presented a fully quantum mechanics treatment of the nanoparticle dimers and stated that the quantum effects in dimer gap can't be neglected when the gap distance is below 1 nm. As will be seen in the following chapters, the plasmonic nanostructures under study are all situated above the justification size points and therefore the classical electrodynamics is fully competent for dealing with interactions between light and plasmonic structures as in our case. As a result, I will start this chapter with an introduction of the Maxwell's equations from which the concepts of linear and nonlinear polarization are briefly discussed. Then, a large portion of sections are casted into the dielectric functions of the plasmonic metals and the analytical model for the surface plasmons at metals and their nanostructures. Finally, a detailed analytical description of the second harmonic generation in metal nanostructures is presented

and their physical origins are also clearly classified.

2.1 Maxwell's equations for classic field theory

As the fundamental formulas in the classic electrodynamics, Maxwell's equations read:

$$\nabla \cdot D(r,t) = 4\pi\rho(r,t) \tag{2.1}$$

$$\nabla \cdot B(r,t) = 0 \tag{2.2}$$

$$\nabla \times E(r,t) = -\frac{1}{c}\frac{\partial B(r,t)}{\partial t} \tag{2.3}$$

$$\nabla \times H(r,t) = \frac{4\pi}{c} j + \frac{1}{c}\frac{\partial D(r,t)}{\partial t} \tag{2.4}$$

Here B is the magnetic field, D is the dielectric displacement, ρ the charge density, j the current density and c the speed of light in vacuum.

Maxwell's equations in many cases are linear in the E and B fields, of which it's sufficient to only investigate their possible solutions in the form of time harmonic fields. Any other complex solutions can then be viewed as superposition of them. Therefore, one use

$$E(r,t) = E(r)e^{-i\omega t}\ , B(r,t) = B(r)e^{-i\omega t} \tag{2.5}$$

Given that no sources are present ($\rho = 0, j = 0$), Maxwell's equations are reduced to

$$\nabla \cdot E = 0, \qquad \nabla \times B = \frac{1}{c}\frac{\partial E}{\partial t} \tag{2.6a}$$

$$\nabla \cdot B = 0, \qquad \nabla \times E = \frac{1}{c}\frac{\partial B}{\partial t} \tag{2.6b}$$

Under external excitations, the electrons bounded to an atom in the material response as the forced oscillators. In this way, the macroscopic polarization of the material induced by the cumulative effect of all displaced electrons, can thus be directly related to the net charge

distributions. Formally, the electric and magnetic inductions in material obey the following constitutive relations

$$D = E + 4\pi P, \qquad B = H + 4\pi M \tag{2.7}$$

where P refers to the dipole moment associated with single unit volume and M is the magnetic moment per unit volume. Since our attentions are only paid to the non-magnetic materials, one can set $M = 0$ and combine Maxwell's equations to

$$\nabla^2 E - \nabla(\nabla \cdot E) = \frac{1}{C^2}\frac{\partial^2 E}{\partial t^2} + \frac{4\pi\partial^2 P}{c^2 \partial t^2} \tag{2.8}$$

Considering the extreme high electric fields intensity (up to $10^9 V/cm$) in an atom or molecule, the αth component in Cartesian frame of the dipole moment $P(r,t)$ per unit volume can be formulated with a Taylor series in powers of the macroscopic electric field $E(r,t)$ as below:

$$P_\alpha(r,t) = P_\alpha^{(0)} + \sum_\beta \left(\frac{\partial P_\alpha}{\partial E_\beta}\right) E_\beta + \frac{1}{2!}\sum_{\beta\gamma}\left(\frac{\partial^2 P_\alpha}{\partial E_\beta \partial E_\gamma}\right) E_\beta\, E_\gamma + \frac{1}{3!}\sum_{\beta\gamma\delta}\left(\frac{\partial^3 P_\alpha}{\partial E_\beta \partial E_\gamma \partial E_\delta}\right) + \cdots. \tag{2.9}$$

here $E_\beta = E_\beta(r,t)$,with $\beta \in \{x,y,z\}$, are the three Cartesian components of the electric field. In dielectric materials, the electric dipole moment at zero field, $P_\alpha^{(0)}$ vanishes. One can thus write

$$P_\alpha(r,t) = \sum_\beta \chi_{\alpha\beta}^{(1)} E_\beta + \sum_{\beta\gamma} \chi_{\alpha\beta\gamma}^{(2)} E_\beta E_\gamma + \sum_{\beta\gamma\delta} \chi_{\alpha\beta\gamma\delta}^{(3)} E_\beta E_\gamma E_\delta + \cdots, \tag{2.10}$$

where $\chi^{(i)}$ are the susceptibilities tensors of $(i+1)-th$ rank. Accordingly, $\chi^{(1)}$ is the ordinary linearly susceptibility relating the electric field with the dipolar polarization. $\chi^{(2)}$ and $\chi^{(3)}$ are the second and third order susceptibilities, respectively. Therefore, the dipole moment can be formally decomposed into a linear part and a nonlinear part as

$$P_\alpha\,(r,t) = P_\alpha^{(L)}(r,t) + P_\alpha^{(NL)}(r,t) \tag{2.11}$$

where

$$P_\alpha^{(L)}(r,t) = \sum_\beta \chi_{\alpha\beta}^{(1)} E_\beta \tag{2.12a}$$

$$P_\alpha^{(NL)}(r,t) = \sum_{\beta\gamma} \chi_{\alpha\beta\gamma}^{(2)}\, E_\beta E_\gamma + \sum_{\beta\gamma\delta} \chi_{\alpha\beta\gamma\delta}^{(3)} E_\beta E_\gamma E_\delta + \cdots, \tag{2.12b}$$

Thus, the previously discussed relation in equation (2.7) can be simplified as

$$D = E + 4\pi P = (1 + 4\pi\chi_e)E = \varepsilon E \tag{2.13}$$

Accordingly, all nonlinear effects are related to the higher order susceptibilities. Since *P* and *E* are vectors, and are intrinsically odd under inversion symmetry. This makes $\chi^{(2)}$ vanishes in any medium that is invariant in form under inversion[124]. However, if the symmetry is broken (for example, at the interface between two different medium) or in the case of surface distortions[125], $\chi^{(2)}$ contributions for centrosymmetric materials (like gold or silver) can also be achievable[126].

2.2 Dielectric functions of metals

As illustrated in in equation (2.13), the permittivity ε determine how the material responses to the external electromagnetic field, and thus is fundamentally important for derive the optical properties of metals involved in the plasmonic nanostructures in our study. In the following, some details about the determination of dielectric functions of the noble materials will we presented.

To describe the response of metal, Paul Drude[127] proposed a classical theory based on nearly free electron model, and derived the equation of motion of electrons moving between the periodically arranged ions background. This model was further advanced by Arnold Sommerfeld[128] and Hans Bethe[129] and ends today with a general form

$$m_{\mathrm{e}}\frac{\partial^2 r}{\partial t^2}+m_{\mathrm{e}}\gamma_{\mathrm{d}}\frac{\partial r}{\partial r}=eE_0e^{-i\omega t} \qquad (2.14).$$

where γ_{d} represents a phenomenological damping term, m_{e} refers to the effective free electron mass, e is the free electron charge and ω and E_0 are the frequency and amplitude of the applied electric field, respectively. Equation (2.14) can be analytically solved with the ansatz form $r(t)=r_0e^{-i\omega t}$ by which the dielectric function can be directly obtained as

$$\varepsilon_{\mathrm{d}}(\omega)=\varepsilon_\infty-\frac{\omega_p^2}{\omega^2+i\gamma_{\mathrm{d}}\omega}, \qquad \text{with} \qquad \omega_{\mathrm{p}}=\sqrt{\frac{4\pi n_{\mathrm{e}}e^2}{m_{\mathrm{e}}}} \qquad (2.15).$$

here ω_{p} is the bulk (or volume) plasmon frequency (with electron density $n_{\mathrm{e}}=3/4\pi r_s^3$, the electron gas value r_s takes the value 0.16 nm for noble metals such as gold or silver) and ε_∞ corresponds to the ionic background in metal. Neglecting γ_{d} and ε_∞ for the moment, equation (2.15) can be simplified to

$$\varepsilon_{\mathrm{d}}=1-\frac{\omega_{\mathrm{p}}^2}{\omega} \qquad (2.16).$$

Then, two frequency regions can be clearly distinguished: ε_{d} is positive if $\omega>\omega_{\mathrm{p}}$, and the refractive index $n=\sqrt{\varepsilon_{\mathrm{d}}}$ is a real quantity. When $\omega<\omega_{\mathrm{p}}$, ε_{d} is negative and correspondingly n is imaginary, implying that electromagnetic waves with frequency in this region cannot propagate in the bulk medium.

Specifically, some typical metals possess values of ω_{p} lying in the ultraviolet region, which just accounts for the shiny and glittering appearance in the visible spectrum. Light waves with lower frequencies ($\omega<\omega_{\mathrm{p}}$) are reflected, because the oscillating electrons in the metal screen the incident electromagnetic radiations. In contrast, light waves with frequencies above the bulk plasma frequency ($\omega>\omega_{\mathrm{p}}$) get transmitted (the metal seems transparent to the light), since the motions of electrons in metal are too slow and fail to quickly respond to the fast oscillations of the high frequency fields.

The free electron gas model gives quite accurate dielectric parameters for describing the optical properties of metals at frequencies far away from the bulk plasmon frequency ω_p. At higher-energy frequencies, especially near or above the ω_p, interband transitions of bond electrons from the d bands into the sp bands are significantly promoted[130] (see Figure 2.1) and thus the Drude model is inaccurate for the visible region of the spectrum as indicated in Figure 2.2.

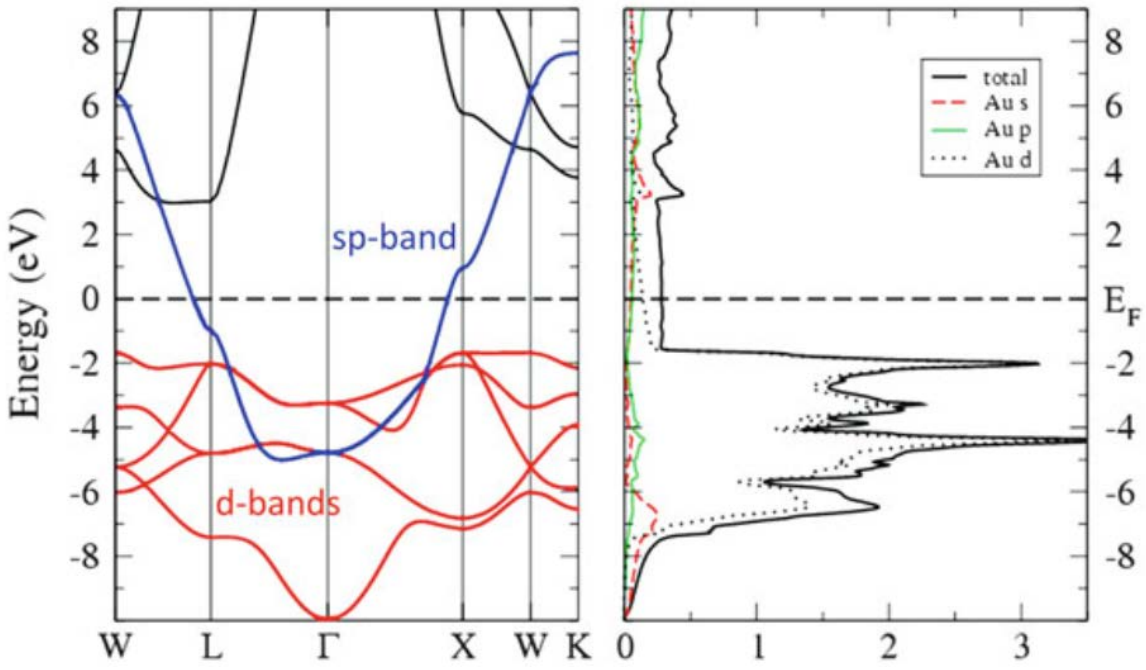

Figure 2.1 Electron band structure of gold obtained with first-principle calculations. The parabolic sp-bands, with energy roughly proportional to momentum spared, explain why the Drude model works well for most metals. Within the spectral regions above 2 eV, electrons can be significantly promoted from the lower d-bands to states in sp-bands above the Fermi energy level, leading to strong plasmon damping and absorption induced interband transitions[131].

Generally speaking, the dielectric function can fully describe the optical response of a material and can be exactly calculated with the first principle approach or obtained from measurements. In all the electromagnetic simulations performed throughout this thesis, the

dielectric data obtained from measurements by Johnson and Christy[132] are used.

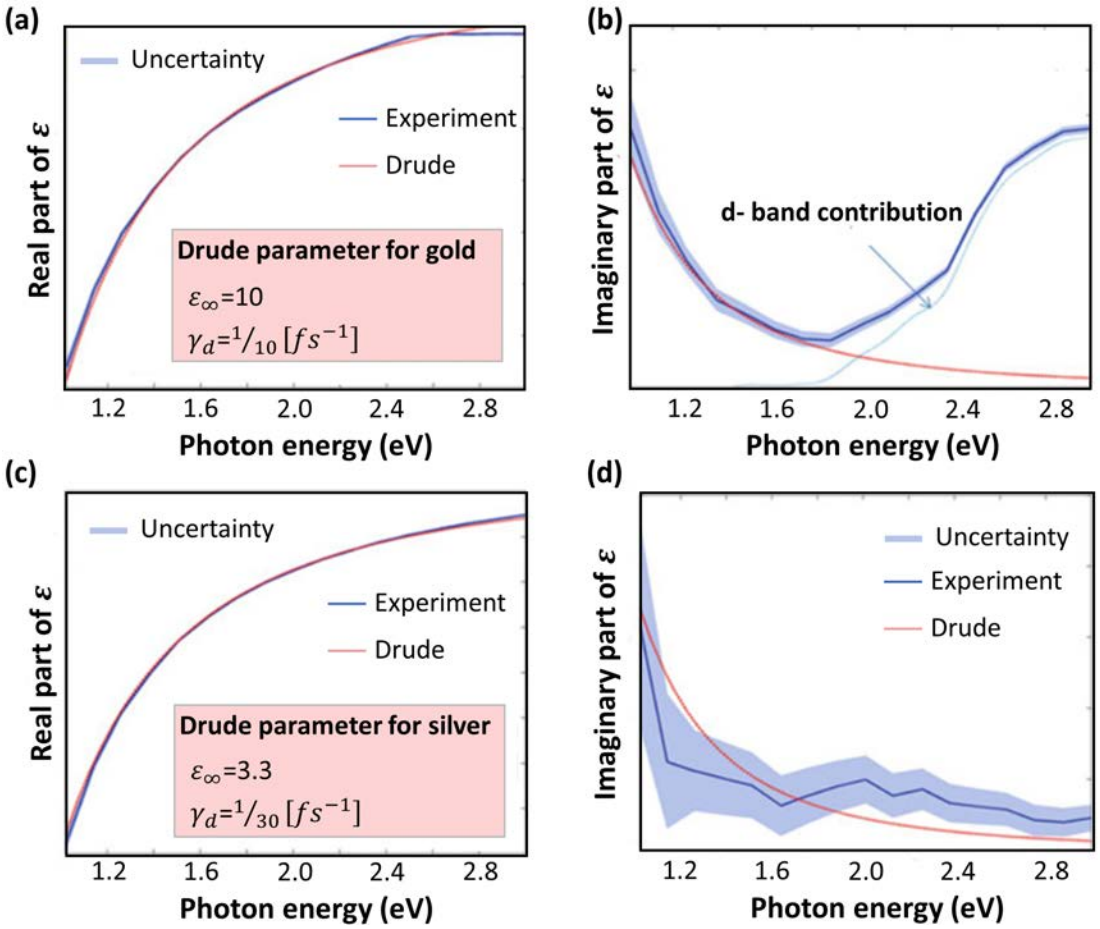

Figure 2.2 Dielectric functions of gold (silver) obtained by Drude model and experiment measurements, respectively[24]. Real and imaginary parts for gold in (a-b) and for silver in (c-d). Note the imaginary parts of the dielectric function for gold given by Drude model (in b) becomes invalid for frequency energies above 1.9eV, because at this frequency regions interband transitions are involved. The curve representing the d-band contribution depicted in (b) is obtained by direct comparison between the Drude model and the experimental measurements.

2.3 Theoretical description of Surface plasmon polaritons and localized surface plasmons

2.3.1 Propagating surface waves at interface

Before deriving the surface waves from Maxwell's equations, some simplifications are made by introduction of electromagnetic potentials in further processing. Firstly, we consider the frequency domain Maxwell's equation in free space:

$$\nabla \cdot D(r,\omega) = 0 \quad \nabla \times B(r,\omega) + i\omega D(r,\omega) = 0 \tag{2.17a}$$

$$\nabla \cdot B(r,\omega) = 0 \quad \nabla \cdot B(r,\omega) - i\omega B(r,\omega) = 0 \tag{2.17b}$$

Taking the curl on equations of Ampère's and Faraday's law and performing the variables substitute lead to the wave equation for electromagnetic fields of Helmholtz form

$$\left(\nabla^2 + \varepsilon \frac{\omega^2}{c^2}\right) \begin{Bmatrix} E(r,\omega) \\ B(r,\omega) \end{Bmatrix} = 0 \tag{2.18}$$

This equation lies in the central results of Maxwell's equations, since it predicts the existence of electromagnetic waves. By introducing the vector potential A and the scalar potential φ we can combine the four expressions of Equation (2.17) into two new equations as listed below

$$B = \nabla \times A \tag{2.19a}$$

$$E = -\nabla\varphi + ikA \tag{2.19b}$$

Governed by the gauge invariance of potentials, A and φ can be chosen in such a way that they are directly correlated by the Lorenz condition

$$\nabla \cdot A - ik\varepsilon\varphi = 0 \tag{2.20}$$

This condition is coordinate independent and leads to two separate wave equations for A and $\emptyset$, which completely equal to the Maxwell's equations (2.1):

$$\nabla^2\varphi + k^2\varepsilon\varphi = -4\pi\rho \tag{2.21a}$$

$$\nabla^2 A + k^2 \varepsilon A = -\frac{4\pi}{c} j \qquad (2.21b).$$

To derive the analytical form of the surface plasmons, a planar interface between a dielectric with dielectric (ε_b) at $z > 0$ and a metal (ε_m) at $z < 0$ is brought into consideration. The electric field $E(r,t)$ in wave equation (2.18) now will be solved separately in each medium and matching of the two solutions at the interface is guaranteed by the corresponding boundary conditions. In general, two independent sets of self-consistent solutions fulfill the Maxwell's equations. One is the TM mode polarized along the incidence plane ($k0z$), and the other one is the TE mode polarized orthogonally to the incidence plane. Here only the TM mode is responsible for the surface plasmon excitation, we can thus neglect the latter one and write down the solution as[130]

$$E_j = \begin{pmatrix} E_{x_j} \\ 0 \\ E_{z_j} \end{pmatrix} e^{ik_x x - i\omega t} e^{ik_{z_j} z}, \qquad j = 1,2. \qquad (2.22).$$

Note that the index $\boldsymbol{j}$ labeling the medium is omitted because the component $\boldsymbol{k_x}$ parallel to the interface is conserved in both mediums. The boundary conditions at the interface give rise to the following relation

$$E_{x_1} - E_{x_2} = 0 \qquad (2.23a).$$

$$\varepsilon_1 E_{z_1} - \varepsilon_2 E_{z_2} = 0 \qquad (2.23b).$$

These relations mean the field component parallel to the surface is continuous, whereas the perpendicular one is discontinuous across the interface. The dispersion relation in each medium reads

$$k_x^2 + k_{zj}^2 = \varepsilon_j k^2 = \varepsilon_j \left(\frac{\omega}{c}\right)^2 \rightarrow k_{zj} = \sqrt{\varepsilon_j \left(\frac{\omega}{c}\right)^2 - k_x^2}, j = 1,2. \qquad (2.24).$$

This directly results in the plasmon dispersion relation between the angular frequency and the wave vector

$$k_x = \frac{\omega}{c}\sqrt{\frac{\varepsilon_1\varepsilon_2}{\varepsilon_1+\varepsilon_2}} \qquad (2.25).$$

$$k_{z_j} = \frac{\omega}{c}\sqrt{\frac{\varepsilon_j^2}{\varepsilon_1+\varepsilon_2}}, \quad j = 1, 2. \qquad (2.26).$$

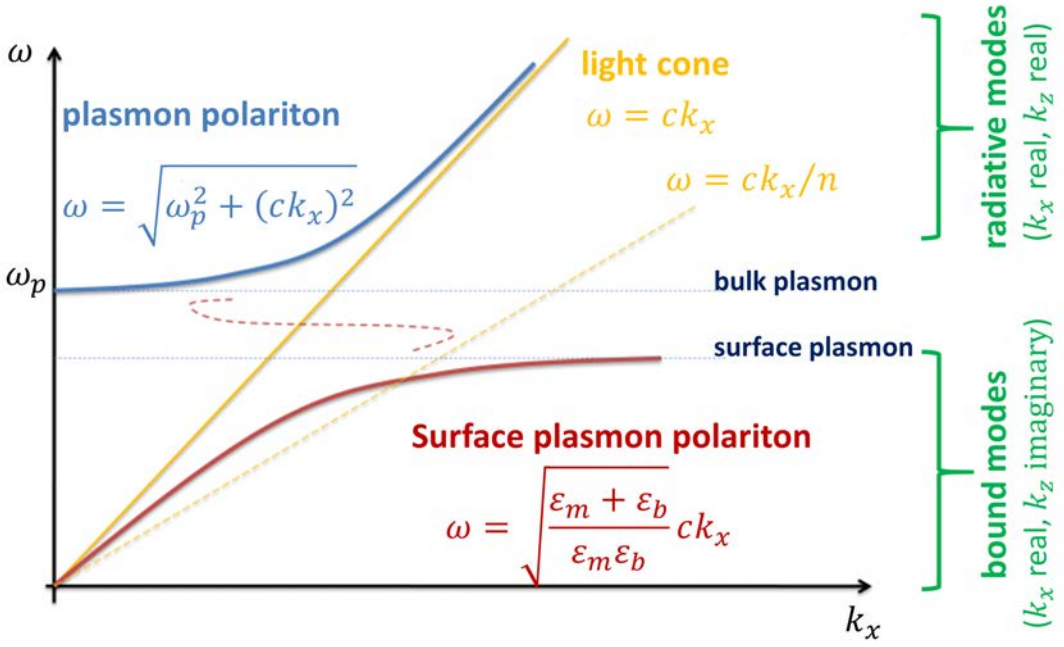

Figure 2.3 Plasmon dispersion relation for an air/metal interface. Because the plasmon dispersion curve (red line; blue line for free electrons) doesn't have any intersections with the light cone (blue line), it's not possible to activate a surface plasmon at an air/metal interface optically. However, the slop of the light cone curve can be decreased (dotted yellow line) by replacement of the free space medium to a dielectric one[24].

For solutions of waves that are propagating along the interface, a real k_x in above formula is required. This can be available by following the conditions

$$\varepsilon_1\varepsilon_2 < 0, \quad \varepsilon_1 + \varepsilon_2 < 0 \qquad (2.27).$$

which leads to an electromagnetic surface wave bond to the dielectric/metal interface. Accordingly, k_{z_j} becomes imaginary and thus corresponds to exponentially decaying evanescent waves.

As can be seen from Figure 2.3, the dispersion curve of the surface plasmon does not intersect with the light cone at any point. Thus, direct excitation of the surface plasmon polaritons with light is not possible. However, SPPs can be excited provided the momentum mismatch is compensated, which can be done by tilting the light curve $\omega = ck_x$ to ck_x/n in dielectric environment, or by generating evanescent fields near the interface as in the Otto and Kretschmann configurations which have already been introduced in Chapter 1 (Figure 1.2).

2.3.2 Localized surface plasmons of metal nanoparticles

Next, we discuss the localized surface plasmons sustained in a metal nanoparticles and distinguish them from their propagating counterpart on the dielectric/metal interface. When an electromagnetic wave illuminates on a metallic nanoparticle (with dimension much smaller than the wavelength), the electron gas in the metal particle gets polarized (at the surface) and the resultant restoring force forms a plasmonic oscillation. The metal nanoparticle thus acts like an electric dipole and the associated resonance behavior dominates the optical response[133].

In principle, the localized plasmon properties of metal nanostructures can be theoretically predicted by solving Maxwell's equations with specific boundary conditions. However, this analytical solutions are only available for nanostructures with spherical or cylindrical geometry, which are worked out by Gustav Mie for seeking the analytical solutions of the scattering response of a spherical particle[134]. After extracting the electromagnetic fields by

Mie's theory, the extinction cross section (C_{ext}), the scattering cross section (C_{sca}) and the absorption cross section (C_{abs}) and can be directed calculated as follows:

$$C_{\mathrm{ext}} = \frac{2\pi}{k^2}\sum_{n=1}^{\infty}\left((2n+1)Re(|a_n|^2 + |b_n|^2)\right) \quad (2.28).$$

$$C_{\mathrm{sca}} = \frac{2\pi}{k^2}\sum_{n=1}^{\infty}(2n+1)(|a_n|^2 + |b_n|^2) \quad (2.29).$$

$$C_{\mathrm{abs}} = C_{\mathrm{ext}} - C_{\mathrm{sca}} \quad (2.30).$$

in which a_n and b_n are coefficients determined by the boundary conditions. In reality, the infinite summations in equations (2.28) and (2.29) are usually truncated to a specific order, depending on the sphere size.

Based on Mie's theory, similar methods to solve Maxwell's equations have been developed for more complex geometries such as multiple-spheres, spherical core-shell structures and cylindrical rods of infinite length[135]. For non-spherical particle, the boundary conditions are too complex to be incorporated into the Maxwell's equations and the analytical solutions are almost impossible. Therefore, some approximations have to be introduced to simplify the calculations. Indeed, when the particle size is much smaller compared to the wavelength of illumination light, the quasi-static approximation can be applied to derive the optical response of particles[25]. Under this approximation, the phase of the light field is assumed to be constant across the entire particle, for which the practical spatial field distribution can be simplified to a case of a particle immersed in an electrostatic field. Thus, the small particles can be regarded as dipoles and the corresponding scattering and absorption can be analytically evaluated. For a small spherical particle, its dipole moment or polarizability, scattering and absorption cross sections can be expressed as:

$$\alpha = 4\pi a^3 \frac{\varepsilon_{\mathrm{p}} - \varepsilon_{\mathrm{m}}}{\varepsilon_{\mathrm{p}} + 2\varepsilon_{\mathrm{m}}} \quad (2.31).$$

$$C_{\mathrm{sca}} = \frac{k^4}{6\pi}|\alpha|^2 = \frac{8}{3}\pi k^4 a^6 \left|\frac{\varepsilon_{\mathrm{p}}-\varepsilon_{\mathrm{m}}}{\varepsilon_{\mathrm{p}}+2\varepsilon_{\mathrm{m}}}\right|^2 \quad (2.32).$$

$$C_{\mathrm{abs}} = kIm(\alpha) = 4\pi k a^3 \mathrm{Im}\left(\frac{\varepsilon_{\mathrm{p}}-\varepsilon_{\mathrm{m}}}{\varepsilon_{\mathrm{p}}+2\varepsilon_{\mathrm{m}}}\right) \quad (2.33).$$

where the ε_{p} and ε_{m} are the dielectric constants of the particle and the surrounding medium. Compared to expressions (2.28) and (2.29), it can be found the results in formula (2.32) and (2.33) are the first-order approximations of the Mie theory. In other words, the optical response of small nanoparticle is determined by the dipole term of the summation in formula (2.28) and (2.29). In light of this insight into the electrostatic approximation, Gans has expanded the Mie model into the case of elliptical particles and worked out the analytical expressions for dipole moment, scattering and absorption cross section of an elliptical particle as:

$$\alpha_j = 4\pi abc \frac{\varepsilon_{\mathrm{p}}-\varepsilon_{\mathrm{m}}}{3\varepsilon_{\mathrm{m}}+3L_j(\varepsilon_{\mathrm{p}}-\varepsilon_{\mathrm{m}})}, \quad (j = x, y, z) \quad (2.34).$$

$$C_{\mathrm{sca},j} = \frac{k^4}{6\pi}\left|\alpha_j\right|^2 \quad (2.35).$$

$$C_{\mathrm{abs},j} = k\mathrm{Im}(\alpha_j) \quad (2.36).$$

here a, b and c are the semi-axes of the ellipsoid. The depolarization factor L_j can be calculated according to

$$L_j = \frac{abc}{2}\int_0^\infty \frac{dq}{\left(a_j^2+q\right)\sqrt{(q+a^2)(q+b^2)(q+c^2)}}, \quad \left(j = x, y, z\,; a_j = a, b, c\right) \quad (2.37).$$

According to equation (2.34), the polarizability α obtains a resonance enhancement under the condition that $\left|\varepsilon_{m+}L_j\left(\varepsilon_p - \varepsilon_m\right)\right|$ reaches its minimum, which, for slowly varying $Im(\varepsilon_p)$ around the resonance, simplifies to

$$Re\left(\varepsilon_{\mathrm{p}}\right) = \frac{1-L_j}{L_j}\varepsilon_{\mathrm{m}} \quad (2.38).$$

This relation is known as Fröhlich condition and defines an oscillation mode corresponding to the dipolar LSP resonance of a metal nanoparticle. Particularly for spherical particles, Equation (2.39) turns out to be

$$Re(\varepsilon_p) = -2\varepsilon_{\mathrm{m}} \tag{2.39}$$

To summarize, the polarizability α of a small metal nanoparticle (spherical or elliptical) solely determines its optical response under quasi-static approximation by

$$\alpha = (1+\kappa)\varepsilon_0 V \frac{\varepsilon_{\mathrm{p}}-\varepsilon_{\mathrm{m}}}{\varepsilon_{\mathrm{p}}+\kappa\varepsilon_{\mathrm{m}}} \tag{2.40}$$

where V is volume and κ is the geometric factor that incorporates the shape dependence of the polarizability α . The localized surface plasmon resonance of the small metal nanoparticle occurs when the polarizability α reaches its maximum at frequency ω_{sp} determined by

$$Re\left(\varepsilon_{\mathrm{p}}(\omega_{\mathrm{sp}})\right) = -\kappa\varepsilon_{\mathrm{m}} \tag{2.41}$$

When the dielectric function of the Drude model is adopted, the frequency ω_{sp} of localized surface plasmon (LSPR) metal nanoparticle can then be calculated

$$\omega_{\mathrm{sp}} = \sqrt{\frac{{\omega_{\mathrm{p}}}^2}{\varepsilon_\infty+\kappa\varepsilon_{\mathrm{m}}} + \gamma^2} \approx \sqrt{\frac{{\omega_{\mathrm{p}}}^2}{\varepsilon_\infty+\kappa\varepsilon_{\mathrm{m}}}} \quad (\gamma \ll \omega_{\mathrm{sp}}) \tag{2.42}$$

With equation (2.41) we can see that, while the real part of the dielectric function determines the spectral position of the LSPR of the metal nanoparticles, the imaginary part determined damping (or dephasing) of the electron oscillations governs the resonance linewidth and absorptive dissipation[136].

2.4 Plasmon coupling in complex metal nanostructures

When two metal nanoparticles are brought in close proximity, the individual surface plasmons sustained in the two particles have capacitive interaction to form new types of

collective plasmon modes[42,44,137–139]. With self-assembling and lithographic pattern technologies, more complex plasmonic nanostructures can be fabricated, such as the trimers[31], heptamers[140], and oligomers[30,141], etc. These coupled nanostructures possess distinctive optical responses and are usually featured with a large electric field enhancement in the gap regions forming the so-called "hot spots"[136,142], which are responsible for a host of plasmon-enhanced spectroscopy applications[143–145]. In analogy with the atomic interactions between constitutive atoms in a molecule, the coupled nanoparticles can be treated as artificial "plasmonic molecules" for which their optical responses can readily be understood by the plasmon hybridization between the individual surface plasmons of the constitutive particles[42].

To permit a solution of the related equations in the hybridization model, several assumptions are required to be made: the electron gas in the metal behaves like liquid and is simultaneously irrotational and incompressible (uniform charge density), (2) the positive ions background are both homogeneous and stationary, (3) the individual particle plasmons can be described with a separable curvilinear coordinate system, and (4) the quasi-static approximation is effective for the individual particle elements, which means the electric retardation effect can be effected and the instantaneous Coulomb interactions between the elementary particles dominate the total optical responses[146]. Given these requirements are satisfied, the exact solutions to hybridization can be attainable.

In addition to offering quantitative solutions, the plasmon hybridization model allows an intuitive understanding of the plasmonic response of complex coupled nanoparticles. Taking the nanosphere homodimer for example, each of the constitute particles supports a primitive plasmon of resonant frequency

$$\omega_{\mathrm{mono}} = \omega_{\mathrm{p}}\sqrt{\frac{l}{2l+1}} \qquad (2.43).$$

where ω_p is the bulk plasma of the metal, l is the angular momentum indexing the spherical harmonics of different order, i.e., the dipole ($l = 1$), quadrupole ($l = 2$), and higher order plasmon modes (as indicated in Figure 2.4). When the two particles are getting closer, the coupling between the primitive plasmon in each sphere leads to a symmetric splitting of the plasmon resonances by forming the bonding and antibonding modes. Since the higher frequency antibonding mode has no dipole momentum, it cannot directly interact with the incident light, rendering it "dark" in the far field. In contrast, the bonding dipole mode, corresponding a strengthened dipole momentum, is optically active and is also known as a "bright" mode. As the interparticle gap distance decreases, interactions with the higher order modes become significant and can contribute an additional spectral redshift to the hybridized modes. The dark higher order modes can turn to optically active by coupling to the dipolar particle mode through modes hybridization, thus manifesting themselves in the far-field optical responses[147]. In the case where the primitive plasmons of the same order possess orthogonal modes, such as the degenerated primitive plasmons of a spherical particle, the interaction between the higher order modes and the dipole plasmons are forbidden and thus hinders the direct optical activation of the dark modes.

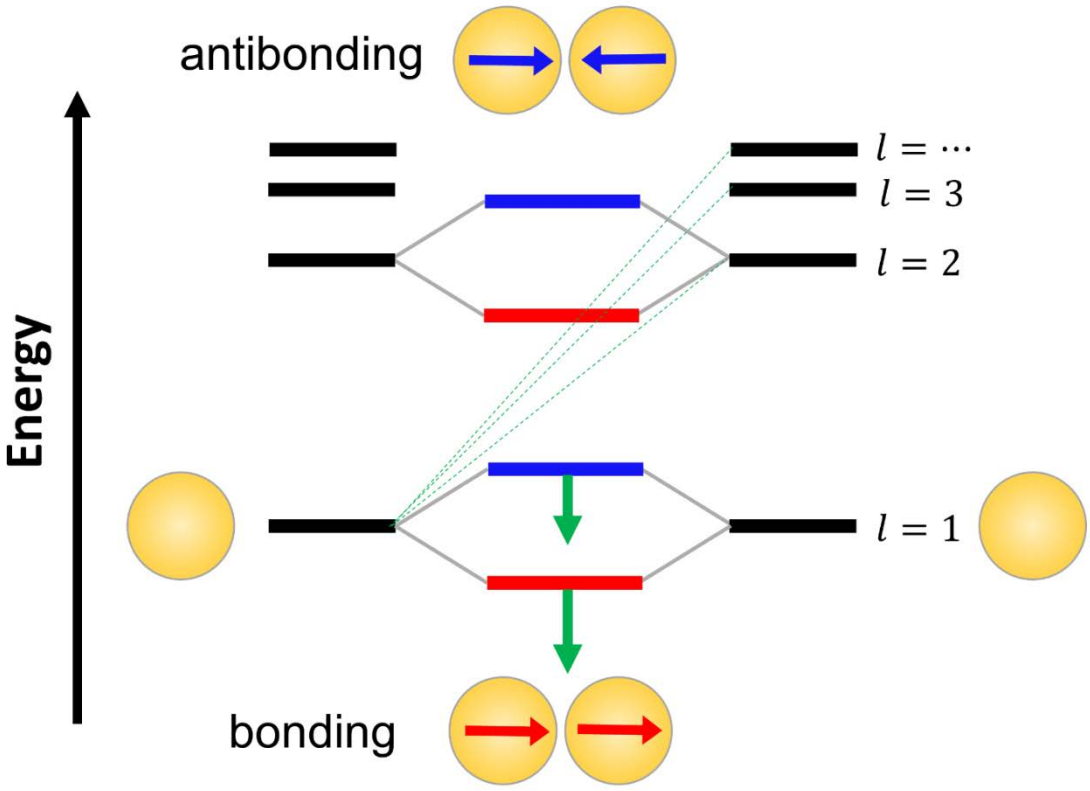

Figure 2.4 Schematic of the plasmon hybridization in a metal nanoparticle dimer. The individual particle plasmons on the two nanoparticles interact and form bonding and antibonding plasmons mode. The arrow in each nanosphere (red and blue) indicates the individual dipole moment. In the dimer, the plasmons of an individual particle can interact with the non-orthogonal ones of the adjacent particle with different angular momentum (indicated by the dashed lines), which leads to an additional shift of the hybridized modes (depicted by the green arrows for the hybridized plasmons with $l = 1$).

As illustrated by the dimer system, plasmon hybridization model provides a design principle for engineering the optical response of complex nanostructures. More specifically, not only the interaction strengths can be geometrically tuned, but also the hybridized mode energy can be manipulated in a wide spectral band through control over the interparticle gap. In addition, for coupling systems with different constitute particles, the hybridization strength is also relevant to the energy gap between the separated primitive plasmons. Anyway, the

strongest hybridization occurs when the primitive plasmon modes are matched both spatially and spectrally. An analytical treatment of the coupled plasmonic system is usually prohibitive, the application of the plasmon hybridization model thus enable an intuitive physical understanding of the numerical results from full wave electromagnetic simulations.

Additional simplified treatments for descriptions of the plasmon coupling include: (1) the coupled dipoles model, in which the individual particle is treated as an electric dipole within electrostatic approximation; (2) the coupled harmonic oscillator model. In this theory, the two nanoparticles in a dimer can be viewed as two oscillators with frequencies ω_1 and ω_2, respectively. The two oscillators couple with each other through a spring connecting them. The response of this equivalent system can be rigorously derived with Lagrange or Hamiltonian mechanics; (3) the resonant L-C circuit model. In this model, a simplified L-C oscillation circuit constituted with one inductor and one capacitor is introduced to model the coupled particles pair, and the inductance and the capacitance are determined by the dielectric gap distance between the constitute nanoparticles. Interested readers can find more details in related literatures[138,148–151].

In general, a thorough evaluation of the plasmonic response of the irregular nanoparticles and complex nanostructures is fully included in the solutions of Maxwell's equations, which in practice can only resort to the full-wave electromagnetic simulations. In the numerical methods, Maxwell's equations are either discretized in the time domain finite difference (FDTD) configuration, or are transformed into the integral form in the finite elements method (FEM). In this thesis, both of these two methods will be adopted in the chapter (4-7) and some details on the simulations configurations can be addressed in the appendix part.

2.5 Second harmonic generations in the metal nanostructures

2.5.1 General description of the nonlinear optical response of materials

As for the nonlinear optical response of materials, let's reproduce the nonlinear polarization expressions of equations (2.12b) below for further discussions. The nonlinear polarization per unit volume in the material can be written as

$$P_\alpha^{(\mathrm{NL})}(r,t) = \sum_{\beta\gamma} \chi_{\alpha\beta\gamma}^{(2)} E_\beta E_\gamma + \sum_{\beta\gamma\delta} \chi_{\alpha\beta\gamma\delta}^{(3)} E_\beta E_\gamma E_\delta + \cdots,\ \alpha,\beta,\gamma \in \{x,y,z\} \tag{2.44}$$

With dyadic notations, the above expression can be simplified as

$$P_\alpha^{(\mathrm{NL})} = \chi_\alpha^{(2)} E{:}E + \chi_\alpha^{(3)} E{:}E{:}E + \cdots, \tag{2.45}$$

where

$$\chi_\alpha^{(2)} = \begin{bmatrix} \chi_{\alpha,\alpha\alpha} & \chi_{\alpha,\alpha\beta} & \chi_{\alpha,\alpha\gamma} \\ \chi_{\alpha,\beta\alpha} & \chi_{\alpha,\beta\beta} & \chi_{\alpha,\beta\gamma} \\ \chi_{\alpha,\gamma\alpha} & \chi_{\alpha,\beta\gamma} & \chi_{\alpha,\gamma\gamma} \end{bmatrix} \quad \chi_\alpha^{(3)} = \cdots \tag{2.46}$$

$$EE = \begin{bmatrix} E_\alpha E_\alpha & E_\beta E_\alpha & E_\gamma E_\alpha \\ E_\alpha E_\beta & E_\beta E_\beta & E_\gamma E_\beta \\ E_\alpha E_\gamma & E_\beta E_\gamma & E_\gamma E_\gamma \end{bmatrix} \quad EEE = \cdots \tag{2.47}$$

the $\chi_\alpha^{(2)}$ and $\chi_\alpha^{(3)}$ are the second- and third-order nonlinear susceptibility tensors. The EE and EEE correspond to the second- and third-order electric dyad tensors. Therefore, the second-order nonlinear optical response of the materials can be fully described by the 27 elements in tensors of $\chi_\alpha^{(2)}$. The governing equation is given by the following SHG polarization[152]

$$P_\alpha^{(2\omega)} = \epsilon_0 \sum_{\beta\gamma} \chi_{\alpha\beta\gamma}^{(2)} E_\beta^{(\omega)} E_\gamma^{(\omega)} \tag{2.48}$$

Then we can calculate the corresponding nonlinear current as[108]

$$j^{2\omega} = \frac{\partial P}{\partial t} = -i2\omega P^{2\omega} \tag{2.49}$$

With the nonlinear current source, the near-field and far-field properties at the second harmonic frequency can totally be calculated.

2.5.2 SHG in plasmonic nanostructures

Surface plasmons are commonly associated with noble metals (Au, Ag) possessing a centrosymmetric lattice structure. Within the electric dipole approximation, the dipolar SHG from the metal bulk vanishes[5]. The origin of the nonlinear optical response can be attributed to the breakdown of the centrosymmetry at metal surface (termed as local response) or field gradients inside the bulk metal (nonlocal response). The total second harmonic polarization can be written as a sum of the surface and bulk contributions,

$$P^{(2\omega)} = P_{\text{surf}}^{(2\omega)} + P_{\text{bulk}}^{(2\omega)} \tag{2.50}.$$

$$P_{\text{surf}}^{(2\omega)} = \varepsilon_0 \chi_s E^{(\omega)} E^{(\omega)} \delta(r - r_s) \equiv P_s^{(2\omega)} \tag{2.51}.$$

$$P_{\text{bulk}}^{(2\omega)} = \varepsilon_0 \chi_b E^{(\omega)} E^{(\omega)} \tag{2.52}.$$

where r_s defines the metal surface and χ_s and χ_b represent the second-order susceptibility tensors. If the surface is of isotropic symmetry with an image plane perpendicular to it, the χ_s has only three non-vanishing elements: $\chi_{\perp\perp\perp}^{(2)}$, $\chi_{\perp\parallel\parallel}^{(2)}$ and $\chi_{\parallel\perp\parallel}^{(2)} = \chi_{\parallel\parallel\perp}^{(2)}$, where the symbol $\perp$ (or $\parallel$) denotes the direction normal (or parallel) to the surface[153]. Therefore, the surface polarization can be recast to

$$P_s^{(2\omega)} = \vec{n}\left(\chi_{\perp\perp\perp}^{(2)} E_n^{(\omega)} E_n^{(\omega)} + \chi_{\perp\parallel\parallel}^{(2)} E_t^{(\omega)} E_t^{(\omega)}\right) + 2\vec{t}\chi_{\parallel\perp\parallel}^{(2)} E_n^{(\omega)} E_t^{(\omega)} \tag{2.53}.$$

where $E_n^{(\omega)}$ and $E_t^{(\omega)}$ are the normal and tangential field components near the interface. The bulk polarization arises from the spatial field gradients inside the material and can be expressed as

$$P_{\text{bulk}}^{(2\omega)} = \beta E^{(\omega)} \nabla \cdot E^{(\omega)} + \gamma \nabla \left(E^{(\omega)} \cdot E^{(\omega)} \right) + \delta' \left(E^{(\omega)} \cdot \nabla \right) E^{(\omega)} \quad (2.54).$$

Where β,γ and δ' are the intrinsic parameters of material[153,154]. In the isotropic media, the first term vanishes. Generally, the susceptibility component $\chi_{\perp\perp\perp}^{(2)}$ dominates the contribution to the surface SH response in metal nanostructures[108,155], and the typical value is of order $\sim 10^{-18} m^2 V^{-1}$[156]. Aside from experimental retrieval of nonlinear susceptibilities, analytical evaluation of parameters which offer deeper insight on the origin of complex nonlinearity in metals can be achieved with free-electron gas, hydrodynamic and quantum density functional theories[157–159]. A more involved self-consistent and non-perturbative approach for describing harmonic generation in metal nanostructures was recently developed within the hydrodynamic model[160,161]. In this thesis, as will be seen in chapter 7, a simplified version of this model is implemented in the finite element method and help to shed light on the second harmonic generation in the metal film-coupled nanoparticles.

Chapter 3 Sample fabrication and characterization techniques

The samples used in this thesis work are the metal film-coupled nanoparticle structure. In this chapter, I will firstly present some details on the sample fabrication. Then I will introduce the primary instrumental techniques to characterize the sample morphology. At last, I will show the specific optical systems involved in this thesis for the dark field, photoluminescence and nonlinear optical spectroscopy in single nanoparticles level.

3.1 Sample fabrication

The schematic illustration of the metal film-coupled nanoparticles is depicted in Figure 3.1, in which the nanoparticle is gold The separation between the nanoparticles and the planar gold film is achieved by the coating cetyltrimethylammonium bromide (CTAB) molecule layer which enables a gap distance $\sim 0.5 - 1nm$ at the junction[162].

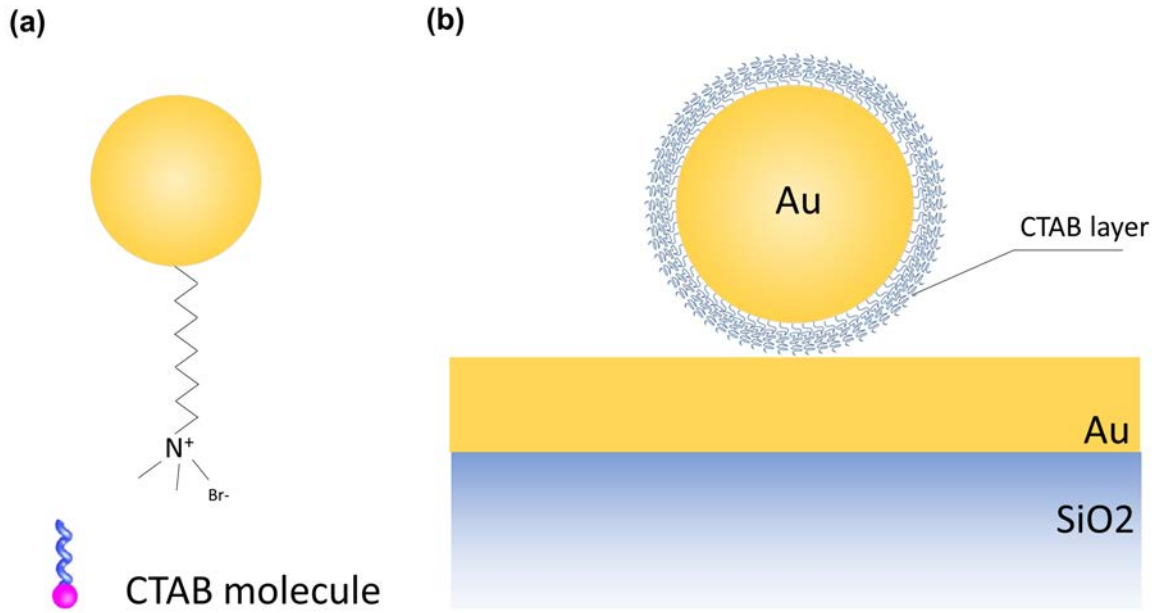

Figure 3.1 Schematic illustration of the metal film-coupled nanoparticles. Cetyltrimethylammonium bromide molecules are used as the surfactants for stabilization in solution (a) and simultaneously can be used as a dielectric spacer to separate the particle from the gold film (b).

3.1.1 Au film deposition

In the first step, the gold film is deposited on an ultraclean silica coverslip (Schott Nexterion, Germany) with a thermal evaporator (Nexdep, Angstrom Engineering, Inc.). The mechanics of the deposition process are schematically presented in Figure 3.2a. Upon electrically heating at high temperature in vacuum ambience, the bulk gold (24k) in the source container will be melt and vaporized into gas of gold atoms which continuously strike the silica surface hanging above and will gradually accumulate forming gold atom layer. The two important parameters, thickness of the film and roughness of the metal surface for loading nanoparticles are carefully controlled in the deposition process. The film thickness can be tuned by controlling the total amount of the deposition source (bulk Au) and the exposure

time of the silica surface to the source, while he roughness of the formed film is directly correlated with the vacuum level and the deposition rate.

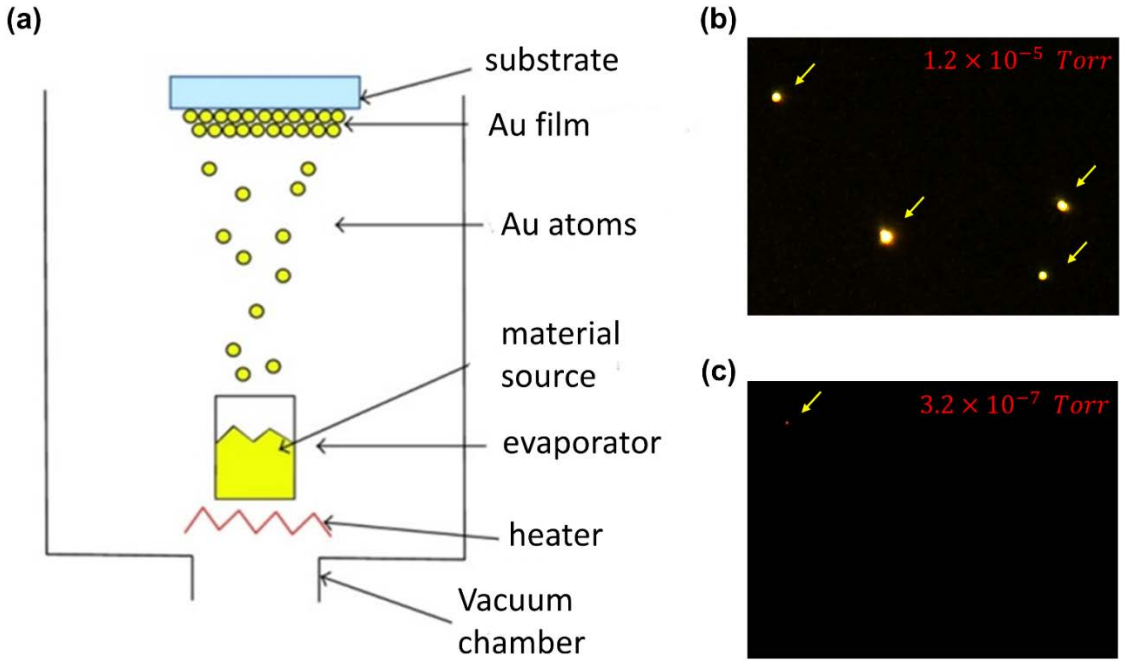

Figure 3.2 (a) Schematic of the thermal evaporation process for metal film deposition. (b) A simple quality evaluation of the gold film deposited under different vacuum level. The images are captured under a dark field microscope with 100× magnification and each image corresponds to a check area of $120\times100\mu m^2$.The particles indicated by the yellow arrows refer to the contaminants introduced during the deposition process. As seen from (c), the image comes with a pure back background and considerably reduced dust numbers, corresponding to a high-quality gold film with small root-mean-square (RMS) of the surface roughness.

In the practical deposition process, the film thickness of optically oblique can always and readily be guaranteed. Usually, the thickness of the film obtained is around $50nm$ when $\sim500mg$ bulk gold is loaded in the source container and the pumping electrical power is set to be 27% of its available power maxima (corresponding to an average deposition rate of $1.8\,Å/s$). The configuration for smaller roughness, however, is highly demanded and especially dependent on the vacuum level that can be achieved. It has been demonstrated by

the comparison presented in Figure 3.2(b) that, at high vacuum level (up to $3.2\times10^{-7}\ Torr$), the roughness of the metal surface is significantly improved compared to that of the lower vacuum level ($\sim1.22\times10^{-5}\ Torr$). Therefore, in each batch of metal film deposition, the deposition chamber is pumped to an extreme high vacuum level of the order $10^{-7}\ Torr$ for high quality metal film yet at a cost of long vacuum pumping time ($8-10\ hours$, typically). As showed in Figure 3.3a, the measured roughness (evaluated by RMS sort for root-mean-squared) of the metal surface by atomic force microscope (AFM) is $\sim0.75\ nm$.

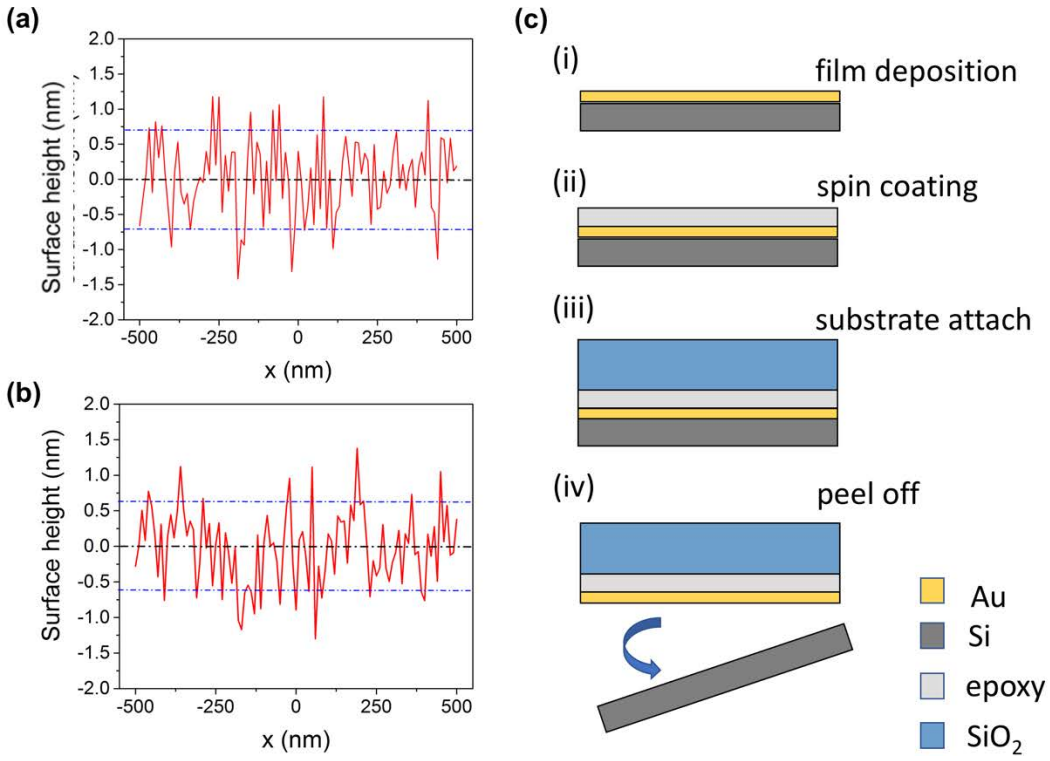

Figure 3.3 (a-b) The measured roughness of the gold film surface with AFM mapping. The vacuum pressure of the deposition chamber is about $1\times10^{-7}\ Torr$. The upper plotting corresponds to metal film fabricated with ordinary thermal evaporation method while the bottom one presents surface roughness of the gold film peered off from the silicon surface. (c) schematic of the pear-off method used to fabricate gold film with smaller roughness.

Chatdanai Lumdee's work[60] has demonstrated the effect of the nanoscale metal surface roughness on the far-field spectral response, which indicates a plasmon resonance induced by

the nanoscale environmental perturbations near the gap junctions. This influence can be more pronounced in various plasmon-enhanced nonlinear optical measurements due to their high sensitivity to field variations. Accordingly, the peel-off method[163] has been adopted for further improving the metal surface RMS, In this deposition flow, as depicted in Figure 3.3b, the gold film is initially deposited on the crystal silicon surface with the thermal evaporation method. Then it will be transferred to the glass substrate with optical epoxy (MG Chemicals, 8322-1), and therefore, the previous metal surface at the silicon-gold interface will be left exposed for following loading of nanoparticles. Since the silicon surface comes with an ultra-flat surface determined by the mono-crystal surface structure, the roughness of the facing surface of the attached gold film can be readily controlled within the angstrom scale ($\sim 0.5\ nm$) as indicated by the AFM measurements in Figure 3.3b.

3.1.2 Au nanoparticles

The gold nanoparticles used here are mainly nanospheres purchased as the form of colloidal solutions (NanoSeedz Ltd., Hong Kong) with OD=5.0 for each batch of them. To avoid the clustering of particles and stable dispersion in the solution, the nanoparticles are all coated with a mono-layered Cetyltrimethylammonium Bromide molecules which are positively charged as already depicted in Figure 3.1. Before dispersed on the gold or silica substrates, the colloidal solutions will be centrifuged for 15 minutes at the speed of 5000 rpm to remove the excessive CTAB molecules in the host solvent, and then diluted with deionized water to the concentration level one third of its originals.

For constructing of the particle on film configuration, a drop of diluted colloidal solution ($\sim 100\ \mu L$) is casted on the gold film or glass substrate and left dry in air for a few seconds.

Particularly, during the drying process, some nanospheres are likely to self-assemble into dimers, trimers or even more complex clusters.

3.2 characterization techniques

3.2.1 Ultraviolet-Visible Spectrophotometer

To have preliminary understandings of the optical properties of the gold nanoparticles, measurements of the extinction spectra are performed by the Ultraviolet-Visible Spectrophotometer (UV-2550 UV-Vis., Shimadzu). The extinction cross section (σ_{ext}), defined by the sum of scattering (σ_{sca}) and absorption (σ_{abs}) cross sections of the particles, are usually used to evaluate the interaction intensity between the light and matters. Actually, in experiments the measurable quantities related to the extinction of colloidal solutions are the transmittances. By measuring the different light intensity of a light beam before and after passing through a standard $1cm$-quartz-cuvettes containing the diluted particles solution, the extinctions of the ensemble nanoparticles can be evaluated by

$$\sigma_{\text{ext}} \propto -log_{10}(T) = -log_{10}\left(\frac{I_0}{I}\right) \tag{3.1}$$

where I_0 and I are the optical power of the incident and transmitted lights, respectively. The typical extinction spectra measured within the range $450 - 950nm$ is presented in Figure 3.4(b). As can be seen, with, the light with wavelengths at around 550nm are significantly extinct after passing through the nanoparticles solution, which implies a strong light-nanoparticles interaction at these wavelengths.

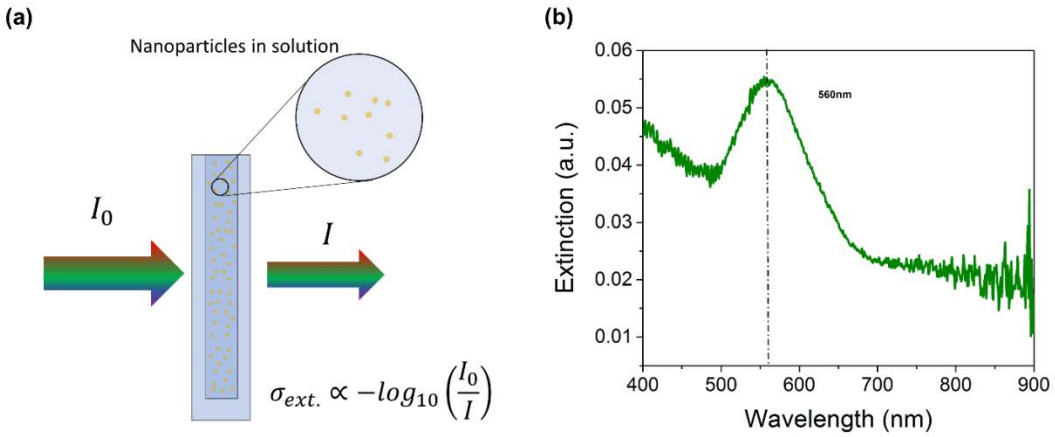

Figure 3.4 (a) Schematics of the extinction measurements of the nanoparticles solution. (b)The measured extinction spectrum of the 100nm gold nanoparticles dispersed in water.

3.2.2 Optical dark field microscopy

Nowadays, the dark field microscopes are almost indispensable characterization tools in studying the optical properties of plasmonic nanostructures. Thanks to their significant enhancement in imaging contrast or signal-to-noise ratio (SNR), weakly emitting tiny objects (even a few tens nanometer) can readily be identified from the noisy imaging background by this observation mode. The mechanics of the high SNR in this microscopy technique can easily be understood by the common sense that the tiny dusts floating in the air ambience can readily been observed in a light beam entering a dark room from inside the room as depicted in Figure 3.5(a). The key point is that the observation direction of our naked eyes must have large angle with respect to the light beam, so that only the scattered light by the tiny dusts can enter our eyes forming the observation view. Since the strong transmitted light rays on the tiny dusts won't enter the eyes, a high contrast can be achieved and the tiny dusts are enabled to stand out from the background. The dark field microscopes share the same function principle with that of the visibility of tiny dusts in air. There are two types of setup configurations for

constructing the optical dark field microscopes- the transmitted and reflected modes, which are depicted in Figure 3.5(b). In the transmitted configuration, the inserted oblique disk in the incidence beam blocks light from the central part of the beam and allows only the outer light ring enter the condenser lens. After focused by the condenser, a hollow light cone is formed as the illumination field. The half angle of the cone θ is determined by the numerical aperture (NA) of the dark field condenser (including the oblique disk) as the function of $\theta = arcsin(\mathrm{NA})$. To achieve a dark background in the observation view formed through the collection objective, the NA of this objective must be at least smaller than that of the bottom condenser to avoid collecting the strong light in the directly transmitted direction. As shown, only the light scattered by the tiny particles can generate rays falling within the collection angle of the objective to form the image. To be noted that this configuration enables the collection of the forward scattering for imaging light and works only for the transparent substrate case. When the substrate is oblique, like the optically thick metal films in our study, the configuration choice should be the reflected dark field illumination. In this configuration, the specially designed objective is functioned as both a condenser and imaging lens. The hollow light cone is achieved by the lens tube consisting of a hollow circular mirror and dark field objective. This elaborate design makes the collected scattering rays in the central part of the tube well separated from the direct incidence for illumination, enabling a pure black background for high contrast observation.

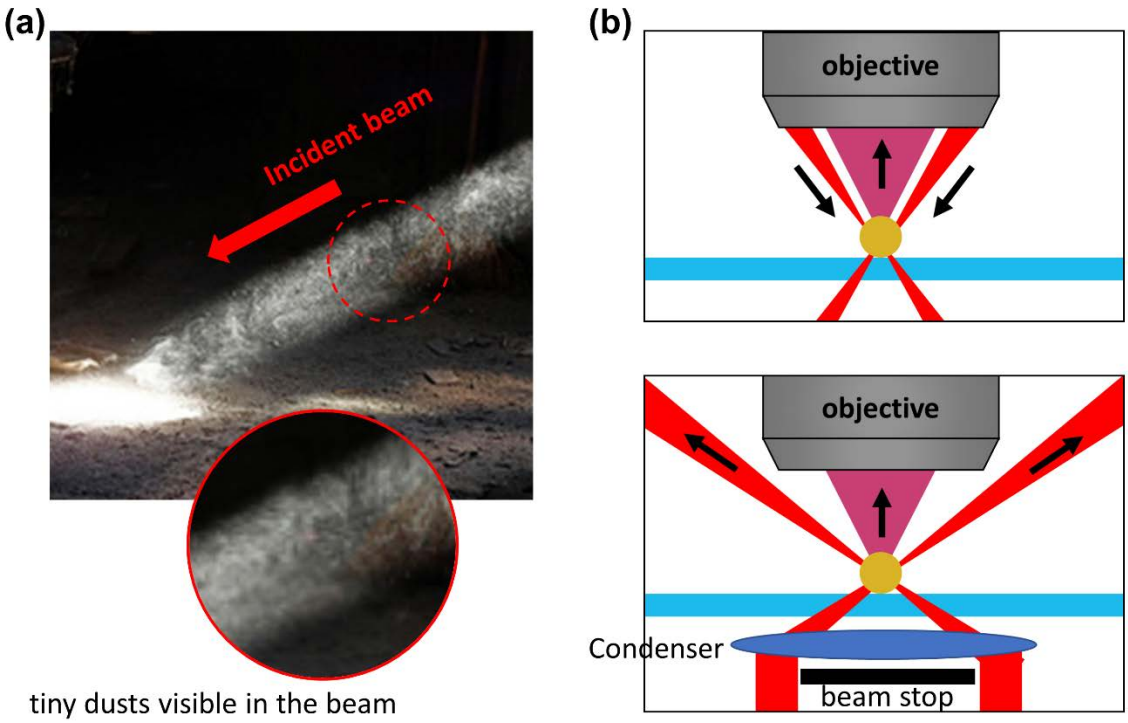

Figure 3.5 (a) An example illustrating the working principle of dark field imaging. The dusts in the incident can be clearly visible in the scattering directions, whereas are invisible in the transmission (or incident) direction. (b)The schematics of the key parts of two types of dark filed microscopes. The upper panel corresponds to the one of reflection mode, in which the back-scattered light is collected for imaging while the objective in the transmission configuration (bottom) collects the forward-scattered light with illumination from the bottom side.

In our experiments, a dark field spectroscopy system has been constructed based on the upright dark field microscope (BX51, Olympus), which enables the optical characterization of the plasmonic nanostructures in the single nanoparticle level. The dark field configuration adopted here is of a reflected mode as in Figure 3.5(b). Being reflected by the hollow circular mirror, light from the light source is steered into the outer tube shell of the objective and then focused to form the hollow light cone for illuminating

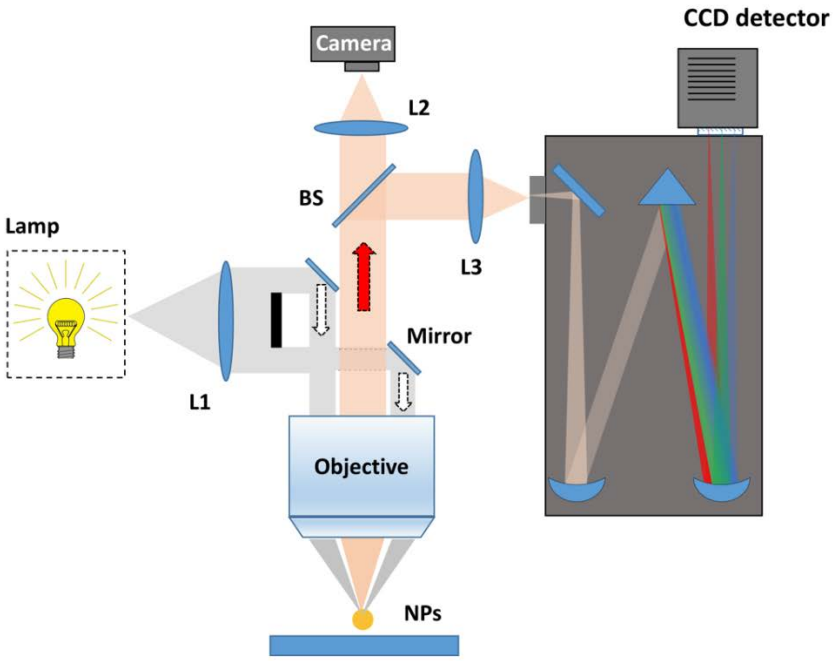

Figure 3.6 Experimental setup for the dark field spectroscopy over single nanoparticle.

the nanoparticles. While the mirror-reflected light from the substrate will mostly return to the incidence path, the scattered light from the nanoparticles will be collected and guided to the eyepiece or the camera for imaging or spectral analysis by the spectrometer system. A typical dark field image of the nanoparticles is presented in Figure 3.7(a), shot by a true-color CCD camera (QICAM 12 bit, QImaging Inc.) mounted on the optical output port.

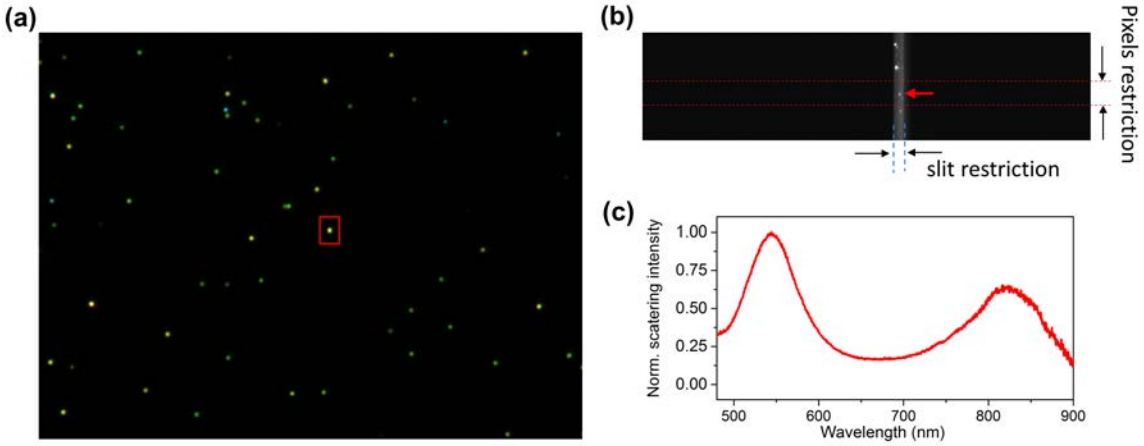

Figure 3.7 Measurement of scattering signals from single nanoparticle. (a) The dark field image of gold nanoparticles dispersed on gold film. The imaging size is $120\mu m \times 100\mu m$. (b) Isolating the scattering signal to the single particle level, the narrowed slit width and selected pixel rows together define a small area containing only one particle and only signals from this area can be acquired by the detection device. (c)The typical scattering spectrum of single gold nanoparticles ($100\mu m$) on gold film.

For measuring the scattering spectrum of single nanoparticles, a confocal imaging configuration is performed in the detection path as depicted in Figure 3.7(b). The basic thinking is to restrict the detection area in the sample into a micro-sized area containing just one nanoparticle as indicated by the rectangular box in Figure 3.7(a). Since the real imaging planes are located at the spectrometer entrance and the camera sensor, the isolating of signal from single nanoparticles can be achieved by horizontally narrowing the slit width at the entrance of the spectrometer, and simultaneously extracting only the signals from the pixel rows (vertically restriction) corresponding to the height of the targeted particles. Upon completing the isolation of single nanoparticle in the imaging plane, only the light from this particle can get accessed to the signal detection channel. Then the optical system is switched to the spectra mode so that the CCD detector can record the intensities of grating dispersed light and output the scattering spectrum of single nanoparticles. A typical scattering spectrum for a $100nm$ gold nanoparticle deposited on gold film is showed in Figure 3.7(c).

3.2.3 Scanning Electron Microscopy

Scanning electron microscopy (SEM) is used to characterize the geometric morphologies of structures with the size below the optical diffraction limit. According to the Rayleigh Criterion, the resolution δ of an optical microscope is determined by $\delta = 0.61\lambda/NA$,where λ is the illumination wavelength and NA is the numerical aperture of the objective. With the

achievable value of NA (typically, ≤ 1.4), the theoretically limited resolution is of the same scale order of the wavelength. The resolution of a conventional optical microscope is hundreds of nanometers which makes it incapable to resolve the structure details within the sub-nanometer scale. The wavelength of electrons in motion, defined as $\lambda = h/p$, can be manipulated by controlling the momentum p. Being accelerated by the moderate electric potential, say, $100\,keV$, the corresponding wavelength of the electron can reach $3.7\times 10^{-3}\,nm$, which is far lower than that of the visible light. Therefore, this ultra-short electron wavelength in the SEM system leads to a much higher resolution (down to several nanometers) compared to the conventional optical microscope.

3.2.4 Photoluminescence spectroscopy

Photoluminescence measurements of plasmonic nanostructures in the single particles are performed based on a modified micro-Raman confocal system (LabRAM HR800, Horiba), which is schematically depicted in Figure 3.8. Lasers, with polarization direction controlled by the half wave-plate (HWP) is guided to the microscope and tightly focused on the samples by the objective. Emitted photons will be collected by the same objective and then partially reflected to the spectrometer for spectral analysis after passing through the dichroic mirror (DM). For identifying the single nanostructure, a dark field illumination arm is constructed besides the microscope based on a fiber white light source (Schott, A20510). Scattered light can be collected by the objective and partially enter the camera for imaging.

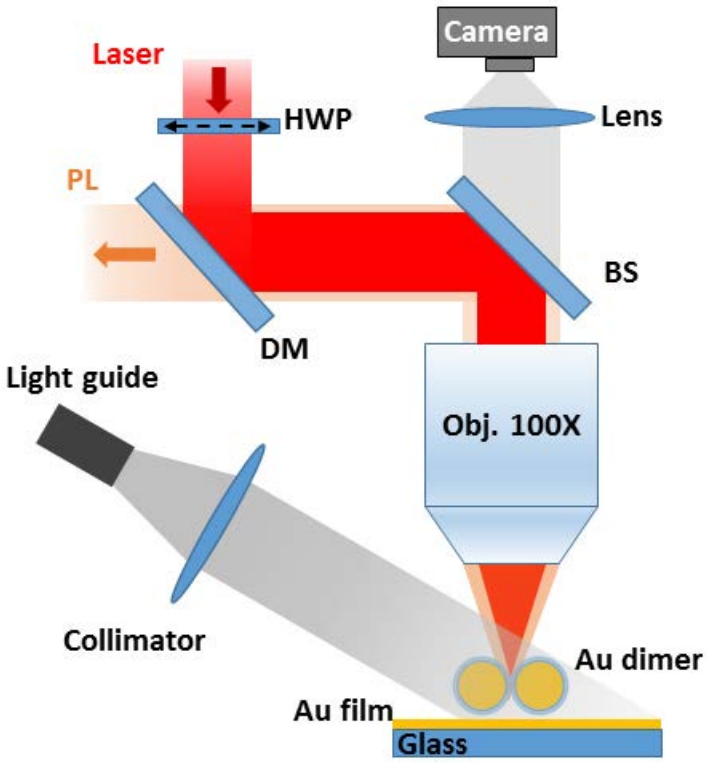

Figure 3.8. Experimental setup of the photoluminescence measurement of individual plasmonic nanostructures. HWP: half wave-plate. DM: dichroic mirror. BS: beam splitter.

3.2.5 Nonlinear optical emission spectroscopy

The measurements of nonlinear optical emission from individual nanostructures were carried out on a functionally extended commercial laser scanning confocal microscope system (TCS SP8, Leica) combined with a Ti:sapphire femtosecond laser (Mai Tai HP, Spectra-Physics). The time duration and repetition rate of the laser pulse is about 200fs and 80MHz, respectively. As depicted in Figure 3.9, the scanning of the laser beam at the focal plane is controlled by the beam scanning resonator with programing applications in PC. Before reaching the sample plane, the laser beam is tightly focused by a dry objective with high NA (0.95). The continuous scanning over the sample by the focused laser beam will result in an emission intensity profile in gray scale and thus scanning images are formed. All the

subsequent analysis, including the emission intensity evaluation, spectra acquisition, are all based on the obtained false color images. Specifically, in the nonlinear optical imaging, the size of pinholes between L1 and L2, which should be carefully optimized in ordinary scanning confocal mode, yet are set as fully open since the nonlinear optical emission occurs just in the very small focus volume and the background intensity are intrinsically suppressed.

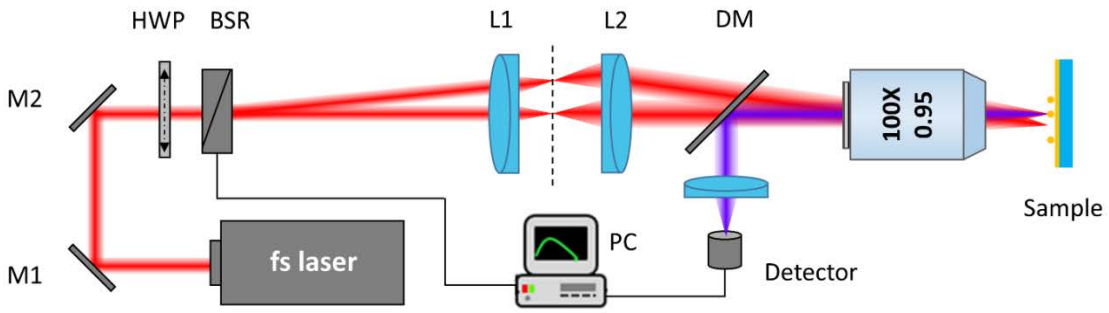

Figure 3.9. Experimental setup of the nonlinear optical spectroscopy. M1 (M2): mirror 1 (mirror 2). HWP: half-wave-plate. BSR: beam scanning resonator. L1 (L2): lens 1 (lens 2). DM: dichroic mirror.

Chapter 4 Unveiling the plasmonic resonances in an Au film coupled nanoparticle by polarization-resolved dark-field spectroscopy

In a close analogy to the strong interaction between a fluorescent molecule and a neighboring metal film, the system of metal film-coupled nanoparticles has recently received a great deal of research interests.[54,60–63,65,164–166] In this system, the presence of the underlying metallic film breaks the rotational symmetry of a spherical nanoparticle, resulting in strong coupling between the plasmon modes supported by the individual nanoparticle with its induced image on the film. As a result, the nanogaps between the particles and the film behave like plasmonic hot spots with extremely large field concentration which promises many plasmon-mediated optical sensing and enhancement applications.[55,167,168] Moreover, this film-coupled nanoparticle system offers a versatile platform for exploring a variety of fundamental nanophotonic phenomena such as spatial nonlocality[66] and quantum tunneling when the gap is less than 0.5 nm.[67] Thus far, most previous investigations have been focused primarily on the system consisting of a single nanoparticle atop a metal film.[169–172] In the monomer-film system, the interaction between the dipolar plasmon mode sustained by the nanoparticle and the underling film, as well as tuning mechanism of the plasmon mode through gap distance controlling are extensively studied. However, little light has been shed on the effect of the underlying metal film on the coupling plasmon modes sustained by complex nanostructures sitting above. Thus, there is very little knowledge about plasmonic properties (resonance position and radiation behavior) of metal film-coupled nanoparticle clusters like dimers or

more complex nanostructures and the potential applications associated with these interesting systems also remain unexplored.[173–175]

In this chapter, I will present an experimental study for the first time on the coupled plasmon resonances in a single metallic film-coupled nanoparticle dimer system. To start this, the scattering responses of both the gold film-coupled nanoparticle monomers and dimers are examined in Section 4.1. It has been found both the monomer and dimer on film support two plasmon resonances at 550nm (i) and 830nm (ii). Particularly, a strong plasmon peak appears at 650nm (iii) in the scattering spectra of nanoparticle dimer. To uncover more physics about these plasmon resonances, excitation polarization dependent scattering measurements are performed in Section 4.2 for individual nanoparticle monomer- and dimer-film nanostructures, respectively. With the polarization resolved spectral decomposition and color decoding base on a functionally extended dark field spectroscopy, we reveal that the plasmon resonance (1) and (2) in both monomers and dimers can be preferentially excited by light with horizontal and vertical polarizations, respectively. Particularly, the excitation polarization along the dimer axis in the film-coupled dimer is highly responsible for the plasmon resonance (3) and the newly emerged one at 530nm (4). Analysis based on the electromagnetic simulations on electric charge and field distributions suggest the dipolar origins of the modes (1) and (2), well consisting with the features of the intensity patterns measured experimentally in the far field. The distortions in charge distributions of mode (3) and (4) in the dimer, however, imply a plasmon hybridization between the bright dipolar mode and high order modes. Finally, in Section 4.3, we demonstrate that the in-plane polarization sensitive gap modes (3) of the gold film-coupled dimer constitute a new nano-metrology tool that can be used to precisely resolve

the spatial orientation of the nanoparticle dimer and also optically distinguish dimers from monomers.

4.1 Optical characterization of gold film-coupled nanoparticles

As mentioned in the last chapter, the diameter of all the nanospheres in our study is ~100 nm. The gap distances are solely determined by the ~1 nm thickness of the coating CTAB layer, which results in the ~1 nm particle-film separation and ~2 nm particle-particle gap distance in the nanoparticles dimer on film. Figure 4.1a depicts a schematic of the gold film-coupled nanospheres and two different dark-field illumination configurations used in our experiment. The left panel shows a built-in un-polarized illumination scheme with a standard dark-field microscope system. Although a polarizer can be inserted in the illumination light path before the objective, the polarization direction of the hollow beam cone cannot be well controlled with respect to the nanostructure orientation in the focal planes, particularly for the nanoparticle dimer. To overcome this limitation, we construct an external illumination arm with which the incidence polarization can be continuously tuned from s- to p-polarized as shown in the right panel of Figure 4.1a. Additionally, the incidence angle can also be tuned within a specific range beyond the cone angle defined by the numerical aperture of the objective. This setup improvement has enabled the polarization- and angle-dependent excitation of specific plasmon resonance modes in complex plasmonic nanostructures, significantly facilitating the understanding of their mode characteristics.

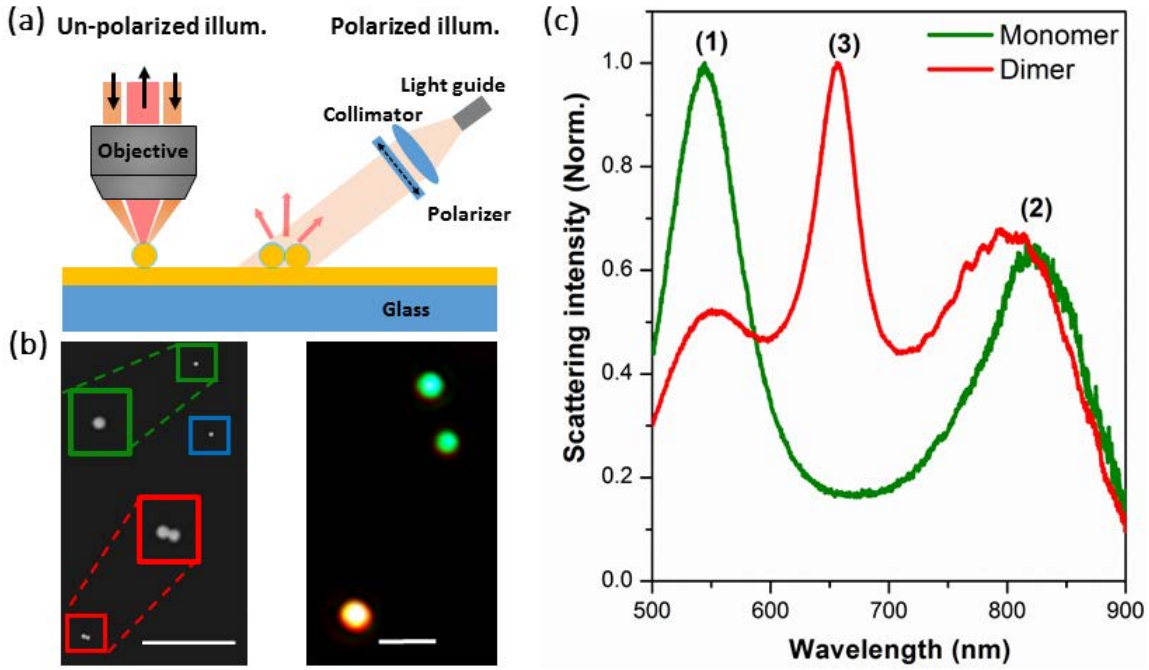

Figure 4.1 (a) Schematic of gold film-coupled nanoparticles under standard (un-polarized, left panel) and home-built (polarization tunable, right panel) excitation configurations. The thin shells in light-blue represent the CTAB coatings around gold nanospheres. (b) SEM micrograph (left, 5000X magnification) of a nanosphere dimer (enclosed by the red square) and two nanosphere monomers (enclosed by the green and blue squares) both dispersed on a 45-nm-thick gold film. The right panel shows the pattern-matched optical dark-field image (100X magnification) for the same sample area. The scalar bars in both images are 2 μm The bigger green and red squares in the SEM image show magnified view of the nanoparticle monomer and dimer, respectively, with their scattering spectra shown in (c) under the un-polarized illumination configuration.

Figure 4.1b shows the pattern-matched scanning electron microscope (SEM, left panel) and true-color optical dark-field (right panel) images for a typical area of the sample used in our study, with the latter captured under an un-polarized illumination configuration with an upright microscope. Three single nanostructures, including two nanosphere monomers and one dimer, can be clearly seen in both images. In the dark-field image, the two gold film-coupled nanoparticle monomers show strong scattering in the green color band while the dimer efficiently scatters the orange light with intensity saturation, well consistent with the measured scattering spectra as shown in Figure 4.1c. The scattering spectrum of the monomer

exhibits two intensity peaks at wavelengths ~550 and 830 nm, labelled as modes (1) and (2), respectively. In addition to the two scattering peaks occurring at nearly the same spectral positions as that in the monomer case, the nanosphere dimer exhibits an additional scattering peak at ~660 nm labelled as mode (3), which has a much stronger intensity yet narrower spectral linewidth (FWHM: ~44 nm) than the other two mode peaks. As shown in the following, the mode natures of the three scattering peaks observed in both gold-film-coupled nanostructures will be investigated in detail by combining polarization-resolved far-field scattering measurements with electromagnetic simulations of surface electric charge distributions at the resonant wavelengths.

4.2 Spectral decomposition and color decoding of distinctive gap plasmonic modes

To get more insight into the observed plasmonic modes, I perform excitation polarization resolved scattering measurements for both monomers and dimers coupled to metal film with the polarization controllable illumination setup shown in Figure 4.1a (right), which permits an elegant decomposition of their un-polarized scattering spectra presented in Figure 4.1c. Figure 4.2a schematically depicts the s- and p-polarized incidence with respect to the two different orientations of the nanoparticles dimer. As can be seen from Figure 4.2b that the measured scattering spectrum of the film-coupled single nanosphere (case (i) in Figure 4.2a) illuminated by the s-polarized incidence exhibits only one peak at ~550 nm, which spectrally coincides with the mode (1) marked in Figure 4.1c, suggesting that this plasmon mode only responds to horizontal excitation polarization. This polarization dependence can be further verified by the surface charge distribution simulated for a gold film-coupled nanosphere as

plotted in the first column of Figures 4.3a and 4.3b, which seemingly, indicate the excitation of an electric quadrupole mode of single nanoparticle. However, the quadrupolar type plasmon is optically inactive mode which is hard to couple with the incidence[45,176–179]. Therefore, it must have been hybridized with the bright dipolar mode, leading to its manifestation in the radiation field[147,180]. Due to the involvement of the dipolar component, the radiation of the quadrupole is expected to behave like a dipole source in the far field as will also be confirmed afterwards by the radiation pattern with a solid far-field radiation pattern as illustrated in Figure 4.5b. In addition, Figure 4.3c shows that the field intensity at the quadrupole resonance is highly confined within the particle-film area. In contrast, the scattering spectrum shown in Figure 4.2b for the nanoparticle monomer under p-polarized illumination is dominated by an intense radiation peak at wavelength ~830 nm, agreeing with the wavelength position of the mode (2) marked in Figure 4.1c, and simultaneously a weaker peak at ~545 nm, similar to the mode (1) activated by the residual horizontal polarization component of the tilted p-polarized incidence. Therefore, this plasmon resonance corresponds to a vertically aligned bonding mode formed by the vertical coupling between the particle dipolar plasmon mode its induced dipole image in the gold film, fully confirmed by the simulated surface charge distribution as plotted in the second column of Figures 4.3a and 4.3b. The constructive bonding of this mode significantly strengthens the radiation into the far-field space and leads to a large field intensity concentration in the near field as can be seen from Figure 4.3c.

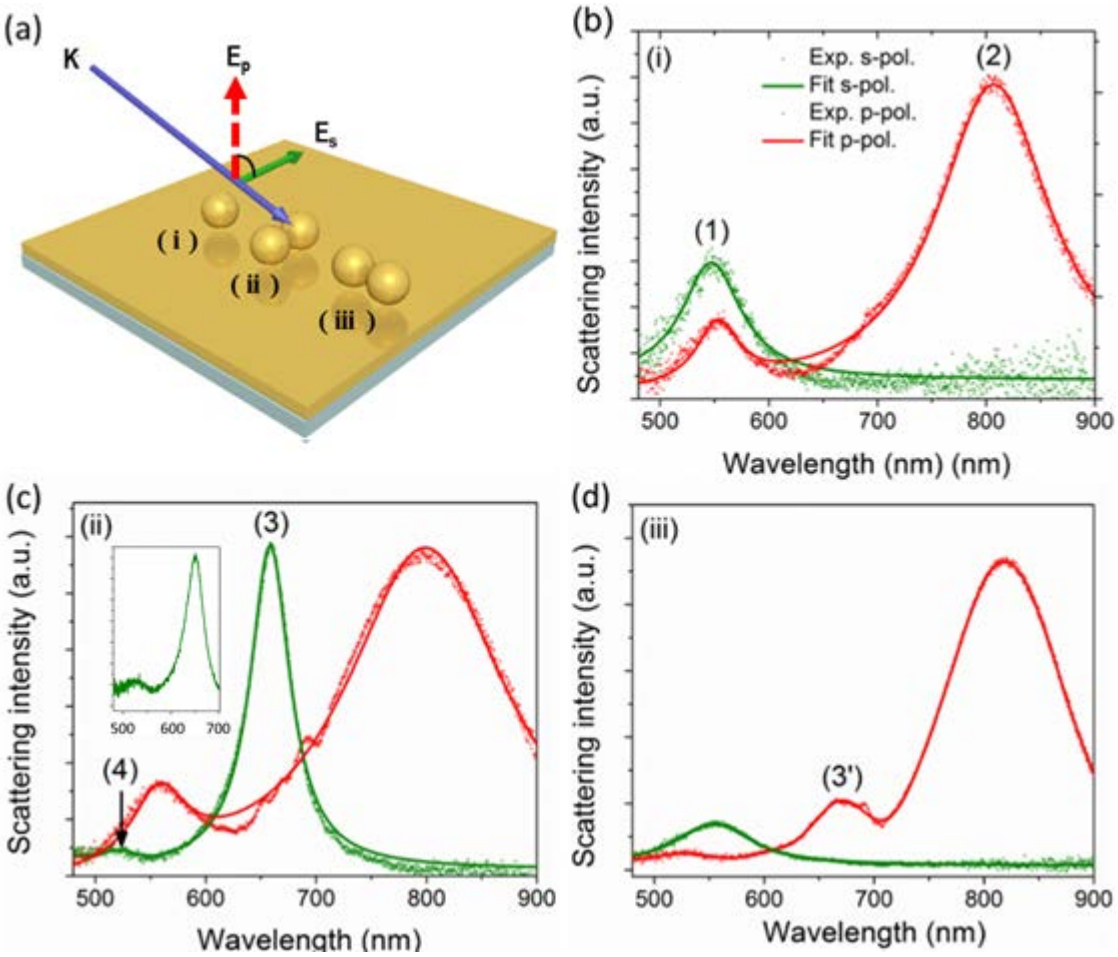

Figure 4.2 (a) Schematic illustration of the two incidence configurations with different polarizations for illuminating the gold film-coupled nanoparticles monomer and dimers. (b-d) Scattering spectra (dots) measured for single nanostructures of the three cases (i-iii) as labelled in (a) under the two orthogonal polarization incidence and the corresponding curve fits with the Lorentz function (lines).

Then we turn to the gold film-coupled nanoparticle dimers with the two orientation cases as depicted in Figure 4.2(a). With s-polarized incidence, Figure 4.2c shows that the scattering property of the dimer in case (ii) is spectrally featured by an intense yet narrow peak at ~660 nm, consisting with the similar spectral position of mode (3) in Figure 4.1c. Note the another spectral peak at ~530 nm, with much lower intensity, can be slightly observed and is labelled as mode (4). Additionally, these two modes totally disappear under when the incidence is switched to the p-polarization, suggesting that they are only associated with plasmon

oscillations along the dimer axis. The surface charge distribution of plasmon mode (3) shown in the third column of Figures 4.3a-b demonstrate that two anti-parallel horizontal dipole moments exists in each of the particle-film junctions. This destructive dipole pair should contribute little to the far field response of the associated plasmons. However, the charge distribution at the particle-particle gap fully resemble s to that of a nanoparticle dimer immersed in homogeneous medium, which suggests constructive dipolar bonding across the constitute particles, upon further coupled to metal film, still remains and can be the source of the strong far-field radiation at wavelength ~660 nm. The simulated charge distributions for the weak plasmon mode (4) in the fifth column of Figures 4.3a-b demonstrate its higher order origin as revealed by the distorted surface charge distribution features both at the particle-particle junction and particle-film junctions. In addition, for the plasmon resonance (3) and (4), the near field confinement does not solely occur at the particle-film regions, substantially enhanced field enhancement can also be found at the particle-particle region as shown in the last column of Figure 4.3c. The spectral response of the same dimer tunes to a completely different scenario under the p-polarized illumination: its scattering spectrum exhibits two peaks at the similar spectral positions as the modes (1) and (2) which are associated with the horizontal and vertical polarizations, respectively. Since the dimer-axis aligned polarization is absent in the incidence, the particle-particle coupling can be negligible, suggesting the two observed two modes originate respectively from the transverse antibonding (the higher energy one) between the particle dipoles and the vertical bonding (the lower energy one) of the individual particle dipole and its induced dipole image in the gold film.

Lastly, we address the spectral response of the nanosphere dimer in cased (iii). Since the dimer axis lies within the incidence plane, the s-polarized illumination can neither effectively

excite the gaps modes through particle-film coupling, nor trigger the longitudinal dipolar bonding between the constitute particles, leaving only the transverse particle-particle antibonding dominated far field response as indicated by the scattering peak at ~550 nm (Figure 4.2d). When switched to p-polarized illumination, three distinctive resonance modes can be identified from the scattering spectrum, with the strongest one at ~830 nm corresponding to the dipolar gap mode (2), the high order mode (4) ~530 nm and the third at ~670 nm labelled as mode (3′). Actually, this newly emerged plasmon mode (3′) is a hybridized resonance resulted from the coupling between the plasmon modes (2) and (3) as evidenced by the inherited surface charge distribution features from both modes (see the fourth panels of Figures 4.3a-b). As a result, the near- field intensity at this plasmon resonance can be simultaneously enhanced in both the interparticle and particle-film regions (as shown in Figure 4.3c). Since all the modes discussed above can be distinguished with specific polarization, a continuous polarization control as depicted in Figure 4.4a, will result in an alternative excitation of the different plasmon resonance, demonstrating a dynamic and flexible modulation of the abundant plasmon modes as showed in Figure 4.4(b-d).

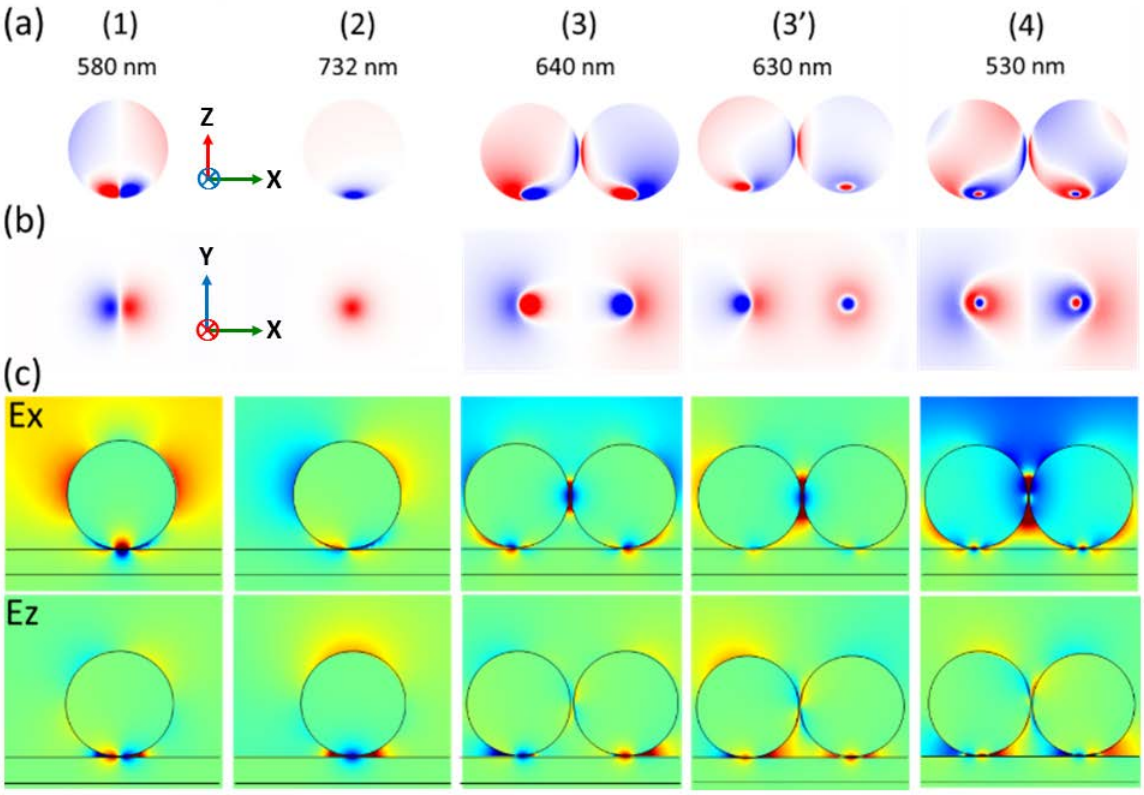

Figure 4.3 (a-b) Surface charge distribution simulated for both gold-film-coupled nanosphere monomers and dimers. For simplicity, the CTAB layer coated on the individual nanoparticles are modeled as air in simulations. For better visualizations of the particle-film gap regions, Note the charge distributions are separately showed in two different views for better visualizations of the particle-film junctions. (c) Intensity distributions of the field components E_x and E_z of the nanoparticles in (a-b) at the same mode frequency.

To shed more light on the correlation between the simulated near-field origins and the far field responses of each plasmon mode in the gold film-coupled nanoparticles, we strive to isolate the far-field radiation pattern of each plasmon resonance revealed above. In fact, the images captured for plasmonic nanoparticles with a typical optical microscopy system are simple spatial superposition of different colors (as indicated in Figure 4.4c), making it incapable to resolve the far-field radiation pattern of individual plasmon mode and consequently screening important features of its physical nature[181]. To address this issue, , we functionally updated the polarization resolved dark field spectroscopy system by introducing

the color decoding method from computer assisted image processing technologies. This technique can lead to a better "visualization" of the different radiative plasmon modes by

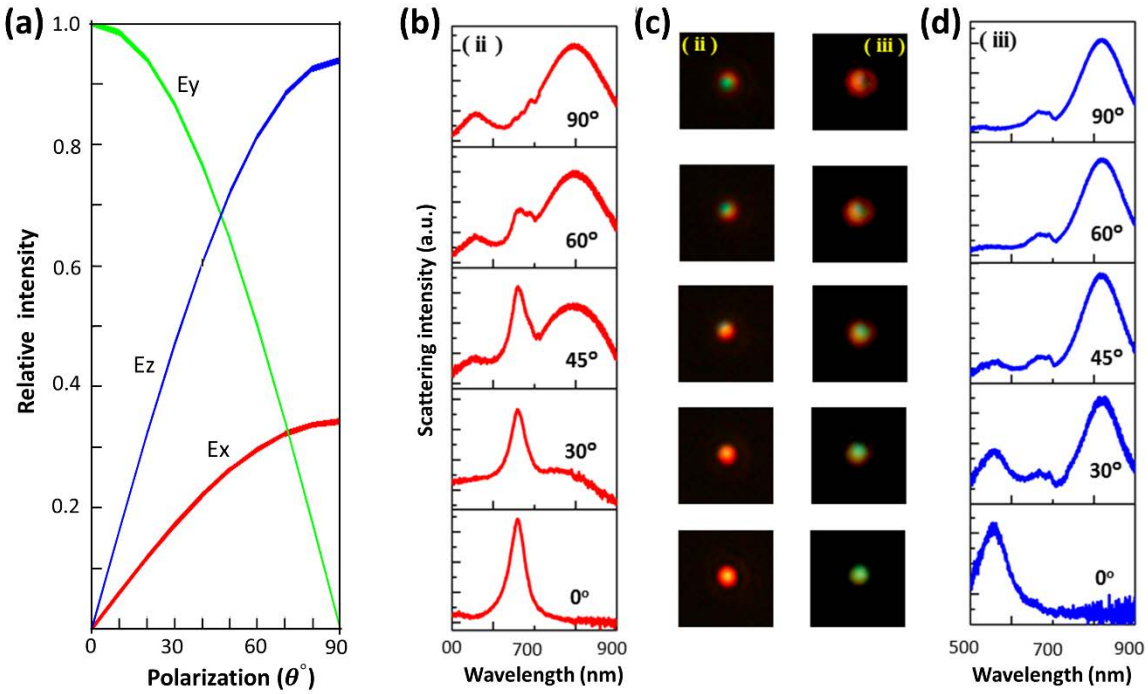

Figure 4.4 (a) Evolution of the field components intensity under different incidence polarization. The E_y component corresponds to the s polarization as depicted in Figure 4.2a, and is also correlated with the 0° polarization angle defined here. The E_z polarization is along the direction normal to the sample surface (90°). (b, d) Evolution of the scattering spectra of film-coupled dimers upon varied incidence polarization. The case (ii) and (iii) representing the different dimer orientations have been schematically depicted in Figure 4.2a. (c) The radiation patterns of the dimers with both orientation cases in (b) and (c).

extracting three grey images from the RGB channels of a single colorful image. This is feasible because the different plasmon modes of the metal film-coupled nanoparticles monomer and dimer can be well separated spectrally and selectively activated by using specific illumination polarization state as that discussed in Figure 4.2. Therefore, the illumination polarization control and color decoding method can be combined together to filter out the radiation pattern for individual plasmon mode.

Figure 4.5a shows a colorful dark field image of a micro-sized sample area containing a large number of nanoparticles on gold film. Note it's captured with the standard microscopy system in which the illumination is un-polarized. As can be seen, the radiation patterns of the nanoparticles in the image are featured by green or red colors which correspond to the plasmonic mode (1) at ~ 550 nm and mode (3) at 660 nm. The particles with green appearance in the yellow square are monomers while a monomer and a dimer can be identified in the blue square, which are confirmed by SEM characterization as exampled in Figure 4.1b.With the combination of polarization control and color decoding method, it can be expected that the plasmonic mode (1) at ~ 550 nm can be selectively imaged in the green channel ($500 - 600$ nm) of the CCD camera under the s-polarized illumination, in which other plasmonic modes are either suppressed in the excitation and/or imaged by other color channels. For clarity, this specific combination of illumination polarization and imaging channel conditions is termed as G-S combination. Similarly, the R-P combination, corresponding to red channel imaging under p-polarized illumination, can be chosen to enhance the imaging contrast in capturing the plasmon mode (3) at ~ 660 nm. The upper-right monochromatic image in Figure 4.5b is captured for the yellow square enclosed sample area in Figure 4.5a with the imaging condition of G-S combination, and each of the particle appear as a solid spot arising from the induced horizontal dipole moments as revealed by the near-field charge distributions shown in the first column of Figure 4.3a-b. Thus, successfully imaging the plasmon mode (1) of single nanoparticles coupled to film from the far-field domain has been achieved. When switching the illumination state to the p-polarization, the radiation pattern of each nanoparticle through mode (1) imaging becomes much darker largely due to the suppressed excitation of this mode. Then we switch the imaging configuration to

the red color channel, the pattern of the plasmon mode (2) at ~830 nm for the nanoparticles monomers can be clearly imaged under the p-polarized illumination, as shown in the lower-left panel. It can be seen that each of the particles exhibits a doughnut shape corresponding to a vertically aligned dipole source which originates from the dipolar bonding between the particle and its image in the gold film. Accordingly, the nanoparticles totally disappear in the upper-left panel of Figure 4.5b due to the suppression of mode (2) under s-polarization excitation. This way we have successfully imaged the two distinctive plasmonic modes (1) and (2) of the gold film-coupled nanoparticles with the different imaging configuration combinations based on code decoding and illumination polarization control. This approach can also be faithfully expanded to other complex nanostructure for imaging their individual scattering modes that are otherwise indistinguishable with the standard microscopy system.

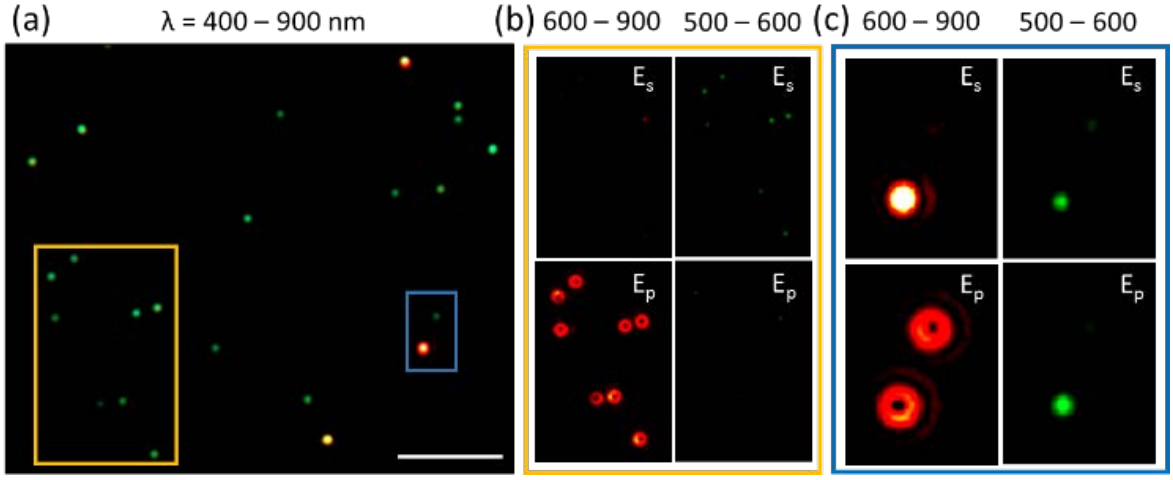

Figure 4.5 (a) Dark field image of nanoparticles (~100 nm) dispersed on a gold film. The rectangular areas labelled with different colors are of our interest and further analyzed in (b-c). The scalar bar is 5 μm. (b) Monochromatic images of the yellow rectangle enclosed area in (a) shot with different color channels (red in the left column and green in the right) under the illuminations with different polarizations (s-polarized in the upper panel and p-polarized in the bottom). (c) Enlarged monochromatic images of the blue rectangle enclosed area in (a), containing a nanoparticle monomer (upper position in the single image) and a dimer (lower position) both of which is captured with the same imaging configurations as in (b).

Then we expand the color decoding approach applied to the nanoparticle monomers to the simplest plasmon coupling system - nanosphere dimers, with the hope to resolve the different plasmonic modes from the far-field imaging. For clarity, we specially choose a sample area containing one nanoparticle monomer and one dimer as labelled by the blue rectangle in Figure 4.5a. The right columns of Figure 4.5c show the monochromatic images of the two nanostructures with green color channel under differently polarized illumination conditions, i.e., the G-S and G-P combinations, respectively. Different from the nanosphere monomer which appears as a solid spot with lower brightness under both polarized illuminations, the dimer shows a brighter solid spot pattern under the s-polarized illumination due to the invoke of the transversely anti-bonded dipolar mode (1) at ~ 550 nm. Moreover, when change the polarization into the p-polarized state, the dimer structure appears as a bigger and brighter spot which can be attributed to the excitation of the plasmon mode (4) at ~ 530 nm. Obviously, this large image contrast can provide an easy-performed approach to distinguish nanoparticles polymers with different orders in a wide-field microscopy configuration. However, the monomer and dimer show no noticeable difference in their red-channel rendered monochromatic images under p-polarized illumination (left-bottom panel), both showing dough-nut shaped patterns as a result of the excitation of the dipolar gap mode (2). In contrast, the monomer and dimer can be readily distinguished in the monochromatic image captured with the R-S combination. As shown in the left-upper panel, the dimer appears as a much brighter solid spot, corresponding to the strongly radiative mode (3) at ~ 660 nm, while the nanosphere monomer is totally invisible. Noted that, though the radiation of plasmonic modes (2) and (3) of the nanoparticle dimer lie in the similar wavelength the two

modes are all imaged with the same red channel, the different polarizations of the illumination permit their good separation in far-field radiation patterns.

4.3 A plasmonic nano-metrology for nanoparticle dimer orientation

As already demonstrated above that the far-field response of the gold film-coupled dimers show sensitive polarization dependence, we propose a polarization resolved nano-metrology combined with the code decoding method to determine the dimer axis direction. The dipolar mode (3) can strongly radiate into the far-field as a result of the in-phase plasmon bonding along the dimer axis, leading to a radiation highly polarized along the same direction. Therefore, the dimer orientation can be determined by monitoring the intensity of their radiation patterns as a function of the detection polarization in the monochromatic images with red color channel, yet the illumination is not necessarily polarized. This can be simply achieved with insertion of a light analyzer in the detection path.

A sample area containing two nanosphere dimers deposited on gold film are chosen as depicted in Figure 4.6a. The SEM image shows detail morphologies of the nanoparticles and are used to directly confirm the dimer orientations. Note the spatial alignment of the dimers cannot be directly distinguished form the dark field image as dose by SEM method. A series of monochromatic images collected with different polarizations are rendered in the red and green channels as presented in Figure 4.6b. As can be seen from the red-channel images, the patterns of both the two dimers show maximum (minimum) radiation intensities when the analyzer transmission axis is parallel (perpendicular) to the individual dimer axis. Therefore, the polarization dependence of the radiation intensity allows for a simple approach for

qualitative determination of the nanoparticles dimer orientation in a wide-filed microscopy configuration. Additionally, the monochromatic images rendered in the green channel show no noticeable intensity fluctuations with the rotation of the analyzer. For a more intuitive visualization of the dimer orientation qualitatively, Figure 4.6c plots scattering intensities of the two dimers as a function the detection-polarization. Here the scattering intensities are obtained by integrating of the intensity within the red-color channels for both dimers, and the polar plots read intensity maximum at polarization angle ~15° for the upper dimer and ~135° for the lower one, showing good agreement with the SEM characterization.

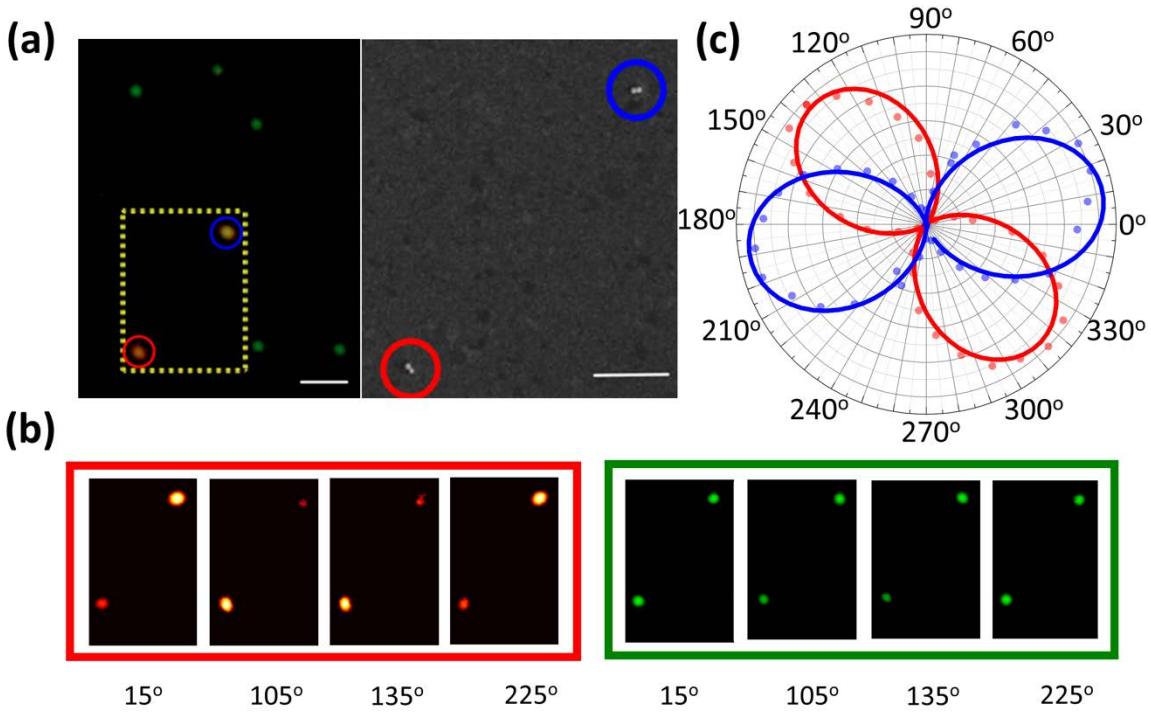

Figure 4.6 (a) Dark field image (left) containing two nanoparticles dimers and its corresponding SEM image (right), The dimer orientations of both dimers can be directly determined from the SEM image. The scalar bar in the dark field image is 5 μm, and 1 μm in the SEM image. (b) The monochromatic images of the two dimers in (a) rendered in the red (left) and green (right) color channels with different collection polarizations in the detection path. (c) Polar plot of the radiation intensity (dots) integrated within the red color channel of captured images for the two dimers labelled in (a). The curves with same color correspond to the nanoparticles labelled with the same color on (a). The solid lines are $cos^2\theta$ fits to the measured data.

4.4 Conclusion.

In this chapter, we have thoroughly uncovered the complex gap plasmonic modes of single gold nanosphere monomers and dimers respectively coupled to gold film using a spectral decomposition and color decoding method based on an excitation polarization control. Together with the electrodynamic simulation results, this method reveals that the individual film-coupled nanosphere monomer possesses two plasmonic modes, one corresponding to a weak transverse particle dipole moment and the other one to a vertical dipolar bonding between the particle dipole and its induced dipole image in the gold film. Besides to these two modes, the dimer placed above the gold film sustains the other two plasmon resonances, one originating from the tilted dipole bonding mainly along the particle-particle axis and the other one with obvious high-order features. Based on the highly polarization dependence of the far-field response, we have proposed a plasmonic nano-metrology method being capable to determine the orientation of nanosphere dimers with high signal to noise ratio and can be expanded to other complex plasmonic nanoclusters for details of their spatial arrangement. We believe the systematic investigations of the metal film-coupled monomers and dimers presented here will pave the way to further explore novel plasmon modes in more complex nanostructures coupled to metal film and probe the rich plasmon hybridizations involved.

Chapter 5 Metal substrate induced linewidth shrinking of the plasmon resonance in a nanoparticle dimer

Over the past decade, many strategies using plasmon hybridization theory have been developed to tailor the resonance profile of LSPs through generating, for example, sub-radiant and super-radiant modes and plasmonic Fano resonances[26,27]. These methods have been applied in many new types of metallic nanostructures, such as nanoparticle clusters or oligomers made from rational assembling of two or more individual nanoparticles into single symmetric or symmetry-broken entities[29,30,182]. Due to the strong capacitive electromagnetic interaction between constitute elements, these composite nanostructures are often featured with one or more near-field hot spots at their interparticle gap regions, which have offered a promising platform for surface-enhanced Raman scattering and photoluminescence spectroscopy[35–37]. In particular, reducing the symmetry of a nanocluster system relaxes the selection rules of dipolar coupling, resulting in effective plasmon hybridization of dipolar and higher-order modes[38,39]. This coherent mode coupling provides, beyond the scope of simply tuning the plasmon resonance position by varying nanoparticle size and shape, important possibilities for engineering the resonance linewidth and line-shape through radiative damping control[40,41].

Recently, Sobhani and Halas et al. demonstrated that the spectral linewidth of an aluminum nanoparticle plasmon resonance can be narrowed by a factor of 2 through near field coupling with an underlying aluminum thin film[183], where symmetry breaking induces the

plasmon hybridization between the dipolar and quadrupolar modes. This experimental realization provides the metal film-coupled nanoparticle system a new fascinating feature in addition to its intrinsic ultralow mode volume. They also pointed out that this mechanism appears to be general to plasmonic nanoparticle-film systems but far less effective for gold-based systems due to lower plasmon frequency. However, a strong yet quite narrow plasmon resonance for gold film- coupled nanosphere dimer is observed in my experiments. As already presented in last chapter, this plasmonic mode was supposed to be a hybridized mode produced by hybridization between the dipolar mode and high order mode. However, this assumption remains to be further confirmed due to failure in specifying the origins of the dipolar and high order modes involved.

To be continued, here we launch a comprehensive study on the linewidth shaping of plasmon resonance in metal film-coupled nanoparticles. By replacing a silica substrate with a gold thin film, it is found the dimer (monomer) exhibits a significant plasmon resonance linewidth shrinking by a factor of ~4.9 (~1.9), leading to a rather small FWHM of ~45 nm, fully consistent with the results by full-wave electromagnetic simulations. Together with theoretical analyses based on multipole expansion model, an intense plasmon hybridization has been confirmed between the dimer dipole mode, formed by longitudinally bonding of the two particle dipoles, and the quadrupole mode mediated by transversely bonding of the particle dipoles. Through plasmon hybridization, the significantly reduced radiation loss of the dipolar mode in the nanoparticle dimer results in a longer plasmon life and thus pronounced linewidth shrinking compared to the nanoparticle dimer in air or substrate with low dielectric constant. In addition, analysis of the linewidth narrowing effect of plasmon resonance in the frame of transformation optics was also performed, which suggests the

energy radiating into the far field has been reduced to a considerable extent, resulting an increased quality factor.

Section 5.1 will firstly present a quantification of the linewidth narrowing effect occurred in metal film coupled nanosphere monomer and dimer by comparison with their counterparts on silica substrate. Then in Section 5.2, theoretical analysis bases on the full-wave electromagnetic simulations as well as the multipole expansion mode will give a comprehensive understanding of the plasmon hybridization in gold film coupled nanosphere dimers. Finally, the metal substrate induced linewidth narrowing of plasmon resonance in the dimer case is revisited with the transformation optics model in the hope to offer an intuitive and analytical understanding of the plasmon interactions.

5.1 Metal substrate induced plasmon resonance linewidth narrowing

Here we use a fabrication trick to disperse the nanoparticle onto both the gold film and silica substrate simultaneously. By scratching the surface of a gold film deposited on silica substrate, parts of the gold film will be removed, leaving the bare silica substrate exposed to air as schematically depicted in Figure 5.1a. Then the nanoparticles are deposited on both of the substrate regions by drop-casting a colloidal droplet onto them as described in the previous chapters.

Figure 5.1b shows the dark-field images of the nanoparticles on the gold film and on the silica substrate (upper panel), along with the corresponding SEM images of the individual nanostructures labeled in the dark filed images (lower panel). One can see that on the gold

film the nanosphere dimer (monomer) produces bright far-field radiation in orange (green). In sharp contrast, the scattering intensities of both dimer and monomer on the glass substrate diminish significantly though the radiation colors remain similar as the gold film case. Figure 5.1c and d show the measured scattering spectra of two dimers and monomers on gold and silica under incident polarization along the dimer axis. The choice of this incident polarization can preferentially excite the bonding dipolar plasmon resonance without invoking other plasmon modes in the two dimers. The silica-supported dimer exhibits a scattering peak at around 650 nm, which is broader and red-shifted compared to the monomer counterpart (see Figure 5.1c), simply due to the stronger plasmonic coupling in the gap of the dimer. Upon positioned on the gold film, the scattering peak of the monomer shows a noticeable linewidth narrowing, which is consistent with the previous observations for similar systems by Halas[183] and Smith[165] and their coworkers. Surprisingly, Figure 5.1c shows that placing the dimer on the gold film leads to more pronounced linewidth shrinking than in the monomer case.

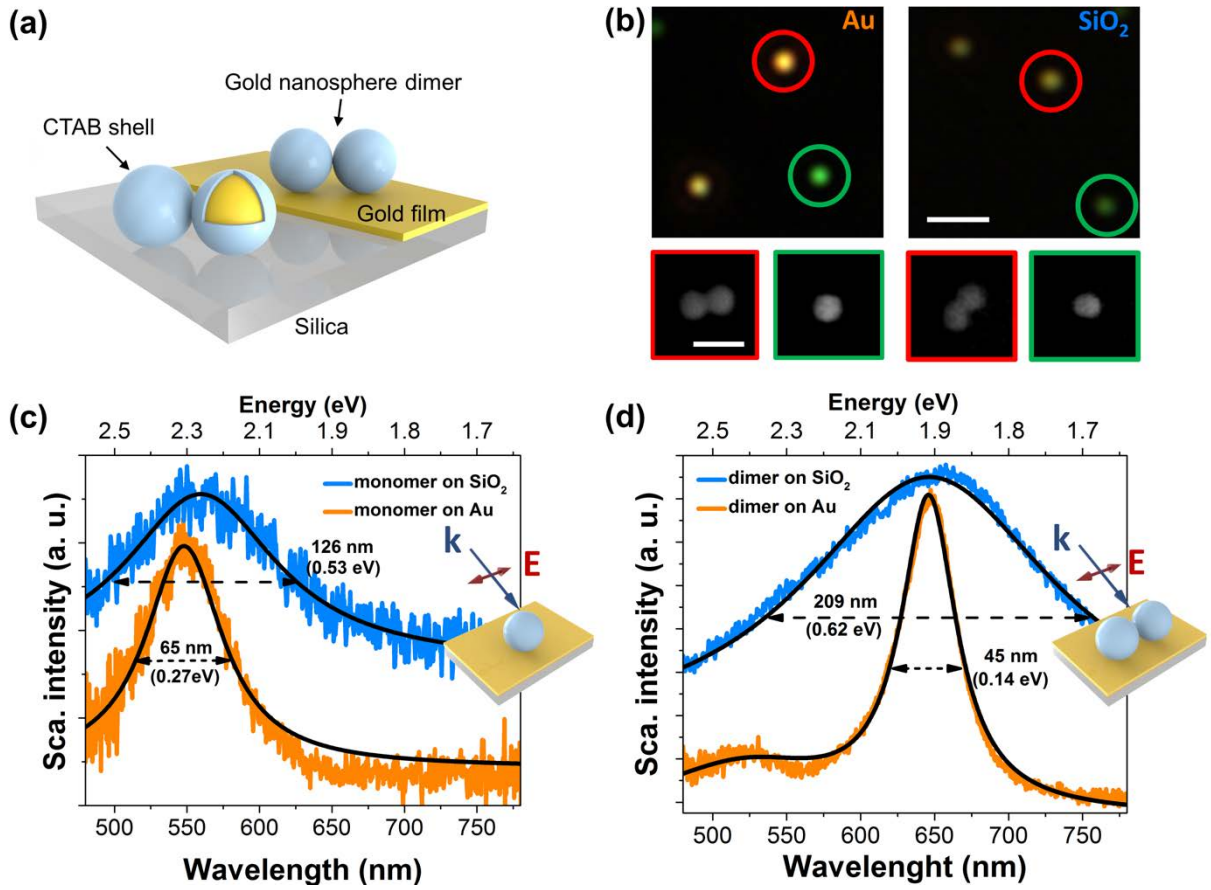

Figure 5.1 (a) Schematic of two CTAB-coated (light blue) gold nanosphere dimers positioned respectively on a thin gold film (yellow) and on a glass substrate (light gray). (b) Dark- field images of individual dimers and monomers on a 70-nm-thick gold film (upper-left) and on a glass substrate (upper-right). The SEM images of the nanoparticles labeled in the dark filed images (red circle enclosed dimer and green circle enclosed monomer) are presented in the lower panel. The scale bar is 3 μm in the dark field image and 200 nm in the SEM image. (c-d) Measured polarization-resolved scattering spectra of the gold nanosphere (c) monomers and (d) dimers on the gold film (orange) and on the silica (light blue). The insets depict schematically the excitation configurations used in the respective measurements. The sold lines are the fits with a Lorentz function.

To quantify the resonance linewidth narrowing, we determine accurately the full-width at half maximum (FWHM) of each scattering peak by fitting the peak with a Lorentz function. The fitting results suggest that, by replacing the silica substrate with the gold film, the FWHM of the 650-nm scattering peak in the dimer reduces from ~209 to 45 nm, narrowed by a factor of ~4.6. However, this linewidth shrinking effect is less effective for the monomer case where the FWHM of the 550 nm scattering peak reduces from 126 to 65 nm (narrowed by a factor of

1.9). In other words, although the dipolar plasmon resonance of the nanosphere monomer on silica is spectrally broadened upon coupled to a second nanosphere nearby to form the dimer (FWHM increased from 65 to 209 nm), the introduction of the metal film can remarkably narrow the spectral linewidth of the new resonance from 209 to 45 nm. As a result, a more surprising and counterintuitive observation is that, by placing the second gold nanosphere near the film-coupled monomer, the scattering peak FWHM of the newly-formed film-coupled dimer can further be narrowed from 65 to 45 nm. Considering the dominated role of dipolar radiation damping responsible for the resonance linewidth broadening in typical plasmonic nanoparticles with relatively large sizes[184–186], the remarkable linewidth narrowing effect in the gold film-coupled dimer implies a significant reduction in radiation losses when brought in close proximity to the metal film.

In addition to the resonance linewidth shrinking effect discussed above, the light scattering intensity of the gold film-coupled dimer is significantly increased, in comparison with the silica case, by 3-fold as shown in Figure 5.2a. It has been proposed that the field reflected by the metal film can add to the exciting field and therefore causes a stronger scattering efficiency for the metal film-coupled nanoparticle[183]. Here we numerically simulate the far-field radiation pattern at the scattering peak wavelength 650 nm for the dimers on silica and gold (details of the simulation model shown in Figure A2 in the appendix part). As can be seen from the results in Figure 5.2b, the silica-supported dimer mainly radiates to the substrate side, leaving only a small amount of the scattered light within the collection angle of the objective lens atop the sample. In contrast, almost all the far-field radiation of the gold film-coupled dimer are injected into the superstrate side, and thus the majority amount of the

scattered light falls into the collection angle of the objective, resulting in the much brighter radiation spots than the former case as compared in the dark-field images of Figure 5.1b

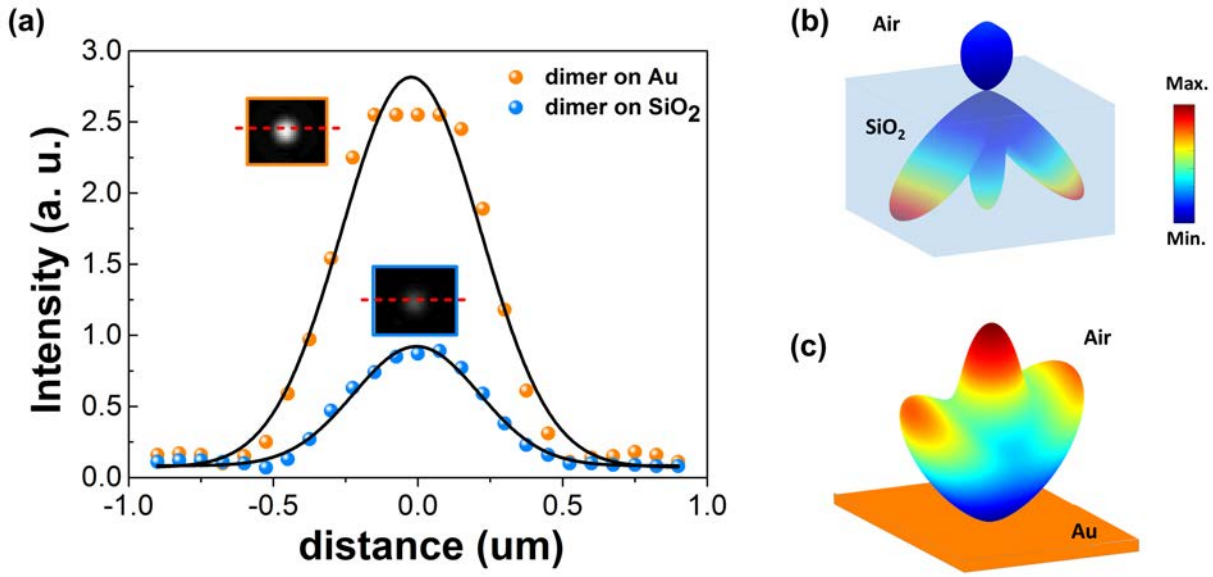

Figure 5.2 (a) Measured scattering intensity profiles for the silica-supported (blue) and gold film-coupled (golden) dimers in the far-field imaging plane. The data points, corresponding to the intensity values along the dashed line in the dark-field images, are extracted from the red channel of the detector which mainly covers the radiation of the plasmon band centered at ~650 nm. (b, c) Calculated far-field scattering patterns at the plasmon resonance 650 nm for the silica-supported (upper panel) and gold film-coupled (lower panel) dimers.

5.2 Metal substrate mediated dipolar-quadrupolar plasmon hybridization.

To uncover the physical mechanism responsible for the drastic resonance narrowing observed above, here we combine full-wave electromagnetic simulations with an analytical multipole expansion model to calculate the near-field distribution and far-field response of the gold film-coupled and silica-supported nanosphere dimers, respectively. Figure 5.3a and b show the simulated polarized scattering spectra of the monomers and dimers on gold and silica under a same excitation condition as used in experiment (depicted in the inset of Figure 5.1c and d), which show good agreement with the measured spectra by reproducing the

scattering peak magnitude and linewidth shrinking of the plasmon resonance in the presence of the gold film. For simplicity, the CTAB surfactant shell was modeled as air in the simulation, leading to a slight blue-shift in the simulated scattering peaks compared to the measured ones. Figure 5.3c presents the charge distribution profiles corresponding to the scattering peaks identified from Figure 5.3b, i.e. 648 nm for the silica-supported dimer (upper) and 635 nm for the gold film-coupled dimer (lower). Note that the gold film and the glass substrate are placed in the XY plane as seen from the top view, and that for better visualization of the charge distribution at the bottom gap junction the dimer is tilted by an angle of 45^{o} in the YZ plane. The left column shows that the induced surface charges are mainly concentrated within the lateral sphere-sphere gap junction in the silica-supported dimer, resembling that of the bonding dipolar mode of a nanosphere dimer in a homogeneous medium, except the negligible induced charges at the bottom of the nanoparticles. In sharp contrast, the gold film-coupled dimer presents a distorted charge profile with surface charges accumulated within both lateral sphere-sphere and vertical sphere-film gap junctions (right column).

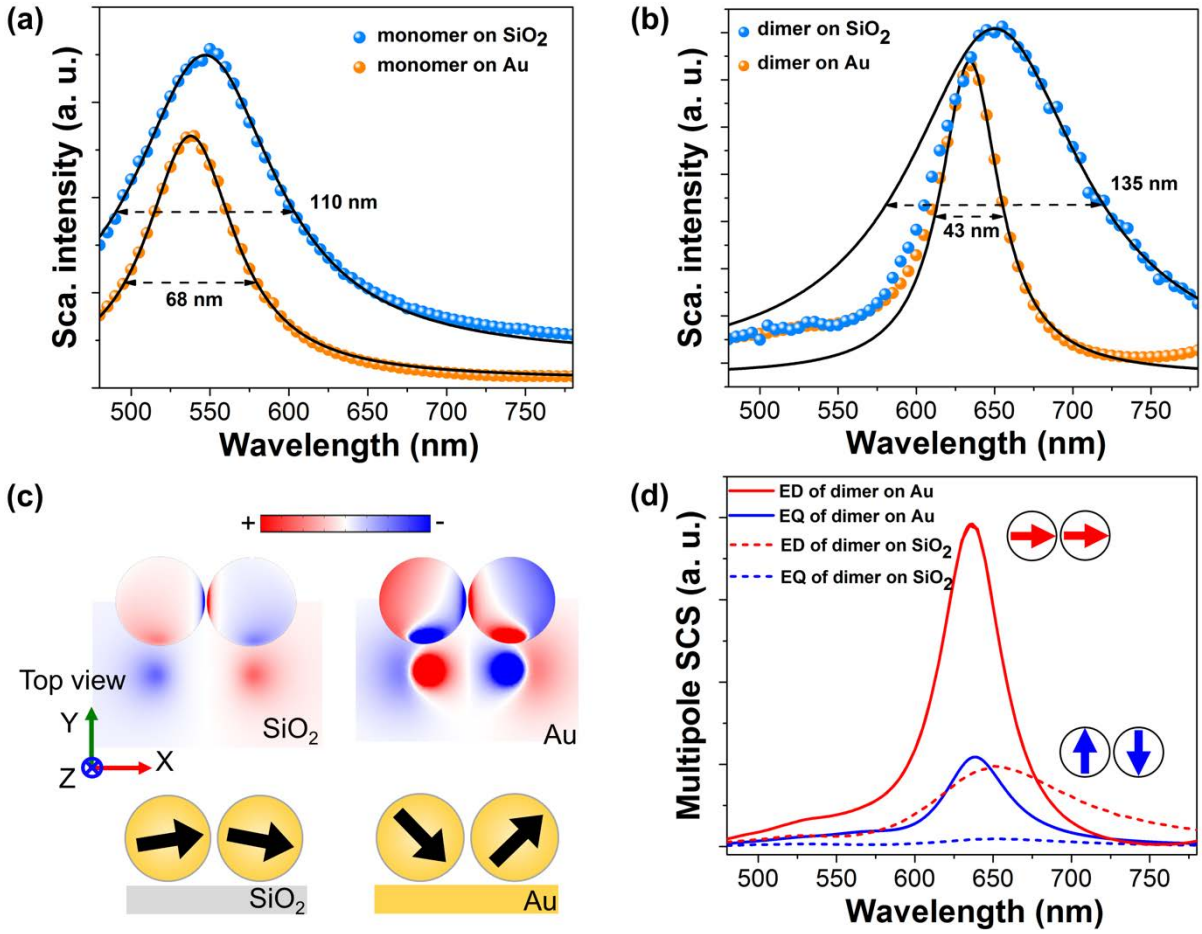

Figure 5.3 (a-b) Simulated polarized scattering spectra of the gold nanosphere monomer (a) and dimer (b) on the gold film (orange dots) and on the silica substrate (blue triangles). The solid lines are the fits with a Lorentz function. The excitation conditions are the same as experiment as depicted in Fig. 2b. (b) Surface charge distribution profile and deduced charge dipole interaction representation for the silica-supported dimer (upper panel) and the gold film-coupled dimer (lower panel) at their scattering peak wavelengths extracted from (a). Note that all the charge distribution profiles are viewed in the substrate plane (XY lane). The dimers are tilted by an angle of 45o with respected to the substrate normal for better visualization of the charge distribution within the nanosphere-substrate gap. (c) Multipolar expansion analysis of the respective contribution from the electric dipole (ED) and quadrupole (EQ) to the total scattering cross sections of the two systems studied in (a). The insets depict the bonding dipolar mode (red) and the quadrupolar mode (blue).

To have an intuitive understanding of the complicated electromagnetic coupling in the dimer systems, the plasmon hybridization model developed by Nordlander et al. is applied to

reveal the underlying physics from the perspective of plasmonic dipole-dipole interaction[31,34,140,187,188]. Based on the simulated charge profiles shown in Figure 5.3c, the plasmon interaction in both dimers can be schematically represented with charge dipoles of different orientation and strength as shown in the lower part in each panel of Figure 5.3b. In the silica-supported dimer, the surface charge density is weakly screened by silica substrate, thereby breaking the symmetry of the charge distribution along the substrate norm and giving rise to a tilted bonding dipolar mode on the dimer. Due to the relatively small electric permittivity of silica, the magnitude of the induced charge in the substrate is so weak that its screening effect on the bonding dipole mode is negligible, leaving the broad scattering peak observed in both simulation and experiment. For the gold film-coupled dimer, however, the magnitude of the induced image charges can be very strong due to the presence of a sea of conduction electrons in the gold film, resulting in the strongly distorted dipolar alignment on the dimer which can be decomposed as a horizontally bonding dipolar mode and a quadrupolar mode (formed by two vertically bonding dipolar mode) as illustrated in the insets of Figure 5.3c. The strength of the two induced vertical dipoles in the quadrupolar mode on the dimer can be comparable to the two horizontal bonding dipoles on the dimer, thereby allowing for intensive plasmon hybridization between them. Note that similar surface charge distribution for the film-coupled dimer was already presented in the last chapter, and here it is replotted for necessary comparison with the silica substrate case and for the deduction of the plasmon hybridization scenario.

Up to now, several studies have demonstrated linewidth shaping of plasmon resonances in metal nanostructures through the concept of mode hybridization[38,39,189,190]. Of particular interest is to relax the requirement of the dipolar coupling selection rules by reducing the

symmetry of a plasmonic system, resulting in an admixture of highly-radiative (or bright) dipole and nonradiative (or dark) higher-order modes. The dark mode, when coupled to the bright mode, will acquire part of the energy from the bright mode, thereby reducing the radiation loss of the system. As mentioned earlier, this concept has recently been verified by Sobhani et al. by realizing significant plasmon resonance linewidth narrowing in an aluminum film-coupled aluminum nanosphere through dipole-quadrupole mode hybridization[183]. Although the semi-analytical model used in their study can well explain the observed linewidth shrinking effect and predict less effective linewidth narrowing for a gold film-coupled nanosphere monomer due to lower plasmon frequency, it cannot be directly applied to our metal film-coupled nanosphere dimer system due to the reduced in-plane symmetry by the horizontal dipolar bonding. To uncover the mode hybridization induced linewidth shrinking in the film-coupled dimer, here we adopt a multipolar expansion model with which the respective radiation contribution of electric dipolar and multipolar moment to the total far-field scattering intensity can be distinguished. The far-field radiation that originates from the induced displacement current in a nanosphere can be described in terms of a vector potential $A(r)$, which, in the quasi-static approximation, could be expanded into multipoles as[32]

$$\mathrm{A}(r) = -i\omega\mu_0 P \frac{e^{ik_0 r}}{4\pi r} + \frac{i\omega\mu_0}{2} Q \cdot \nabla \frac{e^{ik_0 r}}{4\pi r} \qquad (5.1).$$

where P and Q are the electric dipole and quadrupole moments, respectively, under the $e^{-i\omega t}$ time conversion. Higher order terms in the multipole expansion can be neglected due to the subwavelength size of the constituent nanospheres studied in our experiment. The contribution from each term is displayed in Figure 5.3c on the same scale. While the electric dipole dominantly contributes to the total far-field scattering intensity for the gold film-

coupled dimer, the contribution of the quadrupolar moment is considerable due to the energy injection from the dipolar mode through mode hybridization. As a result, the larger quality factor of the quadrupolar mode increases the dephasing time of the hybridized plasmon and thus dramatically reduces the radiation loss of the dipolar mode, leading to the significant linewidth shrinking effect. Comparatively, in the silica-supported dimer, the quadrupole contribution is almost zero, leaving the broad dipolar plasmon resonance nearly unaffected and dominated in the total scattering spectrum.

5.3 Within the transformation optics frame

To offer a more intuitive and analytical understanding of the plasmonic interaction in the gold film-coupled dimer system, the theory of two-dimensional conformal transformation optics is deployed to relate the original system to a simpler one with higher symmetry, following the approaches developed in the previous works[191–193]. The inversion transformation defined by

$$\xi' = \frac{g^2}{\xi - R_0} \tag{5.2}$$

with $\xi = x + iy$ and $\xi' = x' + iy'$, transforms a film-coupled nanowire dimer system in the physical frame into an annular system with an extra nanowire corresponding to the semi-infinite substrate, as shown in Figure 5.4a and b. Points at infinity are mapped to the inversion point, R_0, and the incident fields are converted into a dipole source at the inversion point. When the dimer is placed on a gold substrate, compared with the dimer on a silica substrate, the surface plasmons oscillating at the metal surface create a stronger substrate effect. The plasmonic interaction drags down the charges and confines them in the narrow gap between

the dimer and the substrate. The effective dipole moment of the dimer is therefore decreased due to the distraction of charges to the dimer-substrate gap, which is confirmed by the contour plot of the calculated magnetic field (representing the distribution of induced surface charges, see Figure 5.4c). Consequently, optical radiation into the far-field regime is suppressed and the quality factor of the scattering resonance becomes larger than that of the dimer on silica. Alternatively, if viewed from the transformed frame, the near-field energy is mainly distributed along the horizontal direction due to the symmetric nature of the annular system. However, after introducing the gold substrate, which can be transformed into a nanowire tangent to the inversion point with radius $g^2/2d$, the near-field energy is now concentrated at the intermediate space between the nanowire and the annular system due to significant charge accumulation (see Figure 5.4d). Thus, the energy at the inversion point, which corresponding to the energy radiated into the far-field regime in the physical frame, is reduced to a considerable extent, resulting in the increase of the quality factor.

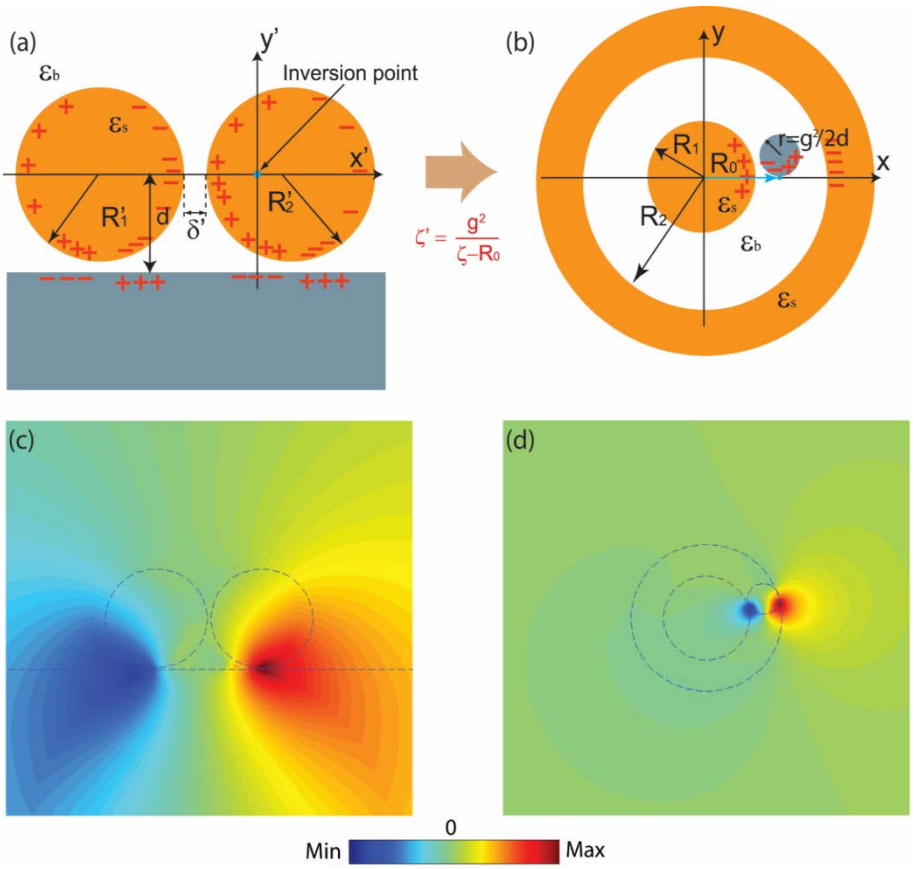

Figure 5.4 (a, b) Schematics of the two-dimensional conformal transformation from a nanowire dimer on a substrate to an annular system with an extra nanowire, through performing an inversion transformation. (c, d) Real part of the magnetic field in the (c) physical and (d) transformed frame at wavelength 500 nm.

5.4 Conclusion

In conclusion, we have experimentally demonstrated in this chapter that the spectral linewidth of the dipolar plasmon resonance in a gold nanosphere dimer can be significantly narrowed by replacing a silica substrate with a gold film. Moreover, the measured linewidth of the film-coupled dimer is even smaller than its monomer counterpart (~30% reduction). This pronounced narrowing effect has been supposed to have much to do with reduced radiation loss induced by plasmon hybridization between dipolar plasmon mode and high

order modes. Analysis based on electromagnetic simulations and multipole expansion model confirms the origins of the dipole and quadrupole mode. The intense interactions between the bright and dark mode mediates an energy transfer from the former to the latter which substantially reduces the decay rate of the dipolar plasmon resonance and leads to the considerable linewidth narrowing of the radiation mode. Calculations within the transformation optics are also performed to address the pronounced linewidth effect and reveal the increased energy stored in the near-field results in the significantly radiation loss into the far field and thus high quality factor of the radiative plasmon mode.

Chapter 6 Plasmon hybridization enhanced photoluminescence in metal-film-coupled nanoparticle dimers

Due to the inhibition of radiation losses, a dark quadrupolar mode, by virtue of having a vanishing moment, can be more efficient than a bright dipolar mode to store electromagnetic energy in the near-field domain, and thus can provide stronger enhancement for various surface-enhanced spectroscopies[194–196]. In the last chapter, we have demonstrated a hybridized plasmon resonance formed by intense plasmon hybridization between a radiative dipole mode and a dark quadrupole mode in the gold film-coupled nanosphere dimer structure. Thus, it's expected that the quadrupole-dipole hybridized mode in this structure can significantly prompt optical processes occurring within its nanoscale gaps, in a more effective manner than the silica-supported dimer. In the meanwhile, the narrowed plasmon linewidth, corresponding to a higher quality factor, which is favorable to many plasmon-enhanced radiation phenomena, makes the film-coupled dimer structure a promising platform for modulating the radiation properties of an optical emitter positioned inside its gap region.

Specifically, the multiple nanoscale gaps in a metal film-coupled nanoparticle dimer offer more than one electric hot spots as depicted in Figure 6.1a (right panel). Moreover, even the hot spots in particle-film gaps can be lighted upon an excitation with in-plane polarization along the dimer axis. This is quite important for a metal film-coupled nanoparticle structures because the effective in-plane polarized excitation largely relaxes the requirements of a sufficient vertical polarization component to light the particle-film gaps which, however,

cannot be readily achieved in a typical spectroscopy platform. To fully evaluate the promising of the preferred particle-film gap regions in potential spectroscopy applications, some insights into light-matter interactions within the gap regions have to be offered. As label-free and non-bleaching metal molecules, gold nanoparticles have been widely used in bio-imaging and sensing applications. Here together with calculations and experiments on photoluminescence, we strive to shed more light on the light-matter interactions within the gap regions in the nanosphere dimers on film structures.

In Section 6.1, we will perform photoluminescence measurements over both silica and gold film supported nanosphere dimers and compare their PL emission in intensity and spectral profiles. Based on the experimental observations, in Sections 6.2, we propose the possible physical mechanisms of the photoluminescence emission in both nanostructures. Finally, we will carry out some calculations in Section 6.3 to verify the assumed PL emission model and in further, evaluate the PL emission in each gap region in the metal film coupled dimers. These results are believed to offer deeper insight into the photoluminescence emission in complex plasmonic nanostructures and guidance in design of related photonic devices

6.1 Photoluminescence enhancement in gold-film-coupled nanosphere dimer

The samples for photoluminescence measurements include the gold nanosphere dimers on gold film and silica substrate, respectively. The fabrication methods have been previously addressed in Section 3.1 and 4.1. The measurement setup has been schematically depicted in section 3.2.4 of chapter 3. Specifically, the laser of 633 nm wavelength is used to achieve the near-resonant excitation. The 100X objective with $\mathrm{NA} = 0.9$ is chosen for high collection

efficiency of emissive sample in the focal plane. To avoid possible photothermal damage to the nanostructures under laser irradiation, the incident laser power was kept at a moderate level, ~0.5 mW, equivalent to a power density of 1.6×10^4 W/cm^2 at the sample plane. The scattering spectrum of the gold film-coupled dimer measured after the PL measurements resembles the initial spectrum, further confirming no perceivable photothermal damage occurred (see appendix A5). Note the PL collection for the gold film-coupled nanoparticles is performed from the film side while that for the glass supported ones is from the glass side. More details of the experimental setup can be addressed in Section 3.2.4.

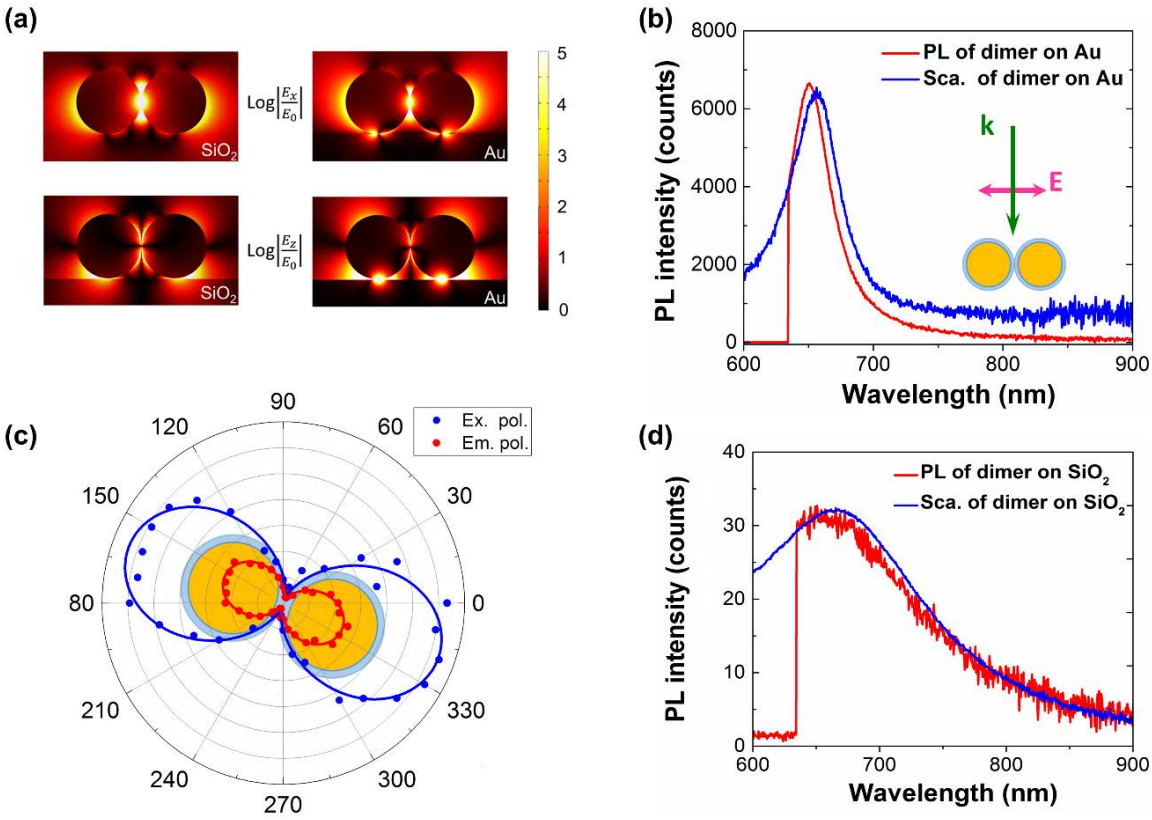

Figure 6.1 (a) The intensity distributions of the electric field components in both silica (left) and gold film (right) coupled nanosphere dimers upon dimer-axis polarized excitation at the resonant wavelength ~$648nm$ (b, d) Measured PL spectra of (b) the film-coupled gold nanosphere dimer and (d) the silica-supported dimer, both under illumination by 633 nm laser with polarization direction along the dimer axis as depicted in the inset. The corresponding scattering spectra measured for both dimers (blue curves), both under white-light illumination with polarization along the dimer axis, are overlaid on their PL spectra for spectral characteristics comparison.

(c) Excitation (blue) and emission (red) polarization dependent PL intensity of the film-coupled gold nanosphere dimer (yellow-blue core-shell). The magnitude of each data point is an intensity integral over a wavelength band of $20nm$ centered at the emission peak. Similar results for the silica-supported dimer are shown in Figure A4 in the appendices section

As can be seen from Figure 6.1a, upon resonant excitation ($\sim$648 nm) with polarization along the dimer axis, the metal film-coupled particle dimer shows intense field concentration in all the three gap regions while in dimer on silica the electric field is mainly confined in the particle-particle gap. Due to the involvement of dark quadrupole component of the plasmon resonance in the dimer on film, the strong field intensity in the particle-film gap regions are expected to more efficiently prompt the excitation rate of photoluminescence emission. Figures 6.1b and 6.1d show respectively the PL spectra of the gold film-coupled and silica-supported dimers measured with the incidence polarization along the dimer axis. Note that the cut-off in the PL spectra at wavelength shorter than 630 nm is due to the cut-off response of the dichroic mirror that is used to filter out the excitation laser band and allows the long-wavelength emission to pass through. The PL spectrum of the film-coupled dimer is featured with a substantially enhanced ($\sim$200 times) yet narrowed ($\sim$4.6 times) emission peak compared to that of the silica-supported dimer. In particular, the PL spectral profile of each dimer inherits its scattering spectral characteristics – nearly the same radiation peak position and linewidth. These spectral similarities between PL and scattering for both dimers imply a plasmon decay mediated emission mechanism as elucidated in the following.

6.2 Radiative plasmon decay dominated photoluminescence emission in nanoparticle dimer on dielectric and metal structures

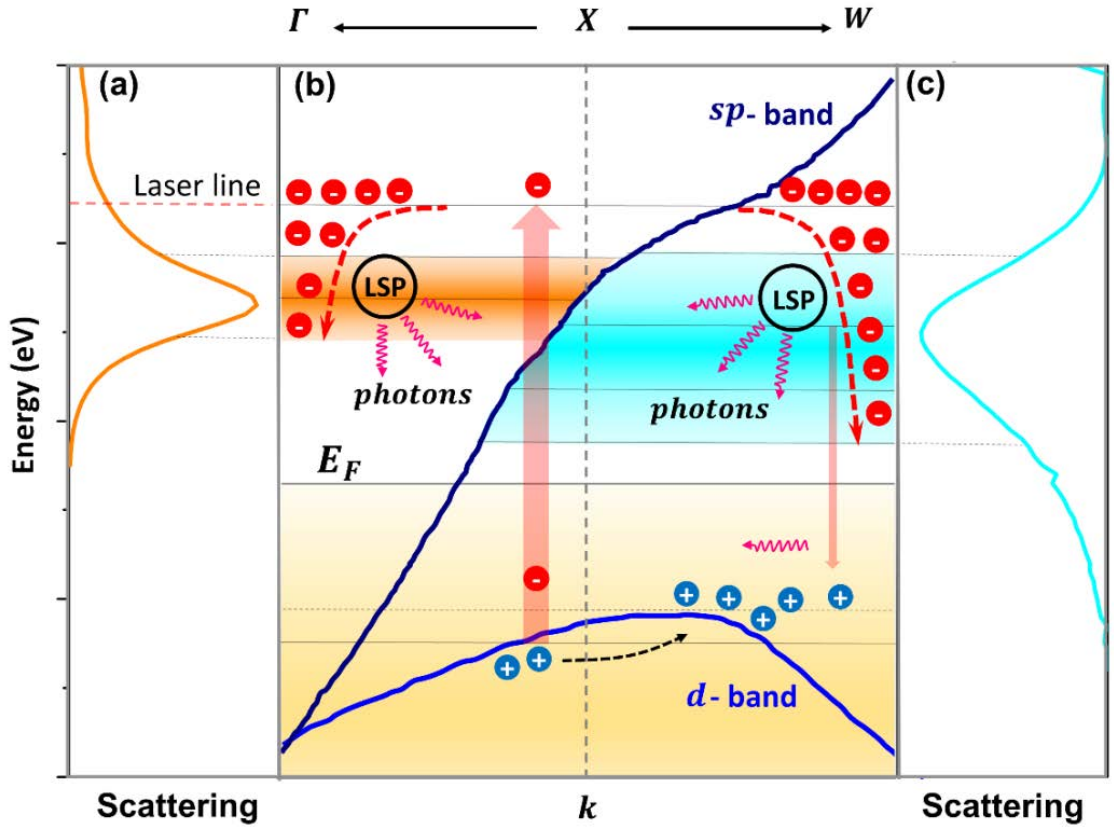

Figure 6.2. Schematic diagram elucidating the plasmon-mediated photoluminescence emission processes in both gold and silica supported dimers. (a, c) simulated scattering spectrum of (a) the film-coupled dimer and (c) the silica supported dimer, respectively. The red dashed line represents the laser line. (b) Energy diagram of gold band structure near the Fermi level around the X point in the first Brillouin zone. The thick upward arrow represents the transition of a d-band electron to the sp-band by absorbing a 633 nm photon. The photoexcited electron will decay non-radiatively into a localized plasmon resonance energy matched band with exponentially decreased population redistribution (dashed red arrows). The majority of the accumulated energetic electrons within the LSP band will decay radiatively, giving rise to the PL emission, while the minority may recombine directly with the photoexcited holes within the top region of the d-band and emit photons (thick downward arrow), similar to the photoemission process in bulk gold.

Figure 6.2b schematically depicts the band structure of gold near the Fermi level around the X point in the first Brillouin zone, while Figures 6.2a and 6.2c show the calculated

scattering spectra representing the magnitude of the local density of plasmonic states (LDoPSs) of the film-coupled dimer (Figure 6.2a) and the silica-supported dimer (Figure 6.2c), respectively. By analogy to the spontaneous emission process of an emitting dipole, a dipolar-like plasmon mode can decay in radiative and nonradiative channels. The radiative decay rate is proportional to the LDoPS in the same way as the radiative decay γ_{rad} of an emitter linearly depends on the local density of optical states (LDOSs) $\rho(\omega)$, following $\gamma_{\mathrm{rad}}(\omega) = \frac{\pi\omega}{3\hbar\epsilon_0}|p|^2\rho(\omega)$, where p is the transition dipole moment of the emitter. More details on the LDoPS calculations are given in the appendices section. Through single-photon absorption processes, a large number of the *d*-band electrons in gold can be excited into higher energy levels in the sp-band, simultaneously leaving plenty of energetic holes in the d-band. The accumulated photoexcited electrons will then decay non-radiatively into the energy-matched LSP band of the dimer, with an exponentially decreased population distribution[197] that accounts for the slight blue-shift in the PL emission peak with respect to the corresponding scattering peak in both dimers (see Figures 6.1b and 6.1d). The energetic electrons within the LSP band can either recombine directly with the photoexcited holes within the top region of the d-band through interband transitions, emitting depolarized photons[77,198], or decay radiatively via plasmon damping, emitting plasmon-modulated polarized photons. Note that the plasmon-decay mediated photoluminescence emission is mainly determined by the LDoPSs that could be very large at the LSP resonance band, thereby leading to an increased radiative decay rate and enhancing the emission intensity. In general, the two emission processes occur simultaneously, and the contribution of each decay channel can be evaluated by the degree of polarization (DoP) of the emission, defined as $(I_{\max} - I_{\min})/(I_{\max} + I_{\min})$, where $I_{\max}$ and $I_{\min}$ are the maximal and minimal emission intensity in the polarization-

resolved PL measurement. The highly linearly polarized emissions from both film-coupled (DoP ~0.88 for detection polarization in Figure 6.1c) and silica-supported dimer (DoP ~0.71 in Figure A4) indicate that the radiative plasmon decay substantially dominates over the interband transitions in their PL emissions and the larger emission DoP observed in the film-coupled dimer imply a more pronounced plasmon emission over its counterpart on the silica substrate.

6.3 Quantitative evaluation of photoluminescence enhancement and enhancement sites

In this section, we provide a quantitative evaluation on the PL intensity and the PL enhancement sites in the two systems. In light of their geometric features, we infer that the PL emission enhancement in the film-coupled dimer is mainly contributed by the two vertical sphere-film gaps rather than the horizontal sphere-sphere gap. To evaluate the quantitative contribution of each gap to the total emission intensity, we calculate the relative PL spectra of both dimers using a generalized one-photon luminescence model. According to the general theory of single-photon absorption induced photoemission, the photoluminescence from a volume element dV in a material can be expressed as[199]

$$I_{PL}(\omega)dV = I_0(\omega_0, \vec{r})Y_{abs}(\omega_0)Y_R(\omega)Y_{em}(\omega)dV \tag{6.1}$$

where ω_0 and ω are the angular frequency of the excitation and emission, respectively. $I_0(\omega_0, \vec{r})$ is the field intensity of the excitation at point $\vec{r}$. $Y_{\mathrm{abs}}(\omega_0)$ is the absorption probability of a single photon at ω_0. Y_{R} is the relaxation probability of photoexcited carriers from an excited state to an emission state, and $Y_{\mathrm{em}}(\omega)$ is the emission probability of radiative

recombination at the frequency ω. The following assumptions were made in the calculations. (i) The absorption probability $Y_{\mathrm{abs}}(\omega_0)$, which is determined by the imaginary part of the gold dielectric function due to the interband transitions at the excitation frequency ω_0, can be assumed to be constant[200]. (ii) The relaxation probability Y_{R}, as an indication of the population redistribution of the photoexcited electrons in the sp-band, corresponds to their nonradiative decay to the emission states, i.e. lower-energy levels within the sp-band for bulk gold and the LSP band for the gold nanosphere dimer. The frequency dependence of this term is associated with the intrinsic bulk properties and this probability is confirmed to be exponentially decreased with decreasing the frequency below the excitation level as depicted by the dashed red curve in Figure 6.2. In a plasmon decay dominated emission process, the effect of the emission frequency dependence of Y_{R} is manifested by the slight blue-shift in the emission peak with respect to the scattering peak[197] as shown in Figure 6.1b and d. In the following calculations, the contribution of Y_{R} to emission intensity of both dimer systems, therefore, can be assumed to be equal and excluded from equation (3) for a relative intensity comparison. (iii) $Y_{\mathrm{em}}(\omega)$, the emission probability of radiative recombination in bulk gold can be modified to associate with the plasmon radiative decay rate in the dimer, which is determined by its LDoPSs that is proportional to the field intensity at the emission frequency[71,200]. For comparison between the calculations and the experimental results, the collection efficiency η, determined by the spatial radiation pattern and the $N.A.$ of the microscope objective has to be taken into consideration as well. Thus, we can evaluate the relative PL intensity in the dimer by solely considering the field intensity and the collection efficiency as

$$I_{PL}(\omega) \propto \eta * \int_V |\vec{E}_0(\omega_0, \vec{r})|^2 * |\vec{E}_{em}(\omega, \vec{r})|^2 dV \qquad (6.2)$$

where $\vec{E}_0(\omega_0, \vec{r})$ is the electric field at the excitation frequency ω_0, $\vec{E}_{em}(\omega, \vec{r})$ is the electric field at the emission frequency ω, and V is the integration volume. Using the finite-difference time domain method, one can calculate the electric field terms in Eq. (6.2) and subsequently calculate the relative PL emission intensity. Note that this calculation model is only applicable to plasmon radiation dominated PL emission processes based on the aforementioned assumptions.

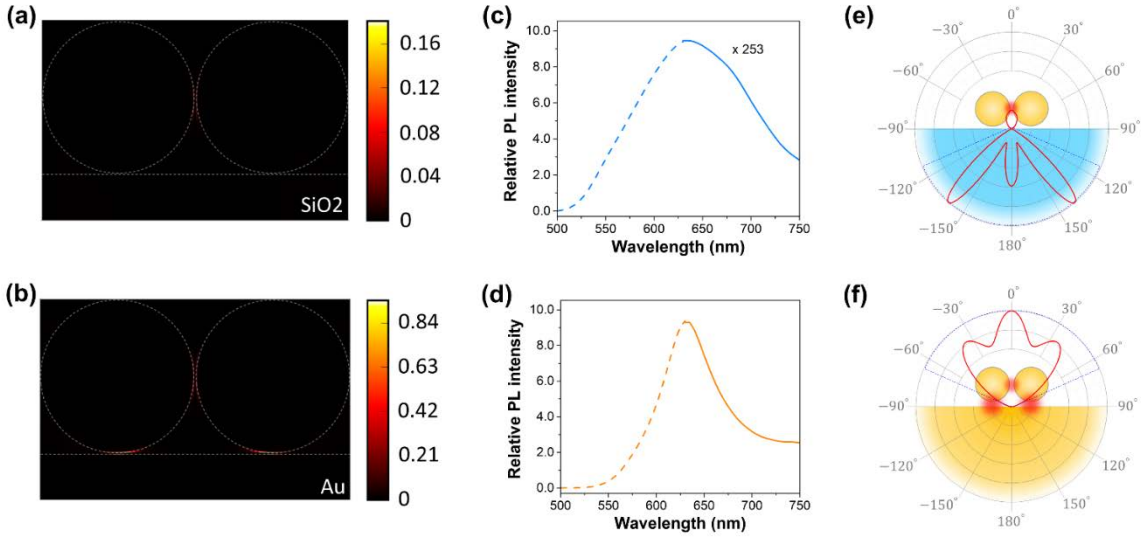

Figure 6.3 (a, b) Calculated PL intensity distribution (cross-sectional view) at the emission peak 650 nm for the nanosphere dimers on silica (b) and film (b), respectively. The color bars represent the calculated PL intensity by Eq. (4). (c, d) Calculated photoluminescence spectra with relative intensity for the dimers on silica (c) and gold film (d). (e, f) Calculated PL emission pattern at 650 nm. The blue dashed sectors correspond to the collection angles defined by the objective NA of 0.9.

As shown in Figure 6.3a and b, the calculated PL intensity distribution at the peak emission wavelength 650 nm reveals that the PL emission of the silica-supported dimer mainly originates from the particle-particle gap while that of the gold film-coupled dimer comes from both the sphere-sphere gap and the sphere-film ones. One can observe that the PL intensity at the sphere-film gaps is substantially larger than that of the sphere-sphere gap in

the film-coupled dimer and, on the other hand, the latter is much stronger than that of the sphere-sphere gap in the silica-supported dimer. This observation is very counterintuitive, considering the fact that the incidence polarization is aligned along the dimer axis. Since the sources of PL emissions are highly confined within the nanoscale gaps in both dimers, we evaluate their radiation directionalities by simulating the far-field radiation patterns of the two systems with an emitter-cavity model (see Figure A2). The calculation results shown in Figure 6.3e-f demonstrate that the emission patterns for both systems are similar to their plasmonic scattering patterns, which again supports the radiative decay of plasmons to be the origin of the observed PL emissions. By integrating the radiation intensity over the collection angle of the objective in the silica substrate side as in Figure 6.3e and in the upper-half space in Figure 6.3f, an emission efficiency of 84% for the silica-supported dimer and 87% for the gold film-coupled dimer are obtained, respectively, with which the relative PL intensity spectra can be calculated for comparison with the wavelength-dependent experimental results. Surprisingly, the calculation results shown in Figure 6.3c-d well reproduce the measured PL spectral profile for both dimers. Additionally, the results also give a peak enhancement factor of ~ 253 for the film-coupled dimer compared to the silica-supported one, showing excellent agreement with experiment (~ 200 times). The negligible discrepancy may be resulted by the effect of nonradiative plasmon decays being absent from the above discussions on mechanism of PL emission[145]. or other experimental flaws, which are hard to name.

In addition, we also calculate the relative PL intensity spectra over specific integrating domains in the gold film-coupled and silica-supported dimers and present the results in Figure 6.4. Note that a modified similar approach was adopted to distinguish plasmon-enhanced nonlinear emission contribution from a discrete domain of an entire hybrid plasmonic

system[201,202]. Figure 6.4b compares the relative PL intensity spectra calculated for the H-gap, V-gap and the entire silica-supported dimer, revealing that the total PL emission mainly comes from the H-gap region. In remarkable contrast, Figure 6.4c shows that the V-gap has a dominant contribution to the total PL intensity of the film-coupled dimer though the incidence polarization is set along the dimer axis which would preferentially excite the H-gap plasmon resonance. This is consistent with the above-discussed metal substrate mediated dipolar-quadrupolar plasmon hybridization mechanism, through which the bright dipolar plasmon resonance (horizontal bonding) effectively harvests the incident light energy, transfers the energy to the dark quadrupolar resonance (vertical bonding) through near-field coupling, and significantly amplifies the energy density in the vertical gap regions, enabling efficient photoluminescence. Furthermore, Figure 6.4d shows that the PL intensity of the underlying gold slab overwhelmingly exceeds that of the nanosphere dimer by a factor of more than 20, which could be attributed to the denser charge accumulation in the flat surface of the gold film than the curved surface of the nanospheres, leading to higher field intensities in the gold film domain.

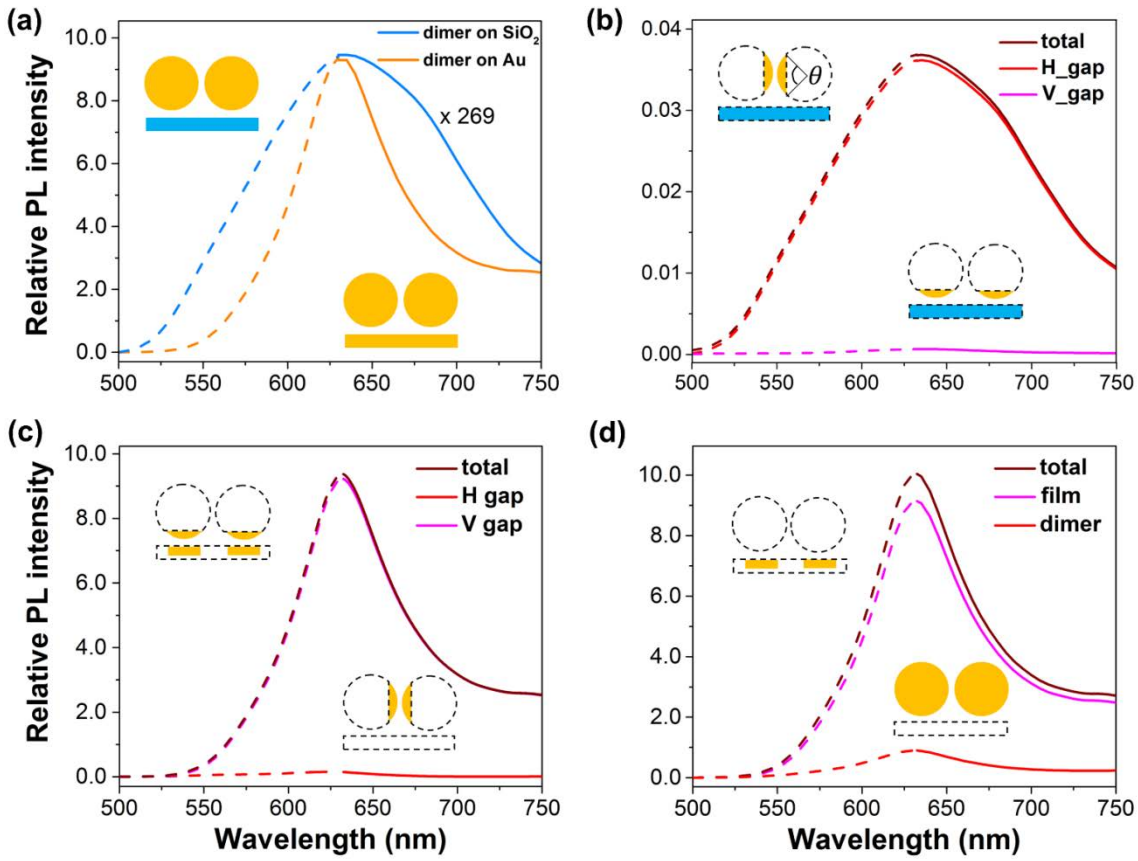

Figure 6.4 Relative photoluminescence intensity calculated for different integrating domains: (a) the entire film-coupled dimer (orange) and the silica-supported dimer (light blue), (b, c) the horizontal (red) and vertical (purple) gap domains in (b) the silica-supported dimer and (c) the film-coupled dimer, and (d) the two nanospheres (red) and the underlying film (purple) of the film-coupled dimer. The corresponding integrating domains are indicated in yellow as shown in the insets. The apex angle θ, defining the domain size in (b, c) is 90^{o}. The size of each slab in (d) is $12\times12\times6$ nm^3.

6.4 Conclusion

In summary, we have performed the photoluminescence spectroscopy over both the single nanosphere dimer on silica and gold film. Upon near-resonant excitation of the hybridized dipole-quadrupole plasmon resonance, the film-coupled dimer shows a photoluminescence intensity enhancement up to ~200 times yet with a much narrower emission linewidth in comparison with the silica-supported dimer. The high polarizations as well as the similarities between the PL emission and plasmon scattering spectra of both the

glass supported and gold film coupled dimer suggest the radiative plasmon decay dominate the photoluminescence emission. Moreover, the relative PL intensity calculated over different volume domains in the two dimers reveals that the contribution from the vertical sphere-film gap junctions dominates the total PL emission of the entire system. These findings demonstrate that the film-coupled metal nanosphere dimer can provide a nanoscale cavity with both ultrasmall mode volume and ultrahigh quality factor, offering a promising platform for various plasmon-enhanced spectroscopy applications such as SERS[175], nonlinear plasmonic sensing[203], and plasmon-molecule strong coupling[72].

Chapter 7 Gap plasmon enhanced nonlinear optical emission from upright plasmonic molecules for longitudinal field mapping

Placing a nanoparticle near metal surface can define a plasmonic molecule with a strong vertically aligned dipole moment. This kind of molecules preferentially respond to the longitudinal filed component of an incident excitation, suggesting the metal film-coupled nanoparticles a potential probe for longitudinal field sensing. To explore this potential, in this chapter we perform the nonlinear optical spectroscopy of the single metal film-coupled nanoparticles. In section 7.1, a continuous tunability of the gap plasmon resonance within the Vis-NIR band is demonstrated through the size control over the gold film-coupled nanoparticles, which allows for a resonant excitation for enhanced nonlinear optical responses with the readily accessible Ti:sapphire femtosecond lasers. Then in section 7.2, the nonlinear optical emissions of the metal nanoparticles on film are experimentally investigated, in which a significant nonlinear optical emission enhancement is demonstrated for the metal film-coupled nanoparticles compared to their counterparts on silica substrate. Particularly, the second harmonic generation shows a nonlinear conversion coefficient $> 1.05\times10^{-8}/W$, which means a second harmonic photon yield as high as $\sim1.49\times10^{9}$. More intriguingly, a two-lobe shaped emission pattern for each nanoparticle on film is observed. To account for these experimental findings, the calculation of field intensity distributions at the focal plane are performed based on the vector diffraction theory as detailed in section 7.3. Excellent agreements between the calculation results and the experimental observations for both linearly and circularly polarized excitation cases are demonstrated, unambiguously confirming that the

excitation of the gap plasmon resonance of the metal film coupled nanoparticles dominantly contributes to the enhanced nonlinear optical emissions. This way the gap plasmon resonance enhanced nonlinear optical emissions enables the vertically aligned plasmonic molecule a nanoscale and sensitive probe for longitudinal field mapping.

7.1 Tunable dipolar gap plasmon resonance through particle size control

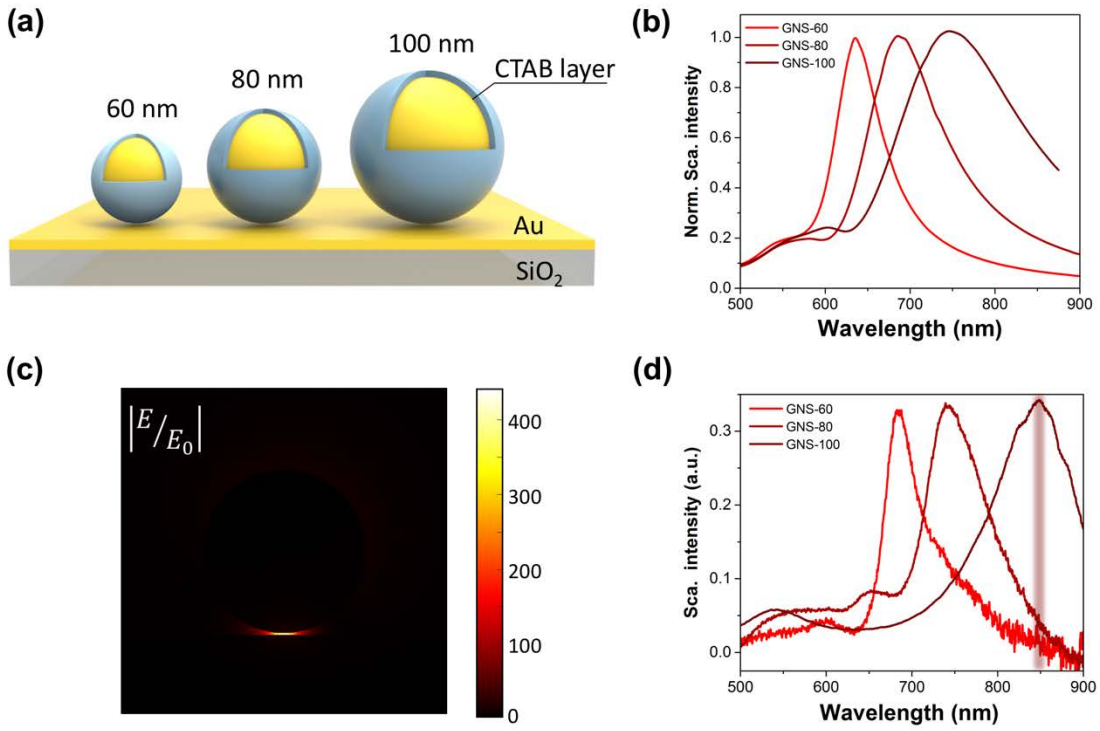

Figure 7.1. (a) Schematic of the gold-film coupled nanospheres of different sizes: 60nm,80nm and 100nm. (b) Calculated scattering spectrum of the particles as in(a), Note the CTAB shell is not considered in the simulation for simplification. (c) Calculated near-field intensity distributions of the 100 nm gold nanoparticles on film at the resonance wavelength. (d) Measured scattering spectra corresponding to the ones in (b).

The gold film coupled nanoparticles used here are schematically depicted in Figure 7.1a, which are fabricated in the same way as in our previous studies[204]. The coating layer CTAB

acts as the spacer to separate the particle from the underlying gold film with ~1 nm distance. To realize emission enhancement in nonlinear optical spectroscopy, the gap plasmon resonances of the film-coupled nanoparticles need to be efficiently excited, which means the gap plasmon resonance wavelength is required to be tuned into the emission band of the generally available Ti: sapphire femtosecond laser, say $700-1000$ nm. Instead of controlling the spacer thickness to adjust the plasmon resonance wavelengths as reported elsewhere, here we simply change the particle size attempting to shift the gap plasmon resonance into the near-infrared region. Based on electromagnetic simulation results, it is found that increasing the particle diameter indeed leads to the red shifts of the gap plasmon resonance as shown in Figure 7.1b. Thus, the nanostructure of the gold film-coupled nanoparticles with different particles size are fabricated. To determine the actual gap plasmon resonance positons, the scattering spectra of them are measured (Figure 7.1d) in the single particle level. As can been seen from Figure 7.1b and d, all of the measured spectra show a redshift in their resonance peaks compared to the corresponding simulated ones. This is largely due to the removal of the thin CTAB layer in the simulation configuration, which otherwise would make the simulation substantially heavy and even leads to convergence failure. Fortunately, the gold nanoparticles of 100 nm diameter coupled to the gold film are found to have a gap plasmon resonance located in the near-infrared band (~850 nm) and more than two orders of filed intensity enhancement can be achieved in the gap region upon resonant excitation according to the simulation results (Figure 7.1c). Subsequently, the gold nanoparticles of 100 nm diameter coupled to the gold film will be studied in the following nonlinear optical spectroscopy experiments.

7.2 Gap plasmon resonance enhanced nonlinear optical emission

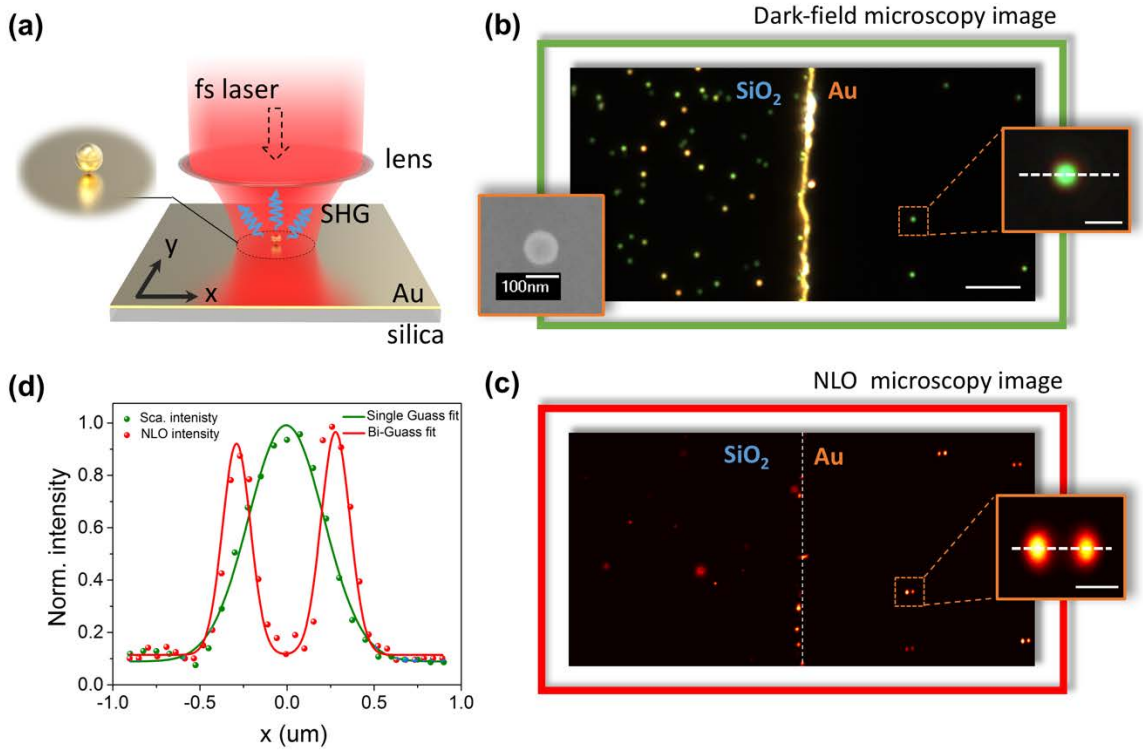

Figure 7.2 (a) Simplified experimental configuration for the nonlinear optical spectroscopy. (b) Dark field image of gold nanoparticles which are dispersed partly on gold film (left region) and silica substrate (right region). The boundary of different substrate is clearly visible. The geometric detail of the red square box enclosed nanoparticle is showed in the inset. (c) The nonlinear optical image of the gold nanoparticles of the same area as in (b). For clarity, the emission pattern of one nanoparticles on the gold film is refined and enlarged as in the inset. The collection band for imaging is 400-750 nm. The scalar bars are 5 μm and 1 μm in the main image and inset, respectively. (d) The intensity profiles of the scattering pattern marked in (b) and nonlinear optical emission pattern for the same one.

The simplified experimental configuration is schematically showed in figure 7.2a. A linear polarized laser beam is tightly focused onto the nanoparticles. The possible nonlinear optical emission, such as second harmonic generation or/and two-photon luminescence, *etc.*, will be collected by the same objective and guided to the spectrometer system for spectral

analysis and nonlinear optical imaging. Particularly, the imaging is performed in a confocal configuration in which the focused laser beam scan across the samples (for details see Figure 3.9). The main images in Figure 7.2b and c show the dark field (b) and nonlinear emission (c) image captured over the same sample area. For a solid comparison of the distinguished optical response of the nanoparticles on gold film and silica substrate, the sample is deliberately processed in a special manner so that particles on both substrates can be shot simultaneously. It can be clearly seen from Figure 7.2b that the particle density on the silica substrate (upper-right region) is unambiguously larger than that on the gold film, which can be attributed to the reinforced bonding through electrostatic attraction between the gold particles and silica surface and thus a higher particle possibility of immobilization[205]. Counterintuitively, the each particle on the gold film also appears as a green solid spot pattern as that on the glass side. Actually, these green solid patterns correspond to the transversely oscillating dipolar mode (with resonances at ~ 550 nm) of the single nanoparticles. The gap plasmon resonances (with resonances at ~ 850 nm) of the gold film-coupled particles, though possessing the strongest scattering intensity, falls into the near-infrared band as already shown in Figure 7.1d and cannot be efficiently detected by the silicon CCD camera. More intriguingly, in the nonlinear optical image shot with a collection band $400 - 750$ nm, while the particles in the silica region are all invisible, their counterparts in the gold substrate area are all lightened again by the focused femtosecond laser pulses. This emission contrast undeniably suggests a large nonlinear optical emission enhancement for the gold nanoparticles when coupled to metal film. Particularly, all of the visible particles appear as a two-lobes shaped pattern individually, which are obviously different from their appearances in the scattering images as shown in Figure 7.2b. These distinctive appearance features of the metal film-coupled nanoparticles in

the dark field (Figure 7.2b) and nonlinear optical image (Figure 7.2c) can be more clearly distinguished by the comparison of their intensity profiles as presented in Figure 7.2d, in which a bi-Gaussian-peaks profile of the individual particle on gold film in the nonlinear optical image can be unambiguously identified from the single-Gaussian intensity distribution observed in the linear optical image.

To identify the origins of the enhanced nonlinear optical emission from gold nanoparticles brought in close proximity to a metal substrate, the emission spectrum from single particle is measured and presented in Figure 7.3a. As can be seen, a narrow emission peak with wavelength exactly poisoned at half of the excitation (~ 425 nm) can be identified from a broad emission background whose band centers at ~ 550nm. Their emission intensity dependencies on the excitation power, as plotted in a log-log manner in Figure 7.3b, both present a linear correlation with slope ~ 2.0, confirming the two emission bands correspond to the second harmonic generation and two-photon luminescence, respectively. To probe the enhancement mechanisms of the SHG and TPL, the nonlinear optical images in both the SHG band ($400 - 450$ nm) and the TPL band ($500 - 600$ nm) are captured as shown in Figure 7.3c. Due to the narrower emission band, the SHG image takes on a lower intensity compared to that of the TPL emission. However, they share the same emission pattern in both images, which implies a similar emission enhancement mechanism behind both of them. Details will be addressed in the following.

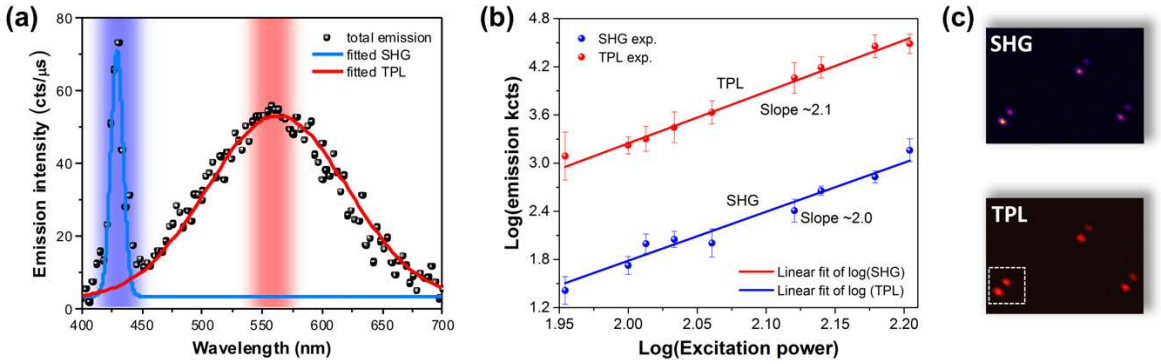

Figure 7.3 (a) The nonlinear optical emission spectra of the single nanoparticles on gold film. (b) The power dependence of the emission intensity for TPL and SHG integrated within spectral bands specified in (a). (c) The nonlinear optical images of nanoparticles in the same area obtained in different spectral bands as that distinguished in (a).

In this nonlinear optical spectroscopy experiment, the focused femtosecond laser illuminates the singled nanoparticles in a beam scanning mode (see Figure 3.10). In details, a linearly polarized laser beam, upon focused by an objective, will produce other two orthogonal field components at the focal plane as indicated in the inset in Figure 7.4a. Particularly, with increase in the numerical aperture of the objective used, the intensity of the longitudinal component, that is absent in the laser beam before focused, will gradually increase and can be up to 30% of the total power when $\mathrm{NA} = 0.9$. Though the field component of the original polarization (transversely polarized) still dominates the total power, the effects of the longitudinal component in sensitive nonlinear spectroscopy applications, cannot be ignored. For the metal film-coupled nanoparticles, the gap plasmon modes respond preferentially to the longitudinal polarization component of the light incidence and the large field enhancement upon resonant excitation of the gap plasmons by the femtosecond lasers are believed to be responsible for the nonlinear optical emissions. To confirm this, we will evaluate the excitation polarization dependent nonlinear emission intensities. Since switching

in between the pure transverse and longitudinal polarizations in experiment is difficult, the polarization control is performed in the nonlinear simulation frame. Take the second harmonic generation for example, the near field distribution at SH wavelength (*ie.*,425 nm) is calculated based on a perturbative approach in the nonlinear optical regime[108]. As indicated in Figure 7.4(b-c), the excitation is either p-polarized (Figure 7.4b, polarization in the incidence plane) or s-polarized (Figure 7.4c, polarization out of incidence plane). For p-polarized excitation, the transverse and the vertical (along the surface normal) polarization components possess the same intensities because the incidence angle is 45^0. In this excitation configuration, strong SH intensities are observed in the nanoparticle-film region. When the excitation is switched to p-polarization, the intensities turn to be extremely weak. This sharp contrast in the SH intensity indicates that the nonlinear optical process is driven by the longitudinal field component. Thus, we can infer that in experiment, even though the transversely polarization component dominates the total laser power, they do not contribute to the enhanced nonlinear optical emission. As will be seen later, the nonlinear optical emission patterns of single film-coupled nanoparticles just provide the evidence for this inference.

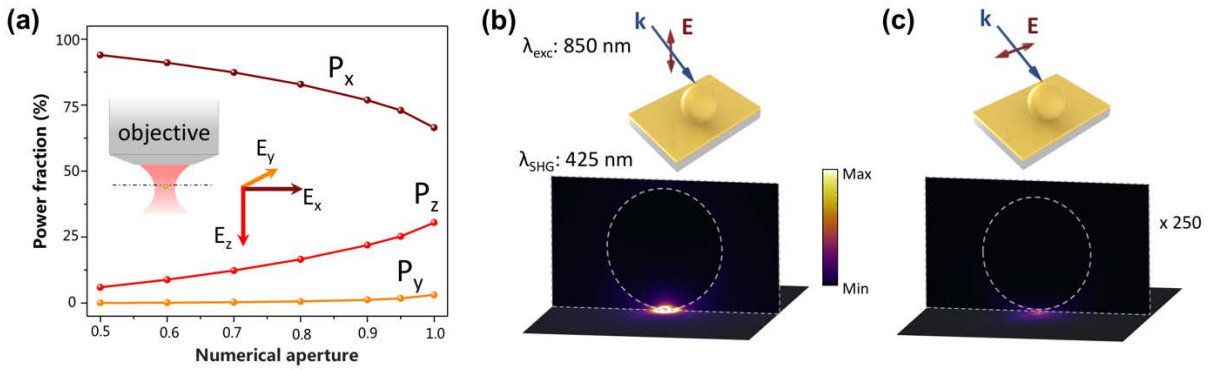

Figure 7.4 (a) Calculated power dependences of the three orthogonal field components on the objective numerical aperture. The incident laser beam is $x-$ polarized before focused. (b) The near field intensity

distribution at the SH frequency upon p-polarized excitation. (c) The near field intensity distribution at the SH frequency upon s-polarized excitation.

7.3 Nanoparticles coupled to a metal film as a sensitive field probe for longitudinal field mapping

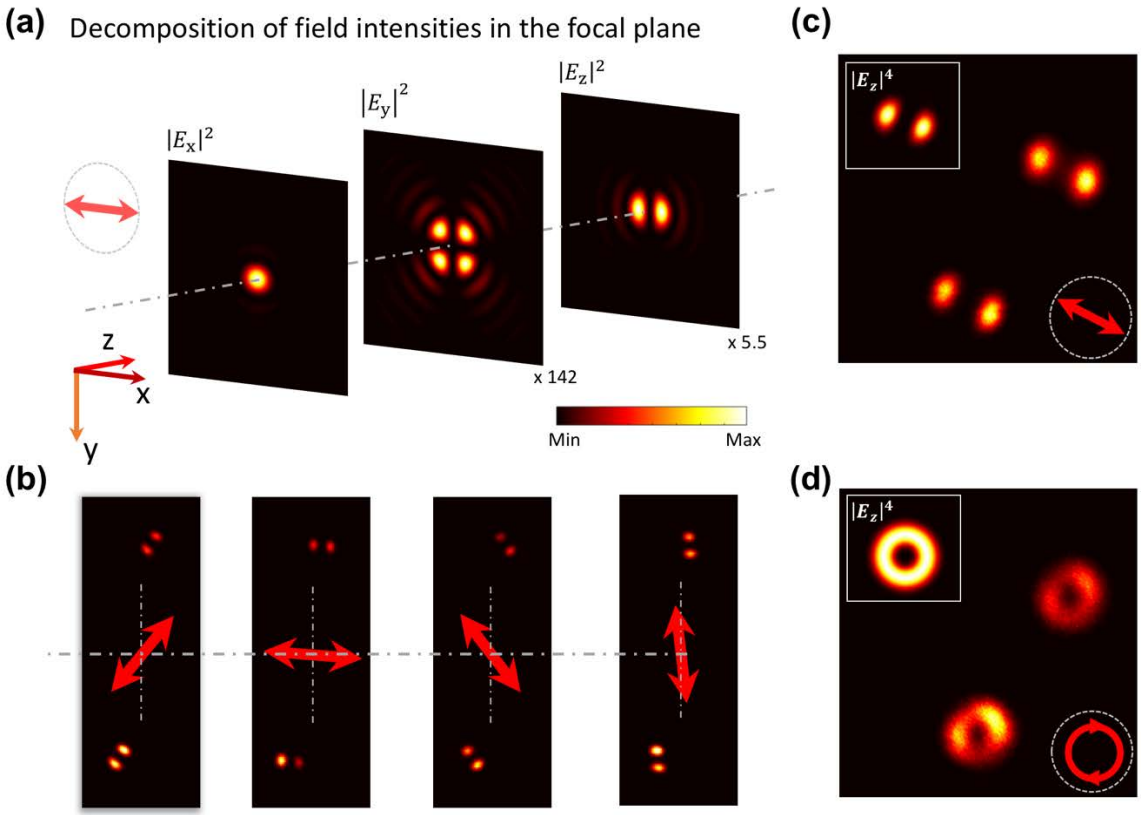

Figure 7.4 (a) Decomposition of filed intensities in the focal plane. Before focused, the incident beam is linearly polarized along x. The numerical aperture of the lens used in calculation is 0.95. (b) Excitation polarization dependent SH emission patterns of single gold film-coupled nanoparticles. The incidence is linearly polarized. (c-d) comparison between the SH emission patterns of nanoparticles coupled to film upon excitation of different polarization states. (c) for linear polarization and (d) for circular polarization.

Back to experiment, the laser-scanning configuration is functionally equal to a stage scanning one in which a single particle driven by the motorized stage moves around in the

immobilized illumination beam (see Figure7.2a). For clarity, we will adopt the stage scanning configuration in subsequent analysis. With the diffraction theory, we calculate the transverse and longitudinal field intensities at the focal plane of a tightly focused laser beam with linear polarization (see details of the calculation methods[206,207] in the appendices section). Figure 7.4a shows the calculation results. As can be seen, while profile of the strongest transverse field x polarization component, appears as a solid spot, the intensity distribution of the longitudinal field component is featured with two strong intensity lobs symmetrically aligned along the incident polarization of unfocused beam. This two-lobes shaped field pattern closely resembles to the nonlinear optical emission patterns of single gold film-coupled nanoparticles except for the subtle intensity ribbons in the calculated field distribution. Actually, the nonlinear optical emission intensities of both SHG and TPL exhibit a quadratic dependence on the excitation intensity as already demonstrated in Figure 7.3b. Hence, the fourth order powered intensity distribution profiles of fundamental field are more straightforwardly correlated with the nonlinear optical emission pattern (Figure 7.4c). To be convincing, we continuously rotate the direction of the incidence linear polarization. It is found the orientations of SH emissions of single nanoparticles rotate synchronously. In this way, the metal film coupled nanoparticles act as a field probe which can be utilized to map the longitudinal field distribution of focused lasers. As one more demonstration, we alter the incidence light to be circular polarized. The observed nonlinear optical emission pattern of each film-coupled particle becomes like a hollow disk, showing good agreement with the calculation results (Figure 7.4d).

7.4 Revealing the origins behind the large SHG enhancement

To evaluate the SH conversion efficiency with this tightly coupled plasmonic structure, we have performed the SH emission power measurements over 271 nanoparticles on gold film. Details of the method can be found in the appendix section. Based on the statistic measurements, we obtain an average SHG conversion efficient $> 1.05\times10^{-8}\,W^{-1}$ for individual film-coupled nanoparticles, which means a second harmonic photons yield as high as $\sim1.49\times10^{9}$ photons per second.

In probing the mechanism of the large SH enhancement of this compact nano-resonator, the contributions from both the excitation and emission enhancements have to be considered, respectively. Based on a phenomenological model of nonlinear optics[208], the SHG related second-order nonlinear polarization $P_{2\omega}^{(2)}$ for the plasmonic resonator takes the following form:

$$P_{2\omega}^{(2)} \propto \chi^{(2)}(-2\omega;\omega,\omega)L_{2\omega}[L_{\omega}E_0]^2 \quad (1)$$

where L_{ω} and $L_{2\omega}$ are the excitation and emission field enhancement factors, respectively. $\chi^{(2)}(-2\omega;\omega,\omega)$ is the material susceptibility determining the second-order nonlinear response. Obviously, while the nonlinear polarization intensity is linearly proportional to the emission enhancement factor $L_{2\omega}$, it shows a quadratic relationship with the excitation enhancement factor L_{ω}. This distinctive enhancement dependence of the SH response suggests its higher sensitivity to the excitation component, which can be more evident by evaluating the SH intensity variation as

$$\delta I_{2\omega} \propto 2\omega L_{2\omega}\,\Delta\,L_{2\omega} + 4\omega L_{\omega}^{3}\,\Delta\,L_{\omega} \quad (7.2)$$

Here the first term on the right hand of equation (7.2) defines the contribution from emission enhancement, and the second term corresponds to the excitation enhancement. Since the excitation component dominates the nonlinear optical response, the strong SH from the metal film-coupled nanoparticles can be reasonable considering the huge excitation field enhancement within the ultrasmall particle-film cavity. As indicated in Fig.1c, the peak field strength enhancement within the nanocavity reaches ~500. Because of $I_{SH} \propto L_{\omega}^{4} E_{0}^{4}$, a peak SHG enhancement factor as high as 6.25×10^{10} can be anticipated. Though recently reported plasmonic nanostructures designed for enhanced nonlinear optical emissions (SHG/THG) prefer to the double-resonant (DR) configurations, the exemplified structures, until now, are limited to several complex entities.[209,210] Moreover, the DR nano-antennas fabricated with up-bottom methods usually suffer from relatively low nonlinear excitation rate (excitation contributed peak SHG enhancement factor typically $< 10^{8}$)[209] compared to the deep nanoscale ($\sim$1nm) particle-film cavity, offering the metal film-coupled nanoparticles a good chance to surpass the DR antennas in SHG enhancement.

The charge distributions of the nanoparticle on film at the SH wavelength are also calculated to reveal the nature of the SH emissions. Figure 5a shows both the real and imaginary parts of the complex charge distributions. While the real part exhibits an electric quadrupole feature in the near-field, the imaginary part shows definitely an electric dipole character. This distinct charge phase characters suggest modes hybridization occurred at the SH wavelength.[211] Though a clear description of its role on SHG emission is still lacking, it's believed that, through modes hybridization, the dark quadrupole component induced SHG in the near field can partly transfer its energy to the radiative dipole mode and, thus, radiate into the far field space.[212] To address this effect in the gold nanoparticles tightly coupled to film,

we seek to track the dipolar SH emission characters in the far field zone. We achieve this by numerically performing the near-to-far field transformation.[213] A pure dipolar character of the second harmonic emission can be identified from the far field (Figure 7.5b). This far-field feature is dramatically distinct from the doubly-resonant plasmonic antennas in which the SH emission are typically of a quadrupole type due to modes hybridization.[212] Therefore, the SH emission efficiency of doubly-resonant plasmonic antennas are not necessarily advance over the nonresonant dipolar SH emission of gold film-coupled nanoparticles. Though it's hard to evaluate, the emission enhancement contribution to the total SHG enhancement in the gold film-coupled nanoparticles can be considerable.

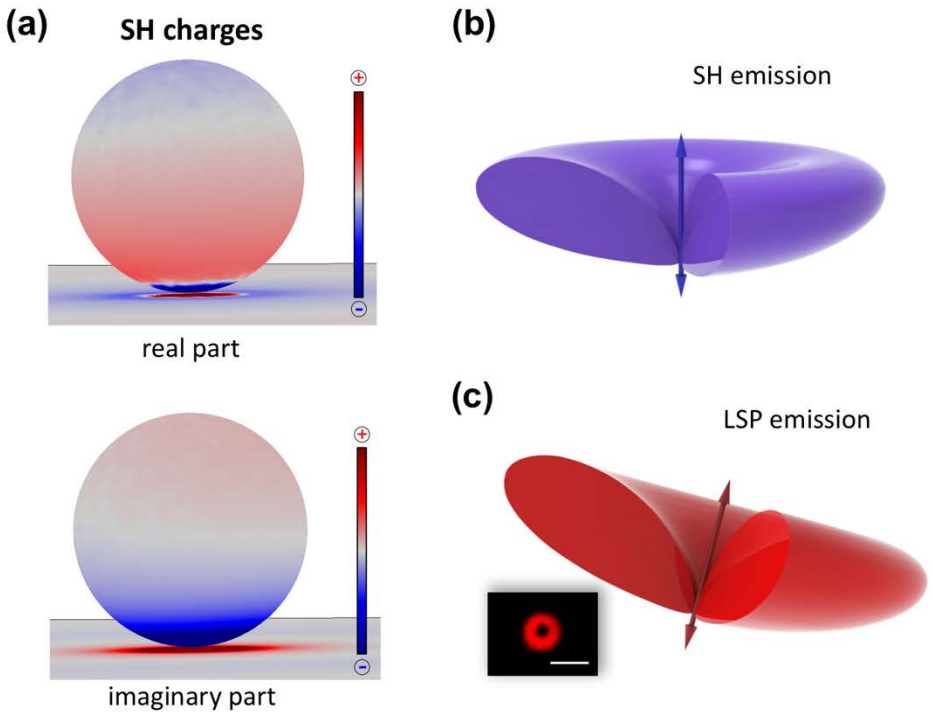

Figure 7.5 (a) Simulated SH (wavelength at 425 nm) charge distributions. (b) Calculated SH emission pattern. (c) Calculated emission pattern of the localized surface plasmon at the excitation wavelength (850 nm).

7.5 Conclusion

In conclusion, we have demonstrated an upright plasmon molecule by placing a gold nanoparticle near the gold film. The strong vertically aligned dipolar plasmon resonance of the molecule can be continuously tuned within the VIS-NIR band through simple control over the particle size. Upon resonant excitation, the metal film-coupled nanoparticles show significant enhancement in nonlinear optical emission (SHG and TPL) compared to their counterparts on the glass substrate. Numerical simulations based on perturbative approach have been performed and the near -field intensity distributions at SH frequency revealed a highly confined nonlinear light source in the particle-film gap junction, implying the dipolar gap plasmon resonance is responsible for the emission enhancement. Subsequent calculations results based on the vector diffraction theory further confirm the dominant contribution of the longitudinal component to the nonlinear optical emission, enabling the metal film-coupled nanoparticles an ultrasmall and sensitive field probe for longitudinal field mapping which is fundamentally important for nanoscale light-matter interactions. Moreover, the measured nonlinear conversion coefficient for second harmonic generation of single gold film-coupled nanoparticles is as high as $> 1.05\times10^{-8}/W$. Nonlinear simulation results reveal this large SHG enhancement originates from both the ultra-strong excitation rate near the nanoparticle-film junction and the emissive dipolar character at SH wavelength.

Chapter 8 Conclusion and outlook

In this thesis, I presented our studies on the linear and nonlinear optical properties of metal film-coupled nanoparticles with particular focus casted on the multi-nanoparticle coupled to the metal film.

Within the linear optical frame, we carried on the polarization resolved dark field spectroscopy experiment to explore the rich gap plasmon modes of both the gold film coupled nanoparticle monomers and dimers. It has been found the gold monomers, when placed near the metal film, can result in a dipolar gap plasmon resonance in the near-infrared wavelength band through the particle-film coupling. This gap dipolar mode shows a distinctive dough-nut shaped radiation pattern as revealed by the developed color-decoding technique (or quasi multi-spectral imaging method). In the meantime, the transverse particle plasmon mode, though electrically screened by the underlying metal film, does remain and appears as a bright solid PSF spot in the radiation field, which showed excellent agreements with the full wave simulation results performed based on FEM method. More intriguing scenario occurred for the dimer case: when a single nanoparticle is coupled to another one on glass. This would lead to a bright bonding dipolar plasmon mode with broad resonance linewidth. However, the linewidth can be significantly narrowed by a factor of ~4.9 by replacing the dielectric substrate with a gold film. While the narrow effect also slightly holds for the monomer coupled gold film, this pronounced linewidth shrinking for the dimer must imply more rich physics involved.

To uncover the physical origin of the narrow plasmon mode of dimer coupled to gold film, we resorted to the plasmon hybridization theory proposed by Peter Norlander etc. Then

with multipole expansion method, we successfully extracted a bonding dipolar mode formed by the particle-particle coupling, and a quadrupole mode formed by the transverse dipolar bonding mediated by the metal film. It turns out that the plasmon hybridization between the bonding dipolar mode and the quadrupole mode largely suppresses the radiative loss of the dipolar mode and thus results in the longer life of the hybridized mode as manifested in the shrinking modes linewidth. Additionally, this narrow effect is also revisited with transformation optics theory. The near field distributions of the transformed system suggest a substantially increased energy concentration in the near field domain and thus the resultant reduction in radiation loss leads to the significant plasmon linewidth narrowing.

In light of the energy transfer from the far field to the near field regime as suggested by both the plasmon hybridization model and the transformation optical theory, we anticipated this effect can be used to significantly enhance the light-matter interactions for some spectroscopy applications. As a demonstration, we performed the photoluminescence spectroscopy of the single nanoparticle dimer coupled to metal film. It has been found the photoluminescence intensity of the dimer on gold film is ~ 200 times stronger than that of its counterpart on glass substrate. Particularly, the spectral characteristic of the photoluminescence for dimers on both substrates fully resemble that of their scattering spectra in peak positions and linewidth. These similarities imply the plasmon emission is the origin of the photoluminescence enhancement in both nanostructures, which is further confirmed by the good agreement between the experiments and calculation results.

As for the nonlinear optics aspect, we perform the multi-photon spectroscopy of the gold film-coupled nanoparticles. The available femtosecond laser system equipped to the spectroscopy system comes with a tunable lasing wavelength within $\sim 700 - 1100$ nm, while

the work wavelength band of the light detectors in the detection module is restricted to $\sim 400-700$ nm. For readily charactering the general nonlinear optical emission, such as the second harmonic generation, two-photon luminescence, the effective excitation wavelength is required to be at least slightly above double of the detector's lower limit, i.e. ~ 800 nm. Therefore, the available excitation wavelength band is $800-1100$ nm, and it can be anticipated when the plasmon resonance falls into this band, resonance enhanced nonlinear optical emission can be achieved. For this reason, we demonstrated a continuous tunability of the plasmon resonance wavelength though simply controlling over the particle size, and finally, the 100 nm particles coupled the metal film, with a gap plasmon resonance ~ 850 nm are chosen for the nonlinear optical spectroscopy. It is found the gold nanoparticles demonstrate large nonlinear optical emission (of both SHG and TPL) enhancement compared to their counterparts on the glass substrate. More strikingly, each of the emitting nanoparticles appears as a two-lobs shaped pattern, which is distinctively different from its appearance in the dark field image. Considering the emission enhancement may arise from the excitation of the gap plasmon resonance peculiar to the nanoparticles on gold film, the two-lobe shaped pattern may correspond to the longitudinal field component responsible for gap plasmon activation. To confirm this, we calculate the field intensity distributions of the tightly focused beam with a linear polarization at the focal plane. It is found that the pattern of the calculated longitudinal field distribution well resembles to the observed emission pattern of single nanoparticle on film, which also holds for the circular polarization excitation carried subsequently, enabling the metal film coupled nanoparticles an ultrasmall and sensitive probe for longitudinal field mapping.

Throughout this thesis, the metal film-coupled nanoparticles have been demonstrated as a promising plasmonic nano-platform which exhibits distinctive plasmonic responses and possesses a nanoscale gap cavity hosting for versatile spectroscopy enhancements. In view of the rich plasmon interactions, together with the easiness in fabrication as well as the readily loading of active optoelectronic materials into the hot spots, continuous studies on the metal film-coupled nanostructures can be expected in future to trigger a series of breakthroughs in nanophotonic research and applications.

Appendices

Identify the nanoparticle dimers on gold film with dark field spectroscopy

Gold nanosphere dimers can readily be identified with the aid of a dark-field microscope. As can be seen in Figure A1, the nanosphere monomers show clear green colors, while the nanoclusters appear as bright spots. In particular, the nanosphere dimers, whose constitution is confirmed afterwards in the SEM image, show clear red colors in the dark-field image. Based on these color differences of the nanoparticles in the dark-field image, we are able to optically distinguish the gold nanosphere dimers from the monomers and measure the optical response of the nanosphere dimers before the SEM characterization. Thus, potential modifications to the optical response of the nanoparticles by the e-beam irradiation in a conventional SEM-first manner are avoided.

Actually, the nanoparticles we selected for scattering measurement are all spherical-like, and no severe aberrations from a sphere shape can be observed in the SEM images. Still, tiny structure features, like sharp surface corners, roughness, overall size difference cannot be excluded and will affect the optical properties. Previous studies[145,214] have shown that, compared to the ultra-smooth spherical nanoparticles, the spherical-like nanoparticles inherit the same plasmonic modes yet with shifted plasmon resonance positions. Another study[215] also demonstrates the surface roughness or local environmental variations in the particle-film coupling system would not alter the plasmonic modes and only shift the plasmon resonance peak. Therefore, the aberration from perfectly spherical shape wouldn't intrinsically alter the

plasmonic modes as showed in Figure A1b.

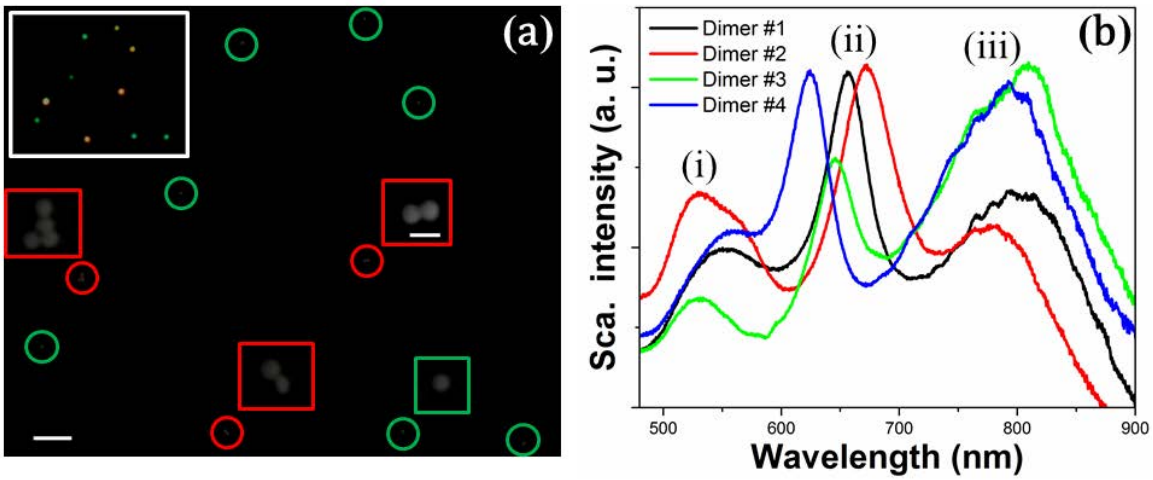

Figure A1. (a) Pattern matched SEM image and dark-field image (inset, upper-left corner) of gold nanoparticles positioned on a 45-nm-thick gold film. The enlarged SEM image of each representative particle is presented nearby as insets. The scale bar is 1 μm in the large image and 200 nm in the enlarged image. (b) Scattering spectra measured over several nanosphere dimers on gold film.

Simulation model of far-field radiation and photoluminescence emission patterns for both silica and gold supported dimers

To simulate the far field radiation patterns of both dimer systems, the monitors used to record the radiative fields have to be very large to cover as much the radiation fields as possible and also be far enough from the surface of the gold film to avoid collecting the field of the surface waves that would not contribute to the far-field radiation. Considering the huge amount of memories required by finite-element method based simulation codes such as COMSOL, here we adopt the finite-difference time domain method to calculate the far-field scattering and emission distribution of the two systems. As depicted in Figure S2, the lateral size of the monitors in the upper and lower half-space are set to be 4800 x 4800 nm^2, and

symmetry planes are set in the PML boundaries to further reduce the computing burden.

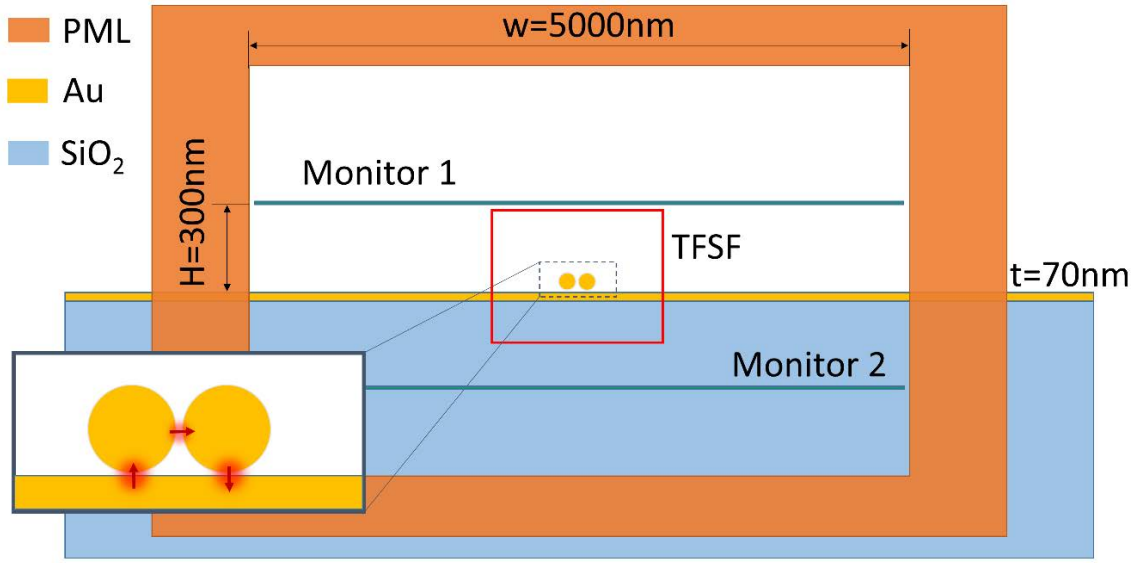

Figure A2. Schematic of an FDTD Solution (Lumerical Inc.) model for calculating the far-field radiation and photoluminescence emission patterns of the gold film-supported dimers. The same model is used for the silica-supported dimer by simply replacing the gold film layer with silica. The lateral width of the calculation domain is 5 μm. PML: perfect match layer; TFSF: total field and scattering field source. When calculating the far-field radiation pattern at the scattering peak wavelengths of the two systems, the TFSF source is launched; When calculating the photoluminescence emission patterns, the dipoles sources as shown in the inset are activated.

Scattering spectra of a single gold film-coupled dimer taken before and after photoluminescence measurement

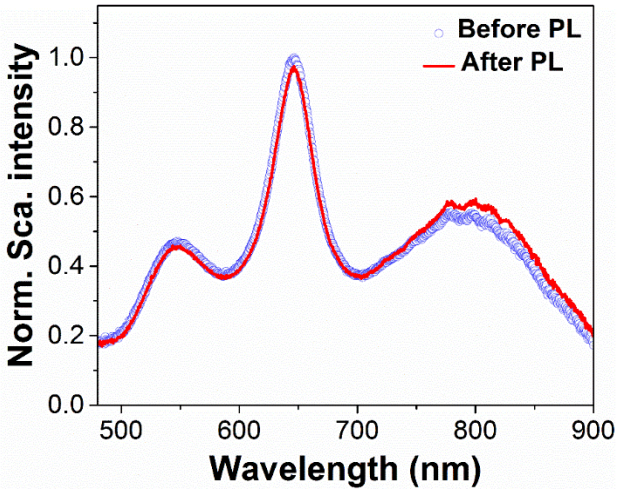

Figure A3. Scattering spectra of a single gold film-coupled gold nanosphere dimer taken before and after photoluminescence measurement. The power density of the 633nm laser is $\sim 1.6 \times 10^4$ W/cm2 in the focus plane.

Excitation and emission polarization dependent photoluminescence spectroscopy of a silica-supported dimer under 633 nm laser illumination

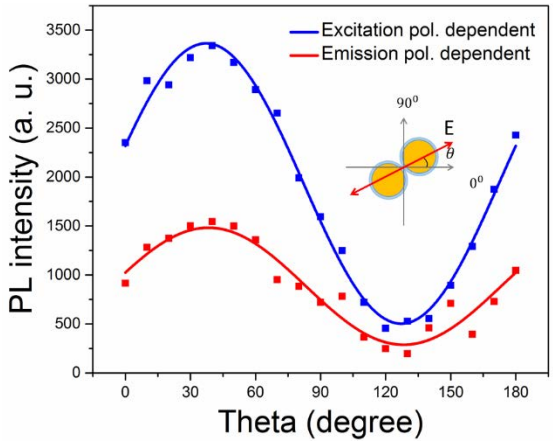

Figure A4. Excitation (blue) and emission (red) polarization dependent photoluminescence intensity under illumination by a 633 nm laser. The solid lines are fits with a cosine function: $y = A + B * cos^2(\frac{\pi}{180}x + C)$. Detailed calculations with the measured data give rise to a degree of polarization (DoP) ~0.71 for detection polarization dependence

Comparison between photoluminescence intensities calculated over the gold film and selected slabs in a film-coupled dimer

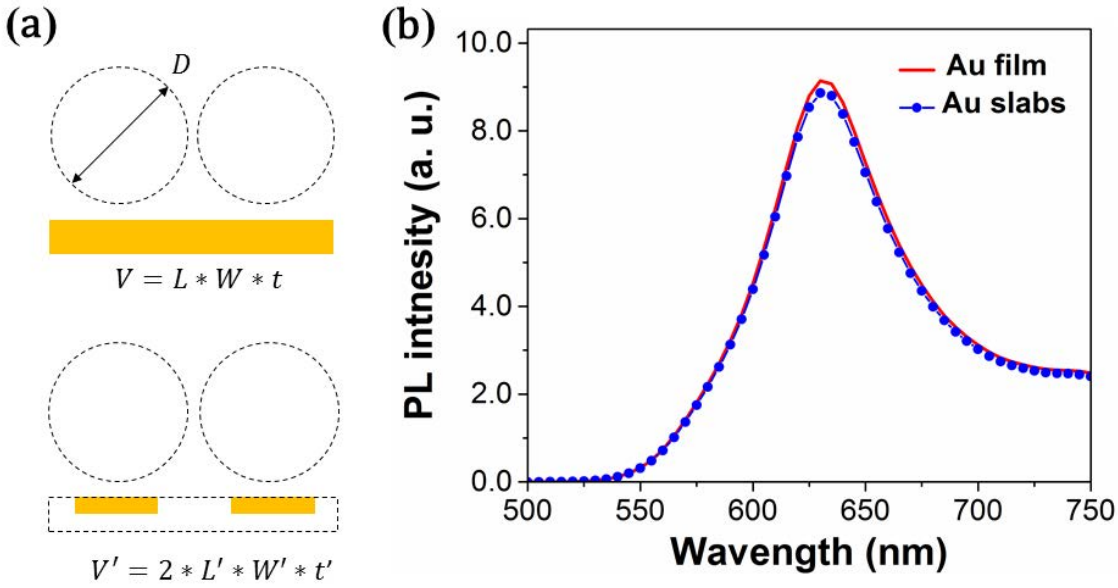

Figure A5. (a) Different integrating domains selected for calculating the photoluminescence contribution from the gold film. $L = 2D = 200$ nm, $W = 100$ nm, $t = 45$ nm, $L' = 12$ nm, $W' = 12$ nm, $t' = 6$ nm. (b) Calculated PL spectra over different domains as indicated in (a). This results confirm that the photoluminescence from the gold film is dominantly contributed by the two ultrasmall domains near the particle-film gaps. In the near-field calculations of the photoluminescence emission intensity, the override meshes applied in meshing the gold slabs, the particle-film gaps and the gold nanospheres have a mesh size of 1nm, 0.2 nm and 1 nm, respectively. The choice of these mesh sizes as well as the mesh size for the whole simulation domain size, the number of PML layers and the conformal mesh scheme are tested to ensure the simulation convergence.

Calculation of the field distributions at the focal plane of focused laser beam

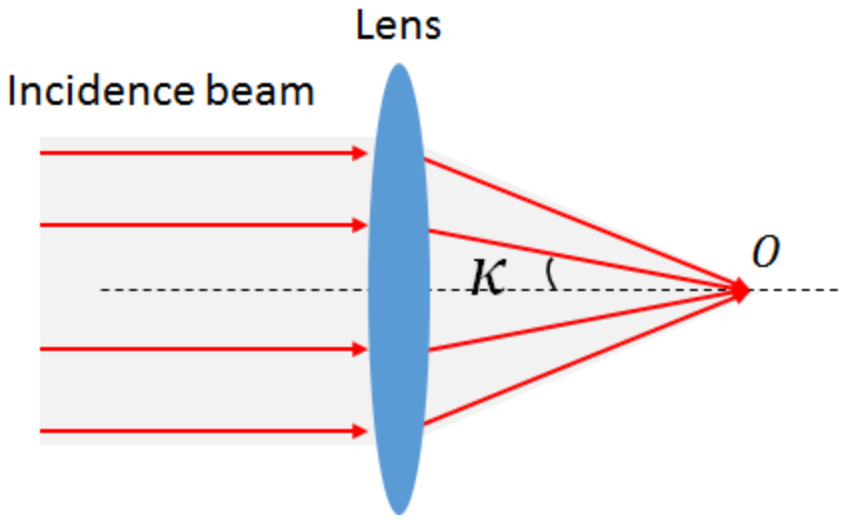

Figure A6 Schematic illustration of the light beam focused by a lens.

As depicted in Figure A6, the $x-$polarized beam, after focused by a lens, the field distribution at the focal plane can be written as

$$E = \begin{bmatrix} E_x \\ E_y \\ E_z \end{bmatrix} = \begin{bmatrix} -iA\left(I_0 + I_2 cos(2\varphi)\right) \\ -iAI_2 sin(2\varphi) \\ -2AI_1 cos(\varphi) \end{bmatrix}$$

where

$$I_0(r) = \int_0^{ksin\alpha} F_0\,[\kappa] J_0[\kappa p] exp\left(i\sqrt{k^2 - \kappa^2}z\right) d\kappa$$

$$I_1(r) = \int_0^{ksin\alpha} F_1\,[\kappa] J_1[\kappa p] exp\left(i\sqrt{k^2 - \kappa^2}z\right) d\kappa$$

$$I_2(r) = \int_0^{ksin\alpha} F_2\,[\kappa]J_2[\kappa p]exp\left(i\sqrt{k^2-\kappa^2}z\right)d\kappa$$

where α corresponds to the NA and is determined by $NA = nsin(\alpha)$; (r, φ) defines the point coordinate at the focal plane.

Similarly, the field distributions of the circular polarized incidences at the focal plane are expressed as follows:

$$E_{cir} = \begin{bmatrix} E_x \\ E_y \\ E_z \end{bmatrix} = \begin{bmatrix} e_x + ie'_x \\ e_y + ie'_y \\ e_z + ie'_z \end{bmatrix} = \begin{bmatrix} -iA[I_0 + I_2 exp(i2\varphi)] \\ A[I_0 - I_2 exp(i2\varphi)] \\ -2AI_1 exp(i\varphi) \end{bmatrix}$$

Evaluation of sample damages induced by the femtosecond laser pulses

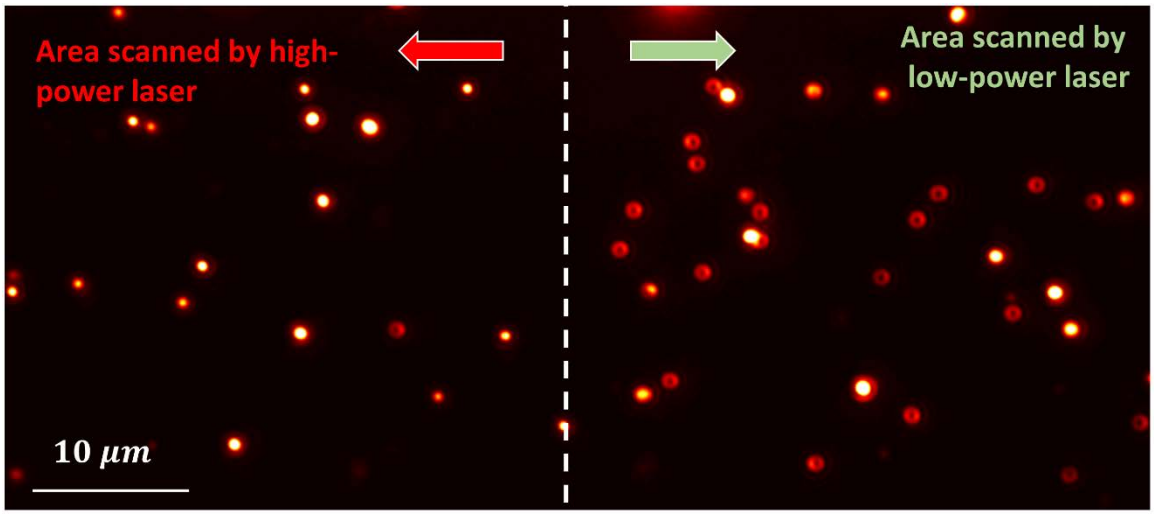

Figure A7 Comparison between dark-field images of samples illuminated by high power laser (~8 mW, left) and low power laser (~0.6 mW, right). The laser wavelength is 850 nm.

Method to evaluate the nonlinear conversion efficiency of single film-coupled nanoparticles

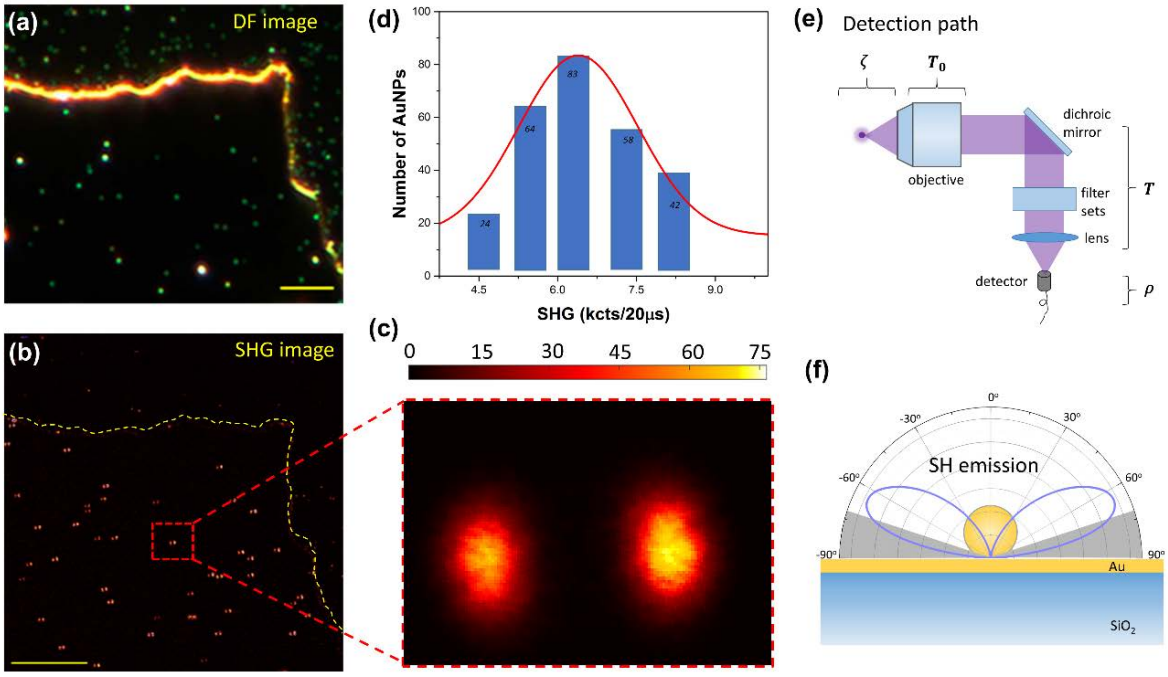

Figure A8 (a-b) Dark-field and nonlinear optical images (400-750 nm) of gold nanoparticles on film (left-bottom). (c) Refined emission pattern of nanoparticles labeled in (b). (d) Statistic histogram counting the numbers of nanoparticle with varied SH intensities. The total particles number is 271. (e) The schematic illustration for the delivery loss of SH signal. (f) Calculated SH emission pattern which determines the collection efficiency of the detection objective used.

Parameters of the excitation

Parameter	**Exc. λ (nm)**	**Laser rep. rate (MHz)**	**laser pulse length (fs)**	**FW average power* (mW)**	**Exc. Obj. NA**	**Spot diameter**	**FW Peak Power (W)**
Symbol	λ	ν	$\boldsymbol{\tau}$	$P_{\mathbf{FW}}$	NA	$\boldsymbol{\delta}$	P'_{FW}
Formula						1.22λ / NA	$P_{\mathbf{FW}} / \boldsymbol{\nu\,\tau}$
Value	850	80	~120	0.8	0.95	~1.1	83

*The value is the effective power corresponding to the longitudinal field component

Parameters of the SH emission

Parameter	SH emitted photons (cts/s)	SHG power (W)	SHG Peak Power (W)	Max. conversion efficiency	Peak Nonlinear Coefficient (/W)
Symbol	N	P_{SH}	P'_{SH}	η_{SHG}	γ_{SHG}
Formula		$N * E_{ph}$	$P_{SH} / (\nu * \tau)$	P_{SH} / P_{FW}	$P'_{SH} / (P'_{FW})^2$
Value	1.49×10^{9}	0.7×10^{-9}	0.73×10^{-4}	0.87×10^{-6}	1.05×10^{-8}

Parameters of the signal delivery system

Parameter	Obj. collection efficiency	Obj. transmittance	Delivery efficiency* (dichroic mirrors, filters, etc.)	Detector quantum efficiency
Symbol	ζ	T_0	T	ρ
Value	0.72	0.85	1.0	0.35
Total detection efficiency: $\sigma = \zeta * T_0 * T * \rho = 0.2142$				

* The value is of a conservative assumption, which leads to decrease of the nonlinear conversion efficiency.

References

(1) Bethe, H. A. Theory of Diffraction by Small Holes. *Phys. Rev.* **1944**, *66*, 163–182.

(2) Roberts, A. Electromagnetic Theory of Diffraction by a Circular Aperture in a Thick, Perfectly Conducting Screen. *J. Opt. Soc. Am. A* **1987**, *4*, 1970.

(3) Kneipp, K.; Moskovits, M.; Kneipp, H. *Surface-Enhanced Raman Scattering*; Kneipp, K.; Moskovits, M.; Kneipp, H., Eds.; Topics in Applied Physics; Springer Berlin Heidelberg, 2006; Vol. 103.

(4) Aoki, T. Photoluminescence Spectroscopy. In *Characterization of Materials*; Kaufmann, E. N., Ed.; John Wiley & Sons, Inc.: Hoboken, NJ, USA, 2012.

(5) Boyd, R. *Nonlinear Optics*; Academic Press, 2008.

(6) Juan, M. L.; Righini, M.; Quidant, R. Plasmon Nano-Optical Tweezers. *Nat. Photonics* **2011**, *5*, 349–356.

(7) Raether, H. *Surface Plasmons on Smooth and Rough Surfaces and on Gratings*; Springer Tracts in Modern Physics; Springer Berlin Heidelberg, 1988; Vol. 111.

(8) Li, J. F.; Huang, Y. F.; Ding, Y.; Yang, Z. L.; Li, S. B.; Zhou, X. S.; Fan, F. R.; Zhang, W.; Zhou, Z. Y.; Wu, D. Y.; *et al.* Shell-Isolated Nanoparticle-Enhanced Raman Spectroscopy. *Nature* **2010**, *464*, 392–395.

(9) Qian, X.-M.; Nie, S. M. Single-Molecule and Single-Nanoparticle SERS: From Fundamental Mechanisms to Biomedical Applications. *Chem. Soc. Rev.* **2008**, *37*, 912–920.

(10) Nie, S. Probing Single Molecules and Single Nanoparticles by Surface-Enhanced Raman Scattering. *Science (80-.).* **1997**, *275*, 1102–1106.

(11) Huang, X.; Jain, P. K.; El-Sayed, I. H.; El-Sayed, M. A. Plasmonic Photothermal Therapy (PPTT) Using Gold Nanoparticles. *Lasers Med. Sci.* **2008**, *23*, 217–228.

(12) Huang, X.; El-Sayed, I. H.; Qian, W.; El-Sayed, M. A. Cancer Cell Imaging and Photothermal Therapy in the near-Infrared Region by Using Gold Nanorods. *J. Am. Chem. Soc.* **2006**, *128*, 2115–2120.

(13) Qian, X.; Peng, X.-H.; Ansari, D. O.; Yin-Goen, Q.; Chen, G. Z.; Shin, D. M.; Yang, L.; Young, A. N.; Wang, M. D.; Nie, S. In Vivo Tumor Targeting and Spectroscopic Detection with Surface-Enhanced Raman Nanoparticle Tags. *Nat. Biotechnol.* **2008**, *26*, 83–90.

(14) Atwater, H. A.; Polman, A. Plasmonics for Improved Photovoltaic Devices. *Nat. Mater.* **2010**, *9*, 205–213.

(15) Clavero, C. Plasmon-Induced Hot-Electron Generation at Nanoparticle/metal-Oxide Interfaces for Photovoltaic and Photocatalytic Devices. *Nat. Photonics* **2014**, *8*, 95–103.

(16) Furube, A.; Du, L.; Hara, K.; Katoh, R.; Tachiya, M. Ultrafast Plasmon-Induced Electron Transfer from Gold Nanodots into TiO2 Nanoparticles. *J. Am. Chem. Soc.* **2007**, *129*, 14852–14853.

(17) Maier, S. A. *Plasmonics: Fundamentals and Applications*; Springer US: Boston, MA, 2007.

(18) Moskovits, M. Surface-Enhanced Spectroscopy. *Rev. Mod. Phys.* **1985**, *57*, 783–826.

(19) Mulvaney, P. Surface Plasmon Spectroscopy of Nanosized Metal Particles. *Langmuir* **1996**, *12*, 788–800.

(20) Sherry, L. J.; Chang, S.-H.; Schatz, G. C.; Van Duyne, R. P.; Wiley, B. J.; Xia, Y. Localized Surface Plasmon Resonance Spectroscopy of Single Silver Nanocubes. *Nano Lett.* **2005**, *5*, 2034–2038.

(21) Righini, M.; Volpe, G.; Girard, C.; Petrov, D.; Quidant, R. Surface Plasmon Optical Tweezers: Tunable Optical Manipulation in the Femtonewton Range. *Phys. Rev. Lett.* **2008**, *100*, 186804.

(22) Juan, M. L.; Righini, M.; Quidant, R. Plasmon Nano-Optical Tweezers. *Nat. Photonics* **2011**, *5*, 349–356.

(23) Quidant, R.; Girard, C. Surface-Plasmon-Based Optical Manipulation. *Laser Photonics Rev.* **2008**, *2*, 47–57.

(24) Trügler, A. *Optical Properties of Metallic Nanoparticles*; Springer Series in Materials Science; Springer International Publishing: Cham, 2016; Vol. 232.

(25) *Absorption and Scattering of Light by Small Particles*; Bohren, C. F.; Huffman, D. R., Eds.; Wiley-VCH Verlag GmbH: Weinheim, Germany, 1998.

(26) Hao, F.; Nordlander, P.; Sonnefraud, Y.; Van Dorpe, P.; Maier, S. A. Tunability of Subradiant Dipolar and Fano-Type Plasmon Resonances in Metallic Ring/disk Cavities: Implications for Nanoscale Optical Sensing. *ACS Nano* **2009**, *3*, 643–652.

(27) Zhou, W.; Odom, T. W. Tunable Subradiant Lattice Plasmons by out-of-Plane Dipolar Interactions. *Nat. Nanotechnol.* **2011**, *6*, 423–427.

(28) Yu, X.; Lei, D. Y.; Amin, F.; Hartmann, R.; Acuna, G. P.; Guerrero-Martínez, A.; Maier, S. A.; Tinnefeld, P.; Carregal-Romero, S.; Parak, W. J. Distance Control in-between Plasmonic Nanoparticles via Biological and Polymeric Spacers. *Nano Today*, 2013, *8*, 480–493.

(29) Sonnefraud, Y.; Verellen, N.; Sobhani, H.; Vandenbosch, G. A. E.; Moshchalkov, V. V; Van Dorpe, P.; Nordlander, P.; Maier, S. A. Experimental Realization of Subradiant, Superradiant, and Fano Resonances in Ring/disk Plasmonic Nanocavities. *ACS Nano* **2010**, *4*, 1664–1670.

(30) Rahmani, M.; Lei, D. Y.; Giannini, V.; Lukiyanchuk, B.; Ranjbar, M.; Liew, T. Y. F.; Hong, M.; Maier, S. A. Subgroup Decomposition of Plasmonic Resonances in Hybrid Oligomers: Modeling the Resonance Lineshape. *Nano Lett.* **2012**, *12*, 2101–2106.

(31) Fan, J. a; Wu, C.; Bao, K.; Bao, J.; Bardhan, R.; Halas, N. J.; Manoharan, V. N.; Nordlander, P.; Shvets, G.; Capasso, F. Self-Assembled Plasmonic Nanoparticle Clusters. *Science* **2010**, *328*, 1135–1138.

(32) Shafiei, F.; Monticone, F.; Le, K. Q.; Liu, X.; Hartseld, T.; Alù, A.; Li, X. A Subwavelength Plasmonic Metamolecule Exhibiting Magnetic-Based Optical Fano Resonance. *Nat. Nanotechnol.* **2013**, *8*, 95–99.

(33) Verellen, N.; Sonnefraud, Y.; Sobhani, H.; Hao, F.; Moshchalkov, V. V; Van Dorpe, P.; Nordlander, P.; Maier, S. A. Fano Resonances in Individual Coherent Plasmonic Nanocavities. *Nano Lett.* **2009**, *9*, 1663–1667.

(34) Hentschel, M.; Saliba, M.; Vogelgesang, R.; Giessen, H.; Alivisatos, A. P.; Liu, N. Transition from Isolated to Collective Modes in Plasmonic Oligomers. *Nano Lett.* **2010**, *10*, 2721–2726.

(35) Wadell, C.; Syrenova, S.; Langhammer, C. Plasmonic Hydrogen Sensing with Nanostructured Metal Hydrides. *ACS Nano*, 2014, *8*, 11925–11940.

(36) Ou, F. S.; Hu, M.; Naumov, I.; Kim, A.; Wu, W.; Bratkovsky, A. M.; Li, X.; Williams, R. S.; Li, Z. Hot-Spot Engineering in Polygonal Nanofinger Assemblies for Surface Enhanced Raman Spectroscopy. *Nano Lett.* **2011**, *11*, 2538–2542.

(37) Feuz, L.; Jonsson, M. P.; Höök, F. Material-Selective Surface Chemistry for Nanoplasmonic Sensors: Optimizing Sensitivity and Controlling Binding to Local Hot Spots. *Nano Lett.* **2012**, *12*, 873–879.

(38) Wang, H.; Wu, Y.; Lassiter, B.; Nehl, C. L.; Hafner, J. H.; Nordlander, P.; Halas, N. J. Symmetry Breaking in Individual Plasmonic Nanoparticles. *Proc. Natl. Acad. Sci. U. S. A.* **2006**, *103*, 10856–10860.

(39) Bachelier, G.; Russier-Antoine, I.; Benichou, E.; Jonin, C.; Del Fatti, N.; Vallée, F.; Brevet, P. F. Fano Profiles Induced by near-Field Coupling in Heterogeneous Dimers of Gold and Silver Nanoparticles. *Phys. Rev. Lett.* **2008**, *101*.

(40) Fedotov, V. A.; Rose, M.; Prosvirnin, S. L.; Papasimakis, N.; Zheludev, N. I. Sharp Trapped-Mode Resonances in Planar Metamaterials with a Broken Structural Symmetry. *Phys. Rev. Lett.* **2007**, *99*.

(41) Zhang, S.; Genov, D. A.; Wang, Y.; Liu, M.; Zhang, X. Plasmon-Induced Transparency in Metamaterials. *Phys. Rev. Lett.* **2008**, *101*.

(42) Prodan, E.; Radloff, C.; Halas, N. J.; Nordlander, P. A Hybridization Model for the Plasmon Response of Complex Nanostructures. *Science* **2003**, *302*, 419–422.

(43) Zohar, N.; Chuntonov, L.; Haran, G. The Simplest Plasmonic Molecules: Metal Nanoparticle Dimers and Trimers. *Journal of Photochemistry and Photobiology C: Photochemistry Reviews*, 2014, *21*, 26–39.

(44) Nordlander, P.; Oubre, C.; Prodan, E.; Li, K.; Stockman, M. I. Plasmon Hybridization in Nanoparticle Dimers. *Nano Lett.* **2004**, *4*, 899–903.

(45) Chu, M.-W.; Myroshnychenko, V.; Chen, C. H.; Deng, J.-P.; Mou, C.-Y.; García de Abajo, F. J. Probing Bright and Dark Surface-Plasmon Modes in Individual and Coupled Noble Metal Nanoparticles Using an Electron Beam. *Nano Lett.* **2009**, *9*, 399–404.

(46) Koh, A. L.; Bao, K.; Khan, I.; Smith, W. E.; Kothleitner, G.; Nordlander, P.; Maier, S. A.; McComb, D. W. Electron Energy-Loss Spectroscopy (EELS) of Surface Plasmons

in Single Silver Nanoparticles and Dimers: Influence of Beam Damage and Mapping of Dark Modes. *ACS Nano* **2009**, *3*, 3015–3022.

(47) Huang, J. S.; Kern, J.; Geisler, P.; Weinmann, P.; Kamp, M.; Forchel, A.; Biagioni, P.; Hecht, B. Mode Imaging and Selection in Strongly Coupled Nanoantennas. *Nano Lett.* **2010**, *10*, 2105–2110.

(48) Yang, S.-C.; Kobori, H.; He, C.-L.; Lin, M.-H.; Chen, H.-Y.; Li, C.; Kanehara, M.; Teranishi, T.; Gwo, S. Plasmon Hybridization in Individual Gold Nanocrystal Dimers: Direct Observation of Bright and Dark Modes. *Nano Lett.* **2010**, *10*, 632–637.

(49) Volpe, G.; Cherukulappurath, S.; Juanola Parramon, R.; Molina-Terriza, G.; Quidant, R. Controlling the Optical near Field of Nanoantennas with Spatial Phase-Shaped Beams. *Nano Lett.* **2009**, *9*, 3608–3611.

(50) Hao, F.; Larsson, E. M.; Ali, T. A.; Sutherland, D. S.; Nordlander, P. Shedding Light on Dark Plasmons in Gold Nanorings. *Chem. Phys. Lett.* **2008**, *458*, 262–266.

(51) Talley, C. E.; Jackson, J. B.; Oubre, C.; Grady, N. K.; Hollars, C. W.; Lane, S. M.; Huser, T. R.; Nordlander, P.; Halas, N. J. Surface-Enhanced Raman Scattering from Individual Au Nanoparticles and Nanoparticle Dimer Substrates. *Nano Lett.* **2005**, *5*, 1569–1574.

(52) Thacker, V. V; Herrmann, L. O.; Sigle, D. O.; Zhang, T.; Liedl, T.; Baumberg, J. J.; Keyser, U. F. DNA Origami Based Assembly of Gold Nanoparticle Dimers for Surface-Enhanced Raman Scattering. *Nat. Commun.* **2014**, *5*, 3448.

(53) Myroshnychenko, V.; Rodríguez-Fernández, J.; Pastoriza-Santos, I.; Funston, A. M.; Novo, C.; Mulvaney, P.; Liz-Marzán, L. M.; García de Abajo, F. J. Modelling the Optical Response of Gold Nanoparticles. *Chem. Soc. Rev.* **2008**, *37*, 1792–1805.

(54) Mock, J. J.; Hill, R. T.; Degiron, A.; Zauscher, S.; Chilkoti, A.; Smith, D. R. Distance-Dependent Plasmon Resonant Coupling between a Gold Nanoparticle and Gold Film. *Nano Lett.* **2008**, *8*, 2245–2252.

(55) Hill, R. T.; Mock, J. J.; Hucknall, A.; Wolter, S. D.; Jokerst, N. M.; Smith, D. R.; Chilkoti, A. Plasmon Ruler with Angstrom Length Resolution. *ACS Nano* **2012**, *6*, 9237–9246.

(56) Englund, D.; Faraon, A.; Fushman, I.; Stoltz, N.; Petroff, P.; Vučković, J. Controlling Cavity Reflectivity with a Single Quantum Dot. *Nature* **2007**, *450*, 857–861.

(57) Faraon, A.; Fushman, I.; Englund, D.; Stoltz, N.; Petroff, P.; Vučković, J. Coherent Generation of Non-Classical Light on a Chip via Photon-Induced Tunnelling and Blockade. *Nat. Phys.* **2008**, *4*, 859–863.

(58) Nomura, M.; Kumagai, N.; Iwamoto, S.; Ota, Y.; Arakawa, Y. Laser Oscillation in a Strongly Coupled Single-Quantum-Dot–nanocavity System. *Nat. Phys.* **2010**, *6*, 279–283.

(59) Lévêque, G.; Martin, O. J. F. Optical Interactions in a Plasmonic Particle Coupled to a Metallic Film. *Opt. Express* **2006**, *14*, 9971–9981.

(60) Lumdee, C.; Yun, B.; Kik, P. G. Effect of Surface Roughness on Substrate-Tuned Gold Nanoparticle Gap Plasmon Resonances. *Nanoscale* **2015**, *7*, 4250–4255.

(61) Schertz, F.; Schmelzeisen, M.; Mohammadi, R.; Kreiter, M.; Elmers, H. J.; Schönhense, G. Near Field of Strongly Coupled Plasmons: Uncovering Dark Modes. *Nano Lett.* **2012**, *12*, 1885–1890.

(62) Lassiter, J. B.; McGuire, F.; Mock, J. J.; Ciracì, C.; Hill, R. T.; Wiley, B. J.; Chilkoti, A.; Smith, D. R. Plasmonic Waveguide Modes of Film-Coupled Metallic Nanocubes. *Nano Lett.* **2013**, *13*, 5866–5872.

(63) Lei, D. Y.; Fernández-Domínguez, A. I.; Sonnefraud, Y.; Appavoo, K.; Haglund, R. F.; Pendry, J. B.; Maier, S. a. Revealing Plasmonic Gap Modes in Particle-on-Film Systems Using Dark-Field Spectroscopy. *ACS Nano* **2012**, *6*, 1380–1386.

(64) Li, G.-C.; Zhang, Y.-L.; Lei, D. Y. Hybrid Plasmonic Gap Modes in Metal Film-Coupled Dimers and Their Physical Origins Revealed by Polarization Resolved Dark Field Spectroscopy. *Nanoscale* **2016**, *8*, 7119–7126.

(65) Mubeen, S.; Zhang, S.; Kim, N.; Lee, S.; Krämer, S.; Xu, H.; Moskovits, M. Plasmonic Properties of Gold Nanoparticles Separated from a Gold Mirror by an Ultrathin Oxide. *Nano Lett.* **2012**, *12*, 2088–2094.

(66) Ciraci, C.; Hill, R. T.; Mock, J. J.; Urzhumov, Y.; Fernandez-Dominguez, a. I.; Maier, S. a.; Pendry, J. B.; Chilkoti, a.; Smith, D. R. Probing the Ultimate Limits of Plasmonic Enhancement. *Science (80-.).* **2012**, *337*, 1072–1074.

(67) Hajisalem, G.; Nezami, M. S.; Gordon, R. Probing the Quantum Tunneling Limit of Plasmonic Enhancement by Third Harmonic Generation. *Nano Lett.* **2014**, *14*, 6651–6654.

(68) Mertens, J.; Eiden, A. L.; Sigle, D. O.; Huang, F.; Lombardo, A.; Sun, Z.; Sundaram, R. S.; Colli, A.; Tserkezis, C.; Aizpurua, J.; *et al.* Controlling Subnanometer Gaps in Plasmonic Dimers Using Graphene. *Nano Lett.* **2013**, *13*, 5033–5038.

(69) Oulton, R. F.; Sorger, V. J.; Zentgraf, T.; Ma, R.-M.; Gladden, C.; Dai, L.; Bartal, G.; Zhang, X. Plasmon Lasers at Deep Subwavelength Scale. *Nature* **2009**, *461*, 629–632.

(70) Russell, K. J.; Liu, T.-L.; Cui, S.; Hu, E. L. Large Spontaneous Emission Enhancement in Plasmonic Nanocavities. *Nat. Photonics* **2012**, *6*, 459–462.

(71) Akselrod, G. M.; Argyropoulos, C.; Hoang, T. B.; Ciracì, C.; Fang, C.; Huang, J.; Smith, D. R.; Mikkelsen, M. H. Probing the Mechanisms of Large Purcell Enhancement in Plasmonic Nanoantennas. *Nat. Photonics* **2014**, *8*, 835–840.

(72) Chikkaraddy, R.; de Nijs, B.; Benz, F.; Barrow, S. J.; Scherman, O. A.; Rosta, E.; Demetriadou, A.; Fox, P.; Hess, O.; Baumberg, J. J. Single-Molecule Strong Coupling at Room Temperature in Plasmonic Nanocavities. *Nature* **2016**, *535*, 127–130.

(73) Benz, F.; Schmidt, M. K.; Dreismann, A.; Chikkaraddy, R.; Zhang, Y.; Demetriadou, A.; Carnegie, C.; Ohadi, H.; de Nijs, B.; Esteban, R.; *et al.* Single-Molecule Optomechanics in "picocavities." *Science (80-.).* **2016**, *354*, 726–729.

(74) Moreau, A.; Ciracì, C.; Mock, J. J.; Hill, R. T.; Wang, Q.; Wiley, B. J.; Chilkoti, A.; Smith, D. R. Controlled-Reflectance Surfaces with Film-Coupled Colloidal Nanoantennas. *Nature* **2012**, *492*, 86–89.

(75) Chikkaraddy, R.; de Nijs, B.; Benz, F.; Barrow, S. J.; Scherman, O. A.; Rosta, E.; Demetriadou, A.; Fox, P.; Hess, O.; Baumberg, J. J. Single-Molecule Strong Coupling at Room Temperature in Plasmonic Nanocavities. *Nature* **2016**, *535*, 127–130.

(76) Mooradian, A. Photoluminescence of Metals. *Phys. Rev. Lett.* **1969**, *22*, 185–187.

(77) Boyd, G. T.; Yu, Z. H.; Shen, Y. R. Photoinduced Luminescence from the Noble Metals and Its Enhancement on Roughened Surfaces. *Phys. Rev. B* **1986**, *33*, 7923–7936.

(78) Wilcoxon, J. P.; Martin, J. E.; Parsapour, F.; Wiedenman, B.; Kelley, D. F. Photoluminescence from Nanosize Gold Clusters. *J. Chem. Phys.* **1998**, *108*, 9137.

(79) Mohamed, M. B.; Volkov, V.; Link, S.; El-Sayed, M. A. The "Lightning" Gold Nanorods: Fluorescence Enhancement of over a Million Compared to the Gold Metal. *Chem. Phys. Lett.* **2000**, *317*, 517–523.

(80) Varnavski, O. P.; Mohamed, M. B.; El-Sayed, M. A.; Goodson, T. Relative Enhancement of Ultrafast Emission in Gold Nanorods. *J. Phys. Chem. B* **2003**, *107*, 3101–3104.

(81) Dulkeith, E.; Niedereichholz, T.; Klar, T. A.; Feldmann, J.; Von Plessen, G.; Gittins, D. I.; Mayya, K. S.; Caruso, F. Plasmon Emission in Photoexcited Gold Nanoparticles. *Phys. Rev. B - Condens. Matter Mater. Phys.* **2004**, *70*.

(82) Wu, X.; Ming, T.; Wang, X.; Wang, P.; Wang, J.; Chen, J. High-Photoluminescence-Yield Gold Nanocubes: For Cell Imaging and Photothermal Therapy. *ACS Nano* **2010**, *4*, 113–120.

(83) He, H.; Xie, C.; Ren, J. Nonbleaching Fluorescence of Gold Nanoparticles and Its Applications in Cancer Cell Imaging. *Anal. Chem.* **2008**, *80*, 5951–5957.

(84) Gan, Z.; Cao, Y.; Evans, R. A.; Gu, M. Three-Dimensional Deep Sub-Diffraction Optical Beam Lithography with 9 Nm Feature Size. *Nat. Commun.* **2013**, *4*, 2061.

(85) Kulmala, S.; Suomi, J. Current Status of Modern Analytical Luminescence Methods. In *Analytica Chimica Acta*; 2003; Vol. 500, pp. 21–69.

(86) Ishikawa-Ankerhold, H. C.; Ankerhold, R.; Drummen, G. P. C. Advanced Fluorescence Microscopy Techniques-FRAP, FLIP, FLAP, FRET and FLIM. *Molecules*, 2012, *17*, 4047–4132.

(87) KÖNIG, K.; SO, P. T. C.; MANTULIN, W. W.; TROMBERG, B. J.; GRATTON, E. Two-photon Excited Lifetime Imaging of Autofluorescence in Cells during UV A and NIR Photostress. *J. Microsc.* **1996**, *183*, 197–204.

(88) Han, M.; Bindewald-Wittich, A.; Holz, F. G.; Giese, G.; Niemz, M. H.; Snyder, S.; Sun, H.; Yu, J.; Agopov, M.; Schiazza, O. La; *et al.* Two-Photon Excited Autofluorescence Imaging of Human Retinal Pigment Epithelial Cells. *J. Biomed. Opt.* **2006**, *11*, 10501-010501–010503.

(89) Lee, J. H.; Lim, C. S.; Tian, Y. S.; Han, J. H.; Cho, B. R. A Two-Photon Fluorescent Probe for Thiols in Live Cells and Tissues. *J. Am. Chem. Soc.* **2010**, *132*, 1216–1217.

(90) Farrer, R. a; Butterfield, F. L.; Chen, V. W.; Fourkas, J. T. Highly Efficient Multiphoton-Absorption-Induced Luminescence from Gold Nanoparticles. *Nano Lett.* **2005**, *5*, 1139–1142.

(91) Wang, D.-S.; Hsu, F.-Y.; Lin, C.-W. Surface Plasmon Effects on Two Photon Luminescence of Gold Nanorods. *Opt. Express* **2009**, *17*, 11350–11359.

(92) Bouhelier, A.; Bachelot, R.; Lerondel, G.; Kostcheev, S.; Royer, P.; Wiederrecht, G. P. Surface Plasmon Characteristics of Tunable Photoluminescence in Single Gold Nanorods. *Phys. Rev. Lett.* **2005**, *95*.

(93) Durr, N. J.; Larson, T.; Smith, D. K.; Korgel, B. A.; Sokolov, K.; Ben-Yakar, A. Two-Photon Luminescence Imaging of Cancer Cells Using Molecularly Targeted Gold Nanorods. *Nano Lett.* **2007**, *7*, 941–945.

(94) König, K.; So, P. T.; Mantulin, W. W.; Gratton, E. Cellular Response to near-Infrared Femtosecond Laser Pulses in Two-Photon Microscopes. *Opt. Lett.* **1997**, *22*, 135–136.

(95) König, K.; Becker, T. W.; Fischer, P.; Riemann, I.; Halbhuber, K. J. Pulse-Length Dependence of Cellular Response to Intense near-Infrared Laser Pulses in Multiphoton Microscopes. *Opt. Lett.* **1999**, *24*, 113–115.

(96) Zijlstra, P.; Chon, J. W. M.; Gu, M. Five-Dimensional Optical Recording Mediated by Surface Plasmons in Gold Nanorods. *Nature* **2009**, *459*, 410–413.

(97) Boardman, A. D.; Zayats, A. V. Nonlinear Plasmonics. *Handb. Surf. Sci.* **2014**, *4*, 329–347.

(98) Celebrano, M.; Wu, X.; Baselli, M.; Großmann, S.; Biagioni, P.; Locatelli, A.; De Angelis, C.; Cerullo, G.; Osellame, R.; Hecht, B.; *et al.* Mode Matching in Multiresonant Plasmonic Nanoantennas for Enhanced Second Harmonic Generation. *Nat. Nanotechnol.* **2015**, *10*, 412–417.

(99) Kachynski, a. V.; Pliss, a.; Kuzmin, a. N.; Ohulchanskyy, T. Y.; Baev, a.; Qu, J.; Prasad, P. N. Photodynamic Therapy by in Situ Nonlinear Photon Conversion. *Nat. Photonics* **2014**, *8*, 1–7.

(100) Wang, F.; Deng, R.; Wang, J.; Wang, Q.; Han, Y.; Zhu, H.; Chen, X.; Liu, X. Tuning Upconversion through Energy Migration in Core–shell Nanoparticles. *Nat. Mater.* **2011**, *10*, 968–973.

(101) Butet, J.; Martin, O. J. F. Nonlinear Plasmonic Nanorulers. *ACS Nano* **2014**, *8*, 4931–4939.

(102) Walsh, G. F.; Dal Negro, L. Enhanced Second Harmonic Generation by Photonic-Plasmonic Fano-Type Coupling in Nanoplasmonic Arrays. *Nano Lett.* **2013**, *13*, 3111–3117.

(103) Metzger, B.; Schumacher, T.; Hentschel, M.; Lippitz, M.; Giessen, H. Third Harmonic Mechanism in Complex Plasmonic Fano Structures. *ACS Photonics* **2014**, *1*, 471–476.

(104) Butet, J.; Brevet, P.-F.; Martin, O. J. F. Optical Second Harmonic Generation in Plasmonic Nanostructures: From Fundamental Principles to Advanced Applications. *ACS Nano* **2015**, *9*, 10545–10562.

(105) Zhang, Y.; Wen, F.; Zhen, Y.-R.; Nordlander, P.; Halas, N. J. Coherent Fano Resonances in a Plasmonic Nanocluster Enhance Optical Four-Wave Mixing. *Proc. Natl. Acad. Sci.* **2013**, *110*, 9215–9219.

(106) Zhang, Y.; Manjavacas, A.; Hogan, N. J.; Zhou, L.; Ayala-Orozco, C.; Dong, L.; Day, J. K.; Nordlander, P.; Halas, N. J. Toward Surface Plasmon-Enhanced Optical Parametric Amplification (SPOPA) with Engineered Nanoparticles: A Nanoscale Tunable Infrared Source. *Nano Lett.* **2016**, *16*, 3373–3378.

(107) Sipe, J. E.; So, V. C. Y.; Fukui, M.; Stegeman, G. I. Analysis of Second-Harmonic Generation at Metal Surfaces. *Phys. Rev. B* **1980**, *21*, 4389–4402.

(108) Bachelier, G.; Butet, J.; Russier-Antoine, I.; Jonin, C.; Benichou, E.; Brevet, P.-F. Origin of Optical Second-Harmonic Generation in Spherical Gold Nanoparticles: Local Surface and Nonlocal Bulk Contributions. *Phys. Rev. B* **2010**, *82*, 235403.

(109) Butet, J.; Duboisset, J.; Bachelier, G.; Russier-Antoine, I.; Benichou, E.; Jonin, C.; Brevet, P. F. Optical Second Harmonic Generation of Single Metallic Nanoparticles Embedded in a Homogeneous Medium. *Nano Lett.* **2010**, *10*, 1717–1721.

(110) Shen, S.; Meng, L.; Zhang, Y.; Han, J.; Ma, Z.; Hu, S.; He, Y.; Li, J.; Ren, B.; Shih, T. M.; *et al.* Plasmon-Enhanced Second-Harmonic Generation Nanorulers with Ultrahigh Sensitivities. *Nano Lett.* **2015**, *15*, 6716–6721.

(111) Butet, J.; Thyagarajan, K.; Martin, O. J. F. Ultrasensitive Optical Shape Characterization of Gold Nanoantennas Using Second Harmonic Generation. *Nano Lett.* **2013**, *13*, 1787–1792.

(112) Chen, P.-Y.; Argyropoulos, C.; D'Aguanno, G.; Alù, A. Enhanced Second-Harmonic Generation by Metasurface Nanomixer and Nanocavity. *ACS Photonics* **2015**, *2*, 1000–1006.

(113) Kruk, S.; Weismann, M.; Bykov, A. Y.; Mamonov, E. A.; Kolmychek, I. A.; Murzina, T.; Panoiu, N. C.; Neshev, D. N.; Kivshar, Y. S. Enhanced Magnetic Second-Harmonic Generation from Resonant Metasurfaces. *ACS Photonics* **2015**, *2*, 1007–1012.

(114) Dong, Z.; Asbahi, M.; Lin, J.; Zhu, D.; Wang, Y. M.; Hippalgaonkar, K.; Chu, H. S.; Goh, W. P.; Wang, F.; Huang, Z.; *et al.* Second-Harmonic Generation from Sub-5 Nm Gaps by Directed Self-Assembly of Nanoparticles onto Template-Stripped Gold Substrates. *Nano Lett.* **2015**, *15*, 5976–5981.

(115) Aouani, H.; Navarro-Cia, M.; Rahmani, M.; Sidiropoulos, T. P. H.; Hong, M.; Oulton, R. F.; Maier, S. A. Multiresonant Broadband Optical Antennas as Efficient Tunable Nanosources of Second Harmonic Light. *Nano Lett.* **2012**, *12*, 4997–5002.

(116) Zhang, Y.; Grady, N. K.; Ayala-Orozco, C.; Halas, N. J. Three-Dimensional Nanostructures as Highly Efficient Generators of Second Harmonic Light. *Nano Lett.* **2011**, *11*, 5519–5523.

(117) Navarro-Cia, M.; Maier, S. A. Broad-Band near-Infrared Plasmonic Nanoantennas for Higher Harmonic Generation. *ACS Nano* **2012**, *6*, 3537–3544.

(118) Lehr, D.; Reinhold, J.; Thiele, I.; Hartung, H.; Dietrich, K.; Menzel, C.; Pertsch, T.; Kley, E. B.; T??nnermann, A. Enhancing Second Harmonic Generation in Gold Nanoring Resonators Filled with Lithium Niobate. *Nano Lett.* **2015**, *15*, 1025–1030.

(119) Thyagarajan, K.; Rivier, S.; Lovera, A.; Martin, O. J. F. Enhanced Second-Harmonic Generation from Double Resonant Plasmonic Antennae. *Opt. Express* **2012**, *20*, 12860.

(120) Liu, S.-D.; Leong, E. S. P.; Li, G.-C.; Hou, Y.; Deng, J.; Teng, J. H.; Ong, H. C.; Lei, D. Y. Polarization-Independent Multiple Fano Resonances in Plasmonic Nonamers for Multimode-Matching Enhanced Multiband Second-Harmonic Generation. *ACS Nano* **2016**, *10*, 1442–1453.

(121) Scholl, J. a; Koh, A. L.; Dionne, J. a. Quantum Plasmon Resonances of Individual Metallic Nanoparticles. *Nature* **2012**, *483*, 421–427.

(122) Scholl, J. A.; García-Etxarri, A.; Koh, A. L.; Dionne, J. A. Observation of Quantum Tunneling between Two Plasmonic Nanoparticles. *Nano Lett.* **2013**, *13*, 564–569.

(123) Zuloaga, J.; Prodan, E.; Nordlander, P. Quantum Description of the Plasmon Resonances of a Nanoparticle Dimer. *Nano Lett.* **2009**, *9*, 887–891.

(124) Y.R.Shen; Principles of Nonlinear Optics. *Princ. Nonlinear Opt.* **1984**.

(125) Stockman, M. I.; Bergman, D. J.; Anceau, C.; Brasselet, S.; Zyss, J. Enhanced Second-Harmonic Generation by Metal Surfaces with Nanoscale Roughness: Nanoscale Dephasing, Depolarization, and Correlations. *Phys. Rev. Lett.* **2004**, *92*, 57402.

(126) Hanke, T.; Krauss, G.; Tr??utlein, D.; Wild, B.; Bratschitsch, R.; Leitenstorfer, A. Efficient Nonlinear Light Emission of Single Gold Optical Antennas Driven by Few-Cycle near-Infrared Pulses. *Phys. Rev. Lett.* **2009**, *103*.

(127) El-Sayed, I. H.; Huang, X.; El-Sayed, M. A. Selective Laser Photo-Thermal Therapy of Epithelial Carcinoma Using Anti-EGFR Antibody Conjugated Gold Nanoparticles. *Cancer Lett.* **2006**, *239*, 129–135.

(128) Haes, a. J.; Van Duyne, R. P. A Nanoscale Optical Blosensor: Sensitivity and Selectivity of an Approach Based on the Localized Surface Plasmon Resonance Spectroscopy of Triangular Silver Nanoparticles. *J. Am. Chem. Soc.* **2002**, *124*, 10596–10604.

(129) Fortina, P.; Kricka, L. J.; Graves, D. J.; Park, J.; Hyslop, T.; Tam, F.; Halas, N.; Surrey, S.; Waldman, S. A. Applications of Nanoparticles to Diagnostics and Therapeutics in Colorectal Cancer. *Trends Biotechnol.* **2007**, *25*, 145–152.

(130) Novotny, L. *Principles of Nano-Optics*; 2006; Vol. 1.

(131) Ladstädter, F.; Hohenester, U.; Puschnig, P.; Ambrosch-Draxl, C. First-Principles Calculation of Hot-Electron Scattering in Metals. *Phys. Rev. B - Condens. Matter Mater. Phys.* **2004**, *70*, 1–10.

(132) Johnson, P. B.; Christy, R. W. Optical Constants of the Noble Metals. *Phys. Rev. B* **1972**, *6*, 4370–4379.

(133) Maier, S. A. Plsmonics : Fundamentals and Applications, 2007.

(134) Mie, G. Beiträge Zur Optik Trüber Medien, Speziell Kolloidaler Metallösungen. *Ann. Phys.* **1908**, *330*, 377–445.

(135) Lockwood, D. J. Rayleigh and Mie Scattering. In *Encyclopedia of Color Science and Technology*; Luo, M. R., Ed.; Springer New York: New York, NY, 2016; pp. 1097–1107.

(136) Jain, P. K.; El-Sayed, M. A. Plasmonic Coupling in Noble Metal Nanostructures. *Chem. Phys. Lett.* **2010**, *487*, 153–164.

(137) Gluodenis, M.; Foss, C. A. The Effect of Mutual Orientation on the Spectra of Metal Nanoparticle Rod−Rod and Rod−Sphere Pairs. *J. Phys. Chem. B* **2002**, *106*, 9484–9489.

(138) Shao, L.; Woo, K. C.; Chen, H.; Jin, Z.; Wang, J.; Lin, H.-Q. Angle- and Energy-Resolved Plasmon Coupling in Gold Nanorod Dimers. *ACS Nano* **2010**, *4*, 3053–3062.

(139) Halas, N. J.; Lal, S.; Chang, W. S.; Link, S.; Nordlander, P. Plasmons in Strongly Coupled Metallic Nanostructures. *Chem. Rev.* **2011**, *111*, 3913–3961.

(140) Lassiter, J. B.; Sobhani, H.; Fan, J. A.; Kundu, J.; Capasso, F.; Nordlander, P.; Halas, N. J. Fano Resonances in Plasmonic Nanoclusters: Geometrical and Chemical Tunability. *Nano Lett.* **2010**, *10*, 3184–3189.

(141) Luk'yanchuk, B.; Zheludev, N. I.; Maier, S. a; Halas, N. J.; Nordlander, P.; Giessen, H.; Chong, C. T. The Fano Resonance in Plasmonic Nanostructures and Metamaterials. *Nat. Mater.* **2010**, *9*, 707–715.

(142) Ghosh, S. K.; Pal, T. Interparticle Coupling Effect on the Surface Plasmon Resonance of Gold Nanoparticles: From Theory to Applications. *Chem. Rev.* **2007**, *107*, 4797–4862.

(143) Kneipp, K.; Wang, Y.; Kneipp, H.; Perelman, L. T.; Itzkan, I.; Dasari, R. R.; Feld, M. S. Single Molecule Detection Using Surface-Enhanced Raman Scattering (SERS). *Phys. Rev. Lett.* **1997**, *78*, 1667–1670.

(144) Jun, Y.; Sheikholeslami, S.; Hostetter, D. R.; Tajon, C.; Craik, C. S.; Alivisatos, A. P. Continuous Imaging of Plasmon Rulers in Live Cells Reveals Early-Stage Caspase-3 Activation at the Single-Molecule Level. *Proc. Natl. Acad. Sci. U. S. A.* **2009**, *106*, 17735–17740.

(145) Huang, D.; Byers, C. P.; Wang, L.; Hoggard, A.; Hoener, B.; Dominguez-Medina, S.; Chen, S.; Chang, W.; Landes, C. F.; Link, S. Photoluminescence of a Plasmonic Molecule. *ACS Nano* **2015**, *9*, 7072–7079.

(146) Wang, H.; Brandl, D. W.; Nordlander, P.; Halas, N. J. Plasmonic Nanostructures: Artificial Molecules. *Acc. Chem. Res.* **2007**, *40*, 53–62.

(147) Panaro, S.; Nazir, A.; Liberale, C.; Das, G.; Wang, H.; De Angelis, F.; Proietti Zaccaria, R.; Di Fabrizio, E.; Toma, A. Dark to Bright Mode Conversion on Dipolar Nanoantennas: A Symmetry-Breaking Approach. *ACS Photonics* **2014**, *1*, 310–314.

(148) Shegai, T.; Chen, S.; Miljković, V. D.; Zengin, G.; Johansson, P.; Käll, M. A Bimetallic Nanoantenna for Directional Colour Routing. *Nat. Commun.* **2011**, *2*, 481.

(149) Woo, K. C.; Shao, L.; Chen, H.; Liang, Y.; Wang, J.; Lin, H.-Q. Universal Scaling and Fano Resonance in the Plasmon Coupling between Gold Nanorods. *ACS Nano* **2011**, *5*, 5976–5986.

(150) Shao, L.; Fang, C.; Chen, H.; Man, Y. C.; Wang, J.; Lin, H.-Q. Distinct Plasmonic Manifestation on Gold Nanorods Induced by the Spatial Perturbation of Small Gold Nanospheres. *Nano Lett.* **2012**, *12*, 1424–1430.

(151) Benz, F.; de Nijs, B.; Tserkezis, C.; Chikkaraddy, R.; Sigle, D. O.; Pukenas, L.; Evans, S. D.; Aizpurua, J.; Baumberg, J. J. Generalized Circuit Model for Coupled Plasmonic Systems. *Opt. Express* **2015**, *23*, 33255.

(152) Chandrasekar, R.; Emani, N. K.; Lagutchev, A.; Shalaev, V. M.; Ciracì, C.; Smith, D. R.; Kildishev, A. V. Second Harmonic Generation with Plasmonic Metasurfaces: Direct Comparison of Electric and Magnetic Resonances. *Opt. Mater. Express* **2015**, *5*, 2682.

(153) Heinz, T. F. Second-Order Nonlinear Optical Effects at Surfaces and Interfaces. In *Nonlinear Surface Electromagnetic Phenomena*; 1991; pp. 353–416.

(154) Dadap, J. I.; Shan, J.; Heinz, T. F. Theory of Optical Second-Harmonic Generation from a Sphere of Centrosymmetric Material: Small-Particle Limit. *J. Opt. Soc. Am. B* **2004**, *21*, 1328–1347.

(155) Wang, F. X.; Rodríguez, F. J.; Albers, W. M.; Ahorinta, R.; Sipe, J. E.; Kauranen, M. Surface and Bulk Contributions to the Second-Order Nonlinear Optical Response of a Gold Film. *Phys. Rev. B* **2009**, *80*, 4–7.

(156) Krause, D.; Teplin, C. W.; Rogers, C. T. Optical Surface Second Harmonic Measurements of Isotropic Thin-Film Metals: Gold, Silver, Copper, Aluminum, and Tantalum. *J. Appl. Phys.* **2004**, *96*, 3626–3634.

(157) Tilley, D. R. Surface Polaritons: Electromagnetic Waves at Surfaces and Interfaces. *Opt. Acta Int. J. Opt.* **1983**, *30*, 1501–1501.

(158) Liebsch, A. Second-Harmonic Generation at Simple Metal Surfaces. *Phys. Rev. Lett.* **1988**, *61*, 1233–1236.

(159) Sundararaman, R.; Narang, P.; Jermyn, A. S.; Goddard III, W. a.; Atwater, H. a. Theoretical Predictions for Hot-Carrier Generation from Surface Plasmon Decay. *Nat. Commun.* **2014**, *5*, 5788.

(160) Ginzburg, P.; Krasavin, A. V.; Wurtz, G. A.; Zayats, A. V. Nonperturbative Hydrodynamic Model for Multiple Harmonics Generation in Metallic Nanostructures. *ACS Photonics* **2015**, *2*, 8–13.

(161) Krasavin, A. V.; Ginzburg, P.; Wurtz, G. A.; Zayats, A. V. Nonlocality-Driven Supercontinuum White Light Generation in Plasmonic Nanostructures. *Nat. Commun.* **2016**, *7*, 11497.

(162) Chen, H.; Shao, L.; Li, Q.; Wang, J. Gold Nanorods and Their Plasmonic Properties. *Chem. Soc. Rev.* **2013**, *42*, 2679–2724.

(163) McPeak, K. M.; Jayanti, S. V.; Kress, S. J. P.; Meyer, S.; Iotti, S.; Rossinelli, A.; Norris, D. J. Plasmonic Films Can Easily Be Better: Rules and Recipes. *ACS Photonics* **2015**, *2*, 326–333.

(164) Yu, B.; Woo, J.; Kong, M.; O'Carroll, D. M. Mode-Specific Study of Nanoparticle-Mediated Optical Interactions in an Absorber/metal Thin Film System. *Nanoscale* **2015**, *7*, 13196–13206.

(165) Mock, J. J.; Hill, R. T.; Tsai, Y. J.; Chilkoti, A.; Smith, D. R. Probing Dynamically Tunable Localized Surface Plasmon Resonances of Film-Coupled Nanoparticles by Evanescent Wave Excitation. *Nano Lett.* **2012**, *12*, 1757–1764.

(166) Ha, J. W.; Marchuk, K.; Fang, N. Focused Orientation and Position Imaging (FOPI) of Single Anisotropic Plasmonic Nanoparticles by Total Internal Reflection Scattering Microscopy. *Nano Lett.* **2012**, *12*, 4282–4288.

(167) Du, L.; Lei, D. Y.; Yuan, G.; Fang, H.; Zhang, X.; Wang, Q.; Tang, D.; Min, C.; Maier, S. a; Yuan, X. Mapping Plasmonic near-Field Profiles and Interferences by Surface-Enhanced Raman Scattering. *Sci. Rep.* **2013**, *3*, 3064.

(168) Sigle, D. O.; Mertens, J.; Herrmann, L. O.; Bowman, R. W.; Ithurria, S.; Dubertret, B.; Shi, Y.; Yang, H. Y.; Tserkezis, C.; Aizpurua, J.; *et al.* Monitoring Morphological Changes in 2D Monolayer Semiconductors Using Atom-Thick Plasmonic Nanocavities. *ACS Nano* **2015**, *9*, 825–830.

(169) Chen, X.; Yang, Y.; Chen, Y.-H.; Qiu, M.; Blaikie, R. J.; Ding, B. Probing Plasmonic Gap Resonances between Gold Nanorods and a Metallic Surface. *J. Phys. Chem. C* **2015**, *119*, 18627–18634.

(170) de Nijs, B.; Bowman, R.; Herrmann, L. O.; Benz, F.; Barrow, S. J.; Sigle, D. O.; Mertens, J.; Eiden, A.; Ferrari, A.; Scherman, P. O.; *et al.* Unfolding the Contents of Sub-Nm Plasmonic Gaps Using Normalising Plasmon Resonance Spectroscopy. *Faraday Discuss.* **2014**, *178*, 185–193.

(171) Yamamoto, N.; Ohtani, S.; García De Abajo, F. J. Gap and Mie Plasmons in Individual Silver Nanospheres near a Silver Surface. *Nano Lett.* **2011**, *11*, 91–95.

(172) Hill, R. T.; Kozek, K. M.; Hucknall, A.; Smith, D. R.; Chilkoti, A. Nanoparticle–Film Plasmon Ruler Interrogated with Transmission Visible Spectroscopy. *ACS Photonics* **2014**, *1*, 974–984.

(173) Wang, Y.; Li, Z.; Zhao, K.; Sobhani, A.; Zhu, X.; Fang, Z.; Halas, N. J. Substrate-Mediated Charge Transfer Plasmons in Simple and Complex Nanoparticle Clusters. *Nanoscale* **2013**, *5*, 9897–9901.

(174) Liu, H.; Ng, J.; Wang, S. B.; Hang, Z. H.; Chan, C. T.; Zhu, S. N. Strong Plasmon Coupling between Two Gold Nanospheres on a Gold Slab. *New J. Phys.* **2011**, *13*, 0–8.

(175) Wang, X.; Li, M.; Meng, L.; Lin, K.; Feng, J.; Huang, T.; Yang, Z.; Ren, B. Probing the Location of Hot Spots by Surface-Enhanced Raman Spectroscopy: Toward Uniform Substrates. *ACS Nano* **2014**, *8*, 528–536.

(176) Gomez, D. E.; Teo, Z. Q.; Altissimo, M.; Davis, T. J.; Earl, S.; Roberts, a. The Dark Side of Plasmonics BT - Nano Letters. *Nano Lett.* **2013**, *13*, 3722–3728.

(177) Schmidt, F. P.; Ditlbacher, H.; Hohenester, U.; Hohenau, A.; Hofer, F.; Krenn, J. R. Dark Plasmonic Breathing Modes in Silver Nanodisks. *Nano Lett.* **2012**, *12*, 5780–5783.

(178) Barrow, S. J.; Rossouw, D.; Funston, A. M.; Botton, G. A.; Mulvaney, P. Mapping Bright and Dark Modes in Gold Nanoparticle Chains Using Electron Energy Loss Spectroscopy. *Nano Lett.* **2014**, *14*, 3799–3808.

(179) Liu, M.; Lee, T. W.; Gray, S. K.; Guyot-Sionnest, P.; Pelton, M. Excitation of Dark Plasmons in Metal Nanoparticles by a Localized Emitter. *Phys. Rev. Lett.* **2009**, *102*, 1–4.

(180) Wu, Y.; Nordlander, P. Finite-Difference Time-Domain Modeling of the Optical Properties of Nanoparticles near Dielectric Substrates. *J. Phys. Chem. C* **2010**, *114*, 7302–7307.

(181) Huang, C.-Z.; Wu, M.-J.; Chen, S.-Y. High Order Gap Modes of Film-Coupled Nanospheres. *J. Phys. Chem. C* **2015**, *119*, 13799–13806.

(182) Yu, X.; Lei, D. Y.; Amin, F.; Hartmann, R.; Acuna, G. P.; Guerrero-Martínez, A.; Maier, S. a.; Tinnefeld, P.; Carregal-Romero, S.; Parak, W. J. Distance Control in-between Plasmonic Nanoparticles via Biological and Polymeric Spacers. *Nano Today* **2013**, *8*, 480–493.

(183) Sobhani, A.; Manjavacas, A.; Cao, Y.; McClain, M. J.; García de Abajo, F. J.; Nordlander, P.; Halas, N. J. Pronounced Linewidth Narrowing of an Aluminum Nanoparticle Plasmon Resonance by Interaction with an Aluminum Metallic Film. *Nano Lett.* **2015**, *15*, 6946–6951.

(184) Berciaud, S.; Cognet, L.; Tamarat, P.; Lounis, B. Observation of Intrinsic Size Effects in the Optical Response of Individual Gold Nanoparticles. *Nano Lett.* **2005**, *5*, 515–518.

(185) Sönnichsen, C.; Franzl, T.; Wilk, T.; von Plessen, G.; Feldmann, J.; Wilson, O.; Mulvaney, P. Drastic Reduction of Plasmon Damping in Gold Nanorods. *Phys. Rev. Lett.* **2002**, *88*, 77402.

(186) Novo, C.; Gomez, D.; Perez-Juste, J.; Zhang, Z.; Petrova, H.; Reismann, M.; Mulvaney, P.; Hartland, G. V. Contributions from Radiation Damping and Surface Scattering to the Linewidth of the Longitudinal Plasmon Band of Gold Nanorods: A Single Particle Study. *Phys. Chem. Chem. Phys.* **2006**, *8*, 3540–3546.

(187) Hentschel, M.; Dregely, D.; Vogelgesang, R.; Giessen, H.; Liu, N. Plasmonic Oligomers: The Role of Individual Particles in Collective Behavior. *ACS Nano* **2011**, *5*, 2042–2050.

(188) Stockman, M. I. Nanoscience: Dark-Hot Resonances. *Nature* **2010**, *467*, 541–542.

(189) Christ, A.; Martin, O. J. F.; Ekinci, Y.; Gippius, N. A.; Tikhodeev, S. G. Symmetry Breaking in a Plasmonic Metamaterial at Optical Wavelength. *Nano Lett.* **2008**, *8*, 2171–2175.

(190) Christ, A.; Ekinci, Y.; Solak, H. H.; Gippius, N. A.; Tikhodeev, S. G.; Martin, O. J. F. Controlling the Fano Interference in a Plasmonic Lattice. *Phys. Rev. B - Condens. Matter Mater. Phys.* **2007**, *76*.

(191) Aubry, A.; Lei, D. Y.; Maier, S. a.; Pendry, J. B. Interaction between Plasmonic Nanoparticles Revisited with Transformation Optics. *Phys. Rev. Lett.* **2010**, *105*, 2–5.

(192) Lei, D. Y.; Aubry, A.; Maier, S. A.; Pendry, J. B. Broadband Nano-Focusing of Light Using Kissing Nanowires. *New J. Phys.* **2010**, *12*, 93030.

(193) Aubry, A.; Lei, D. Y.; Maier, S. a; Pendry, J. B. Plasmonic Hybridization between Nanowires and a Metallic Surface: A Transformation Optics Approach. *ACS Nano* **2011**, *5*, 3293–3308.

(194) Liaw, J.-W.; Liu, C.-L.; Kuo, M.-K. Dual-Band Plasmonic Enhancement of Ag-NS@SiO2 on Gain Medium's Spontaneous Emission. *Plasmonics* **2011**, *6*, 673–680.

(195) Hastings, S. P.; Swanglap, P.; Qian, Z.; Fang, Y.; Park, S. J.; Link, S.; Engheta, N.; Fakhraai, Z. Quadrupole-Enhanced Raman Scattering. *ACS Nano* **2014**, *8*, 9025–9034.

(196) Butet, J.; Russier-Antoine, I.; Jonin, C.; Lascoux, N.; Benichou, E.; Brevet, P. F. Sensing with Multipolar Second Harmonic Generation from Spherical Metallic Nanoparticles. *Nano Lett.* **2012**, *12*, 1697–1701.

(197) Yin, T.; Dong, Z.; Jiang, L.; Zhang, L.; Hu, H.; Qiu, C.-W.; Yang, J. K. W.; Shen, Z. X. Anomalous Shift Behaviors in the Photoluminescence of Dolmen-Like Plasmonic Nanostructures. *ACS Photonics* **2016**, acsphotonics.6b00058.

(198) Hu, H.; Duan, H.; Yang, J. K. W.; Shen, Z. X. Plasmon-Modulated Photoluminescence of Individual Gold Nanostructures. *ACS Nano* **2012**, *6*, 10147–10155.

(199) Beversluis, M.; Bouhelier, A.; Novotny, L. Continuum Generation from Single Gold Nanostructures through near-Field Mediated Intraband Transitions. *Phys. Rev. B* **2003**, *68*, 1–10.

(200) Lumdee, C.; Yun, B.; Kik, P. G. Gap-Plasmon Enhanced Gold Nanoparticle Photoluminescence. *ACS Photonics* **2014**, *1*, 1224–1230.

(201) Aouani, H.; Rahmani, M.; Navarro-Cía, M.; Maier, S. a. Third-Harmonic-Upconversion Enhancement from a Single Semiconductor Nanoparticle Coupled to a Plasmonic Antenna. *Nat. Nanotechnol.* **2014**, 1–5.

(202) Aouani, H.; Navarro-Cía, M.; Rahmani, M.; Maier, S. A. Unveiling the Origin of Third Harmonic Generation in Hybrid ITO-Plasmonic Crystals. *Adv. Opt. Mater.* **2015**, *3*, 1059–1065.

(203) Mesch, M.; Metzger, B.; Hentschel, M.; Giessen, H. Nonlinear Plasmonic Sensing. *Nano Lett.* **2016**, *16*, 3155–3159.

(204) Li, G.-C.; Zhang, Y.-L.; Lei, D. Y. Hybrid Plasmonic Gap Modes in Metal Film-Coupled Dimers and Their Physical Origins Revealed by Polarization Resolved Dark Field Spectroscopy. *Nanoscale* **2016**, 7119–7126.

(205) Shao, L.; Ruan, Q.; Jiang, R.; Wang, J. Macroscale Colloidal Noble Metal Nanocrystal Arrays and Their Refractive Index-Based Sensing Characteristics. *Small* **2014**, *10*, 802–811.

(206) Richards, B.; Wolf, E. Electromagnetic Diffraction in Optical Systems II. Structure of the Image Field in an Aplanatic System. *Proc. R. Soc. LONDON Ser. A-MATHEMATICAL Phys. Sci.* **1959**, *253*, 3580379.

(207) Bomzon, Z.; Gu, M.; Shamir, J. Angular Momentum and Geometrical Phases in Tight-Focused Circularly Polarized Plane Waves. *Appl. Phys. Lett.* **2006**, *89*.

(208) Metzger, B.; Gui, L.; Fuchs, J.; Floess, D.; Hentschel, M.; Giessen, H. Strong Enhancement of Second Harmonic Emission by Plasmonic Resonances at the Second Harmonic Wavelength. *Nano Lett.* **2015**, *15*, 3917–3922.

(209) Celebrano, M.; Wu, X.; Baselli, M.; Großmann, S.; Biagioni, P.; Locatelli, A.; De Angelis, C.; Cerullo, G.; Osellame, R.; Hecht, B.; *et al.* Mode Matching in Multiresonant Plasmonic Nanoantennas for Enhanced Second Harmonic Generation. *Nat. Nanotechnol.* **2015**, *10*, 412–417.

(210) Gennaro, S. D.; Rahmani, M.; Giannini, V.; Aouani, H.; Sidiropoulos, T. P. H.; Navarro-Cía, M.; Maier, S. A.; Oulton, R. F. The Interplay of Symmetry and Scattering Phase in Second Harmonic Generation from Gold Nanoantennas. *Nano Lett.* **2016**, *16*, 5278–5285.

(211) Raziman, T. V; Martin, O. J. F. Does the Real Part Contain All the Physical Information? *J. Opt.* **2016**, *18*, 95002.

(212) Yang, K. Y.; Butet, J.; Yan, C.; Bernasconi, G. D.; Martin, O. J. F. Enhancement Mechanisms of the Second Harmonic Generation from Double Resonant Aluminum Nanostructures. *ACS Photonics* **2017**, *4*, 1522–1530.

(213) Yang, J.; Hugonin, J. P.; Lalanne, P. Near-to-Far Field Transformations for Radiative and Guided Waves. *ACS Photonics* **2016**, *3*, 395–402.

(214) Lee, Y. J.; Schade, N. B.; Sun, L.; Fan, J. A.; Bae, D. R.; Mariscal, M. M.; Lee, G.; Capasso, F.; Sacanna, S.; Manoharan, V. N.; *et al.* Ultrasmooth, Highly Spherical Monocrystalline Gold Particles for Precision Plasmonics. *ACS Nano* **2013**, *7*, 11064–11070.

(215) Lumdee, C.; Yun, B.; Kik, P. G. Effect of Surface Roughness on Substrate-Tuned Gold Nanoparticle Gap Plasmon Resonances. *Nanoscale* **2015**, *7*, 4250–4255.